Topics in Microwave Astronomy and Cosmology

by

Yilun Guan

B. Sc., National University of Singapore, 2014

M. Sc., University of Pittsburgh, 2018

Submitted to the Graduate Faculty of

the Dietrich School of Arts and Sciences in partial fulfillment of

the requirements for the degree of

Doctor of Philosophy

University of Pittsburgh

2021

UNIVERSITY OF PITTSBURGH

DIETRICH SCHOOL OF ARTS AND SCIENCES

This dissertation was presented

by

Yilun Guan

It was defended on

July 12th 2021

and approved by

Arthur Kosowsky, Dept. of Physics and Astronomy, University of Pittsburgh

Jeff Newman, Dept. of Physics and Astronomy, University of Pittsburgh

Brian Batell, Dept. of Physics and Astronomy, University of Pittsburgh

Daniel Boyanovsky, Dept. of Physics and Astronomy, University of Pittsburgh

Hy Trac, Dept. of Physics, Carnegie Mellon University

Topics in Microwave Astronomy and Cosmology

Yilun Guan, PhD

University of Pittsburgh, 2021

Over the past decades, precision measurements of the Cosmic Microwave Background (CMB) have led to remarkable progress in our understanding of the universe in what is known as the standard model of cosmology. In this thesis, we demonstrate the potential of high precision CMB dataset in improving our knowledge in both cosmology and astronomy.

In the first part of the thesis, we show that the upcoming CMB experiments may allow us to detect signals from the primordial magnetic field (PMF) and show that a signal from PMF may pose as a source of confusion to the signal from the primordial gravitational waves from inflation. We further show how one can effectively break the degeneracy with the help of precision measurements of the small-scale CMB anisotropies.

In the second part of the thesis, we explore the use of precision measurements of the small-scale CMB anisotropies in constraining physics beyond the standard model. With data obtained from the Atacama Cosmology Telescope (ACT), we search for a signal of parity violating physics in the early universe known as cosmic birefringence. Our non-detection allows us to place a tightest constraint on such effect at the time which improves the previous limit by a factor of 3.

In the next part of the thesis, we demonstrate that the high angular resolution CMB dataset can also be used for galactic science. By combining the CMB datasets from ACT and Planck, we make and present a map of the Galactic center region that improves the previous maps in the microwave frequencies in terms of a wider field of view, higher angular resolution, and sensitivity in both temperature and polarization measurements.

In the last part of the thesis, we discuss the prospects of the upcoming data release (DR6) from ACT which is expected to improve our constraints on cosmological parameters by a factor of 2. I provide a description of an important preprocessing step known as the data cuts pipeline, which identifies data with sporadic pathologies and removes them from the CMB mapmaking, and show the preliminary results from the pipeline for the ACT DR6.

Table of Contents

List of Tables

List of Figures

Preface

The work presented in this thesis would not be possible without the help from many individuals whom I am fortunate to work with. I am extremely grateful for my advisor, Arthur Kosowsky, for his guidance and support throughout my PhD journey. His enthusiasm and deep knowledge of science have always been a source of inspiration to me. I would also like to thank members of my thesis committee: Brian Batell, Jeffrey Newman, Hy Trac, and especially Daniel Boyanovsky for providing valuable feedbacks and asking thought provoking questions about my thesis work.

During my thesis study, I had the furtune to join the ACT Collaboration and work with many amazing colleagues. I am particularly grateful to Rolando Dünner and Loïc Maurin for patiently tutoring me the data cuts pipeline in ACT, to Matthew Hasselfield and Sigurd Naess for patiently explaining the nitty-gritty details of CMB data analysis to me and guiding me through all of the technical challenges I encountered, to Fernando Zago and Simone Aiola for giving me so many precious advices in navigating academic life, and to Susan Clark and Brandon Hensley for introducing me to Galactic science.

I also must not understate the importance of my friends and colleagues in the department who have made my PhD life so much more enjoyable, with special thanks to Hongbo Cai, Yang Ma for the long hours of illuminating physics discussion, and to Bomin Zhang, Lisong Chen, Iris Leung, for all the fun weekend activities that I will truly miss.

Last but not the least, I would like to thank my family members without whose support and encouragement this work would not have been possible. I am particularly grateful to my parents for bringing me into the world and nurturing me into the person I am, to my parents-in-law for being solicitous of my well being, and most importantly, to my loving wife, Caroline Ren, for supporting me unconditionally and taking a selfless care of my life, without whom I would not have achieved anything.

1.0 Introduction

In this chapter, we review the basics of modern theoretical and observational cosmology focusing particularly on the Cosmic Microwave Background. Although the information presented here does not constitute original research, the content presented in this chapter will be useful for a good understanding of the subsequent chapters that describe original works.

1.1 Standard model of cosmology

Over the past decades, our understanding of cosmology has improved tremendously with the observations of the Cosmic Microwave Background (CMB) and the Large Scale Structure (LSS) of our universe. These observational evidences reveal to us a remarkably simple universe that can be well described by only a few parameters in what is known as the Standard Model of Cosmology, or, as is often called, the Lambda Cold Dark Matter (ΛCDM) model. In the ΛCDM model, the universe starts from a hot and dense state known as the Big Bang about 13.8 billions years ago. It undergoes a rapid expansion known as the inflation, during which the universe expands in size by many orders of magnitude, ending up as the spatially flat universe that we see today. The evolution of the universe can be well described by its principal constituents, which include photons, dark matter, baryonic matter, and dark energy. Surprisingly, about $\sim 70\%$ of the energy content of our universe is in what is known as the dark energy, and out of the remaining 30% that matter constitutes, $\sim 80\%$ is in the form of dark matter, which, as far as we know, only interacts gravitationally. The baryonic matter, which composes stars, galaxies, including us, only constitutes $\sim 5\%$ of the total energy content of the universe.

Despite the remarkable success of the ΛCDM model, there remains many open questions. In particular, although dark matter and dark energy constitute about 95% of the total energy density of our universe, their origins remain poorly understood. In addition, the apparent spatial flatness of the universe and the horizon problem – two points outside their respective

light cones appear to have been in thermal equilibrium in the past – lead to the speculations of an inflationary period in the early universe known as inflation, a period in which the universe expands exponentially fast. Despite the speculations, the nature of inflation, including its existence, remains debatable, with no direct observational evidences found to date. On the other hand, inflation, if occurred, may induce tensor-mode metric perturbation that will leave an imprint in the CMB, thus giving us a promising probe of the inflation physics. As a result, the hunt for such signal is one of the major scientific targets of the current and upcoming CMB experiments – a topic that we shall discuss more in Chapter 2.

1.1.1 Friedmann-Lemaître-Robertson-Walker cosmology

The observations of the CMB and the LSS provide compelling evidences of the statistical isotropy of our universe on the large scale ($\gtrsim 100\,\mathrm{Mpc}$). This motivates us to describe the large scale geometry of the universe with the Friedmann-Lemaître-Robertson-Walker (FLRW) metric

$$ds^2 = g_{\mu\nu}dx^\mu dx^\nu = -c^2dt^2 + a^2(t)\left(\frac{dr^2}{1-Kr^2} + r^2 d\Omega^2\right), \tag{1}$$

with $d\Omega^2 \equiv d\theta^2 + \sin^2\theta d\phi^2$. Here $a(t)$ is known as the scale factor, which describes the expansion of the universe, t is the proper time or the cosmic time, the spatial coordinates are known as the comoving coordinates, and K is a curvature parameter with $K = -1, 0, 1$ corresponding to a closed, flat, and open universe, respectively. One can define a conformal time $d\eta \equiv dt/a$, and express the FLRW as

$$ds^2 = a(\eta)^2\left(-c^2d\eta^2 + \frac{dr^2}{1-Kr^2} + r^2 d\Omega^2\right), \tag{2}$$

which is conformal to a non-expanding metric with a conformal factor of $a(\eta)^2$. In the case of $K = 0$, it is conformal to the Minkowski metric. As we have no observational evidence for non-flat universe, we shall assume $K = 0$ hereafter.

The evolution of our universe and the constituents within can then be described using the Einstein equations

$$R_{\mu\nu} - \frac{1}{2}Rg_{\mu\nu} = \frac{8\pi G}{c^4}\left(T_{\mu\nu} - \frac{\Lambda c^4}{8\pi G}g_{\mu\nu}\right), \tag{3}$$

which relates the geometric property of the spacetime (left hand side) to the energy content that lies within (right hand side). In particular, $R_{\mu\nu}$ is known as the Ricci tensor, which is a function of metric and its derivatives, R is the Ricci scalar, defined as $R \equiv g^{\mu\nu}R_{\mu\nu}$, $T_{\mu\nu}$ is the energy-momentum tensor, G is the Newton's gravitational constant, and Λ is known as the cosmological constant, which is one of the potential sources of dark energy.

With the FLRW metric, the Ricci tensor is given by

$$R_{00} = -\frac{3}{c^2}\frac{\ddot{a}}{a}, \quad R_{0i} = 0, \quad R_{ij} = \frac{1}{c^2}g_{ij}\left(2H^2 + \frac{\ddot{a}}{a} + 2\frac{Kc^2}{a^2}\right), \tag{4}$$

and the Ricci scalar is given by

$$R = \frac{6}{c^2}\left(\frac{\ddot{a}}{a} + H^2 + \frac{Kc^2}{a^2}\right). \tag{5}$$

Substituting into the Einstein equations, one gets the Friedmann equations

$$\begin{aligned} H^2 + \frac{Kc^2}{a^2} &= \frac{8\pi G}{3c^2}T_{00} + \frac{\Lambda c^2}{3}, \\ g_{ij}\left(H^2 + 2\frac{\ddot{a}}{a} + \frac{Kc^2}{a^2} - \Lambda c^2\right) &= -\frac{8\pi G}{c^2}T_{ij}. \end{aligned} \tag{6}$$

With the assumption that the universe is both homogeneous and isotropic, the energy-momentum tensor of a given cosmological constituent, such as photons or dark matter, can be described as a perfect fluid with no bulk velocity, given by

$$T^{\mu}{}_{\nu} = \mathrm{diag}(\rho, P, P, P), \tag{7}$$

with ρ the energy density, and P the pressure density of the constituent. Under this assumption, the Friedmann equations become

$$H^2 = \frac{8\pi G}{3}\rho + \frac{\Lambda c^2}{3} - \frac{Kc^2}{a^2}, \tag{8}$$

$$\frac{\ddot{a}}{a} = -\frac{4\pi G}{3}\left(\rho + \frac{3P}{c^2}\right) + \frac{\Lambda c^2}{3}. \tag{9}$$

The total energy density ρ and pressure P can be decomposed in terms of density and pressure of the individual components of the universe as

$$\rho = \sum_i \rho_i, \quad P = \sum_i P_i, \tag{10}$$

where i can be radiation, matter, and dark energy. Equation 8 can then be broken down into

$$H^2(a) = \frac{8\pi G}{3}(\rho_\gamma + \rho_c + \rho_K + \rho_\Lambda), \tag{11}$$

where ρ_γ is the energy density of photons, ρ_c is the energy density of cold dark matter, $\rho_K \equiv -3Kc^2/8\pi Ga^2$ can be seen as the energy density of curvature, and $\rho_\Lambda \equiv \Lambda/8\pi G$ is the energy density of the dark energy. It is also convenient to define a critical density as $\rho_{\text{crit}} = 3H^2/8\pi G$, which has a present day value around $10^{-29}\,\text{g}\,\text{cm}^{-3}$, and the rest of the energy densities can then be expressed as fractions to the critical density, defined as $\Omega_i \equiv \rho_i/\rho_{\text{crit}}$. Equation 11 now becomes

$$\Omega_\gamma + \Omega_c + \Omega_\Lambda = 1 - \Omega_K. \tag{12}$$

This shows that if the universe is spatially flat, the total energy density matches the critical density ρ_c. In fact, observations from the Planck satellite [1] have provided strong evidence that this is indeed the case, that we live in a spatially flat universe, with a current best constraint of $\Omega_K = 0.0008^{+0.0040}_{-0.0039}$ at 95% confidence level, consistent with 0.

In addition to the Einstein equations, the conversation law $\nabla_\nu T^{\mu\nu} = 0$ also gives a continuity equation (for the $\nu = 0$ component)

$$\dot{\rho} + 3H\left(\rho + \frac{P}{c^2}\right) = 0. \tag{13}$$

Assuming that the component of interests has an equation of state of form $P = w\rho c^2$ with a constant w, one gets

$$\frac{\dot{\rho}}{\rho} = -3H(1+w), \tag{14}$$

which has a general solution of the form

$$\rho = \rho_0 a^{-3(1+w)}. \tag{15}$$

In Table 1.1, we summarize the difference in the equation of state parameter w for different components in the ΛCDM model. In particular, for dark matter the pressure is negligible, and hence we get $w = 0$. For radiation, $P = \rho c^2/3$ and hence $w = 1/3$. For cosmological

Constituent	w	Scaling
Radiation	w = 1/3	$\rho_\gamma \propto a^{-4}$
Matter	w = 0	$\rho_m \propto a^{-3}$
Cosmological constant	w = -1	$\rho_\Lambda \propto a^0$

Table 1.1: Equation of state parameters of different constituents of the universe and their scaling with a.

constant, we expect ρ_Λ to remain constant with time, and this reversely tells us that its equation of state is $P = -\rho c^2$, with $w = -1$.

Equation 11 can then be expressed in terms of the energy density at the present day as

$$H^2(a) = H_0^2 \left(\Omega_{\gamma,0} a^{-4} + \Omega_{m,0} a^{-3} + \Omega_{\Lambda,0}\right), \tag{16}$$

where H_0 is the Hubble parameter today, known as the Hubble's constant and measured to be $\sim 70\,\mathrm{km\,s^{-1}\,Mpc^{-1}}$ [1], and $\Omega_{i,0}$ refers to the present day value of Ω_i. As the energy density of Λ stays constant during the cosmic expansion, $\Omega_\Lambda = \Omega_{\Lambda,0}$. Note that we have ignored the curvature contribution which would otherwise contributes a factor of $H_0^2\,\Omega_{K,0} a^{-2}$ on the right hand side.

In Table 1.2, we show the present day values of the contribution from different components measured by Planck [1]. In particular, the matter contribution can be further splitted into contributions from the baryonic matter (Ω_b) and the dark matter (Ω_c) as $\Omega_m = \Omega_b + \Omega_c$, where the contribution from dark matter is about a factor of 5 larger than the baryonic matter. In practice, one often uses $\Omega_i h^2$ instead of Ω_i, with $h \equiv H_0/100\,\mathrm{km\,s^{-1}\,Mpc^{-1}}$, to get rid of its dependency on the Hubble constant H_0.

Energy density	Present day value
Ω_Λ	0.6911 ± 0.0062
$\Omega_{m,0}$	0.3089 ± 0.0062
$\Omega_{K,0}$	0.0008 ± 0.0013
$\Omega_{\gamma,0}$	$9.17 \pm 1.90 \times 10^{-6}$
$\Omega_{b,0}$	0.0486 ± 0.0010
$\Omega_{c,0}$	0.2589 ± 0.0057

Table 1.2: Measurements of the present day value of the contribution from different constituents from Planck [1]. In particular, we further decompose the matter density Ω_m into the dark matter contribution and the baryonic matter contribution, with $\Omega_m = \Omega_c + \Omega_b$.

1.1.2 Expansion history

The expansion history of our universe can be described in terms of the redshift of the received photon, defined as

$$z = \frac{\lambda_o - \lambda_e}{\lambda_e}, \tag{17}$$

with λ_0 the observed wavelength of the photon and λ_e the emitted wavelength of the photon. Redshift z is related to the scale factor a by

$$a = 1/(1+z), \tag{18}$$

after settting the scale factor today as $a_0 = 1$. As the universe expands, the temperature cools down following the relation $T(z) = T_0(1+z)$, with T_0 the temperature of the universe today, measured to be $\simeq 2.7\,\mathrm{K}$.

Different components in the universe scale differently as a function of scale factor, as shown in Equation 16 and depicted in Figure 1.1. Specifically, in the early universe and at a redshift of $z \gtrsim 10^5$ (or $a \lesssim 10^{-5}$), the universe is dominated by radiation. In this era, the total

[1]The measurements of Hubble's constants have some controversy of its own, with an apparent "tension" between the results from the early universe and the local universe. See Ref. [10] for a review.

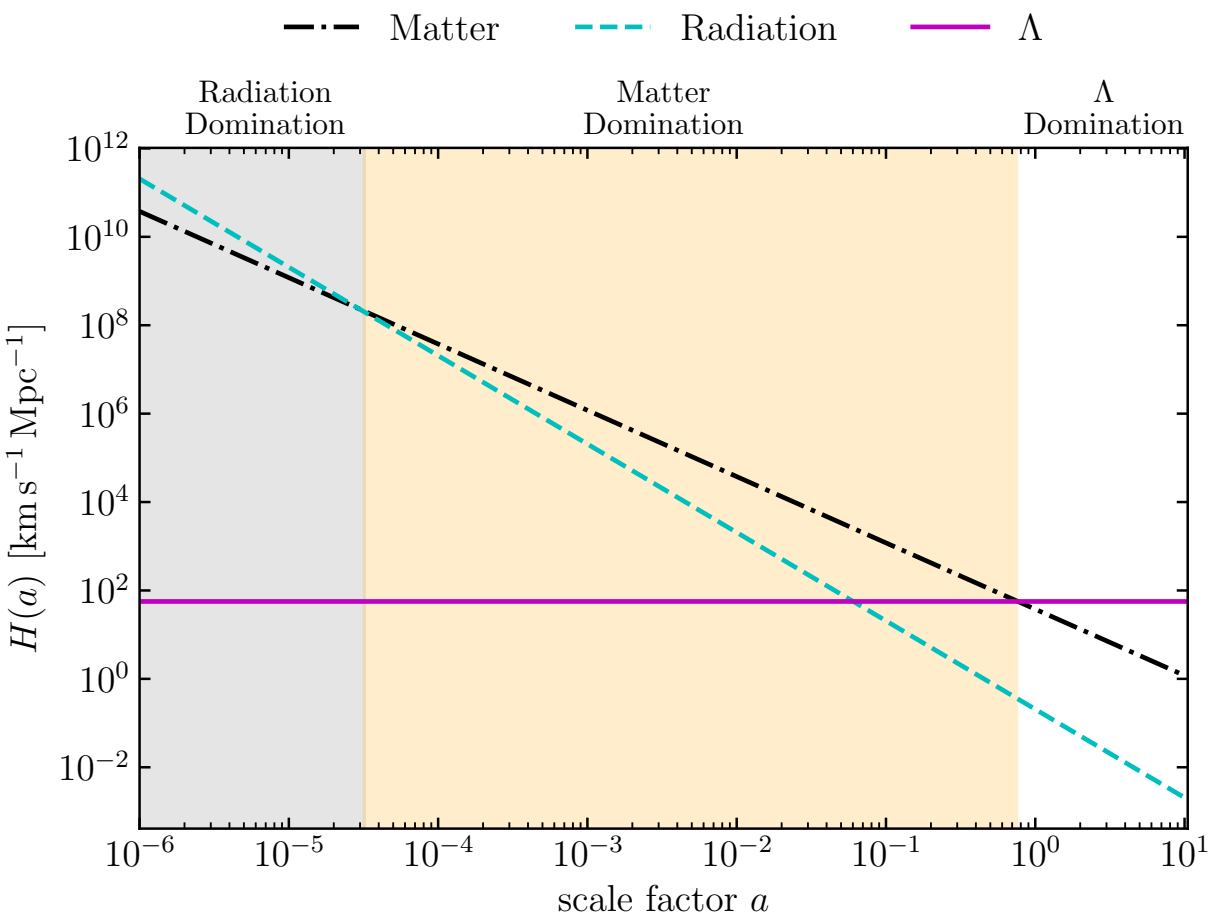

Figure 1.1: How Hubble parameter $H(a)$ changes with scale factor a for different constituents of the universe. Our universe has transitioned from radiation domination to matter domination and only recently to a Λ domination.

energy density consists mostly of photons, neutrinos, and relativistic particles in a highly thermalized state. The universe is opaque to light due the tight coupling between photons and baryons in the primordial plasma. As the universe expands, the energy density of photons drops faster due to the a^{-4} dependence compared to matter which drops with a^{-3}. At a redshift of $z \sim 3300$, the relative amounts of radiation and matter reach a comparable level, known as the matter-radiation equality. At a redshift of $z \sim 1100$, photons are no longer energetic enough to couple to the baryons and start free-streaming across space. During this period, the universe becomes transparent to light as electrons recombine with protons to form neutral atoms – a period known as Recombination. As shown in Figure 1.2, the ionization fraction, defined as $X_e \equiv n_e/(n_e + n_p)$, drops quickly at $z \sim 1100$. The decoupled photons then travel freely across space and become what is known as the cosmic microwave background that we observe today, carrying imprints of physics in the early universe. The universe remains neutral until at a redshift of $z = 7 - 20$, when the universe starts to be ionized again due to the ionizing radiation sourced by the first generation of stars, which just begin to form at the time. This period is known as the Reionization and can be seen in Figure 1.2 as the rapid rise in ionization fraction at $z \sim 10$. Furthermore, at a redshift of $z \sim 0.4$ or about 4 billions years ago, the universe transitions into a dark energy dominated era. As dark energy has an equation of state of $P = -\rho$, featuring a negative pressure, a dark energy dominated universe will experience accelerated expansion rate. The accelerated expansion rate has, in fact, been confirmed experimentally based on supernova observations [11], providing strong evidence of the presence of dark energy in the universe.

1.1.3 Inhomogeneous universe

So far we have only focused on the homogeneous universe, but we know that this cannot be the full picture – inhomogeneity in the universe must exist, because otherwise galaxies, stars, including us, could not have existed. Evidences from the CMB also show that the CMB temperature has anisotropies at the level of a few parts in 10^5. This exceedingly small amount of inhomogeneities allow us to treat them as perturbations to the otherwise homogeneous background densities and describe their evolution via linear perturbation theory. As the full

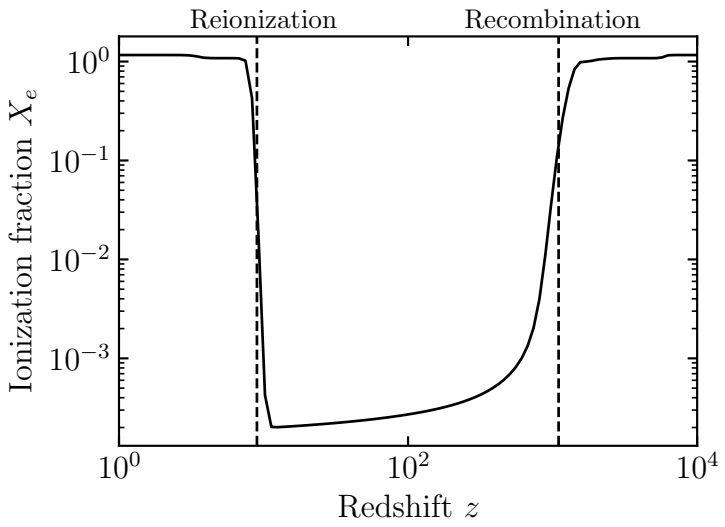

Figure 1.2: Ionization fraction $X_e \equiv n_e/(n_e + n_p)$ as a function of redshift z. The reference redshifts for recombination and reionization processes are indicated with dashed lines. The data in the plot is computed using CAMB [2].

calculation of the evolution of cosmological perturbation is rather technical and not particular illuminating, we thus refer interested readers to Refs. [12, 13] for the full treatment and, for the purpose of introducing the basic concepts, we shall follow the heuristic approach in Ref. [14] and provide only a qualitative overview of the physics.

In the presence of inhomogeneity, the metric tensor can be decomposed as $g_{\mu\nu} = \overline{g}_{\mu\nu} + \delta g_{\mu\nu}$, where $\overline{g}_{\mu\nu}$ represents the homogeneous and isotropic FLRW metric. The perturbed metric $\delta g_{\mu\nu}$ has 10 degrees of freedom, describing different types of metric perturbations. In particular, the 10 degrees of freedom can be decomposed into 4 scalar-type perturbations, 2 vector-type perturbations, and 2 tensor-type perturbations. On the other hand, it is important to note that in an inhomogeneous universe the distinction between background quantity and perturbations may not be as clear-cut and may depend on the particular choice of coordinate system, or gauge, as often called. In other words, $\delta g_{\mu\nu}$ features additional gauge degrees of freedom, which can be described by an infinitesimal coordinate transformation $x^\mu \to \hat{x}^\mu = x^\mu + \xi^\mu(x)$, with ξ^μ being the generator of the gauge transformation. As ξ^μ

contains 2 scalar and 2 vector degrees of freedom, by fixing a gauge the metric tensor $\delta g_{\mu\nu}$ is left with 2 scalar, 2 vector, and 2 tensor degrees of freedom. A common gauge used in cosmology is known as the Conformal Newtonian Gauge (CNG), advocated by Ref. [15]. Under this gauge, the two scalar perturbations can be interpreted physically as gravitational potential and anisotropic stress perturbations, the two vector perturbations can be interpreted as vorticity and shear perturbations, and the two tensor perturbations can be interpreted as polarizations of gravitational waves.

Different types of perturbations evolve independently according to Einstein equations. In particular, density fluctuations only produce scalar perturbations, and thus they will be our main focus in the subsequent discussion. Vector and tensor perturbations are expected to be zero in the context of the ΛCDM model, though they can be produced in special circumstances such as in the presence of a magnetic field – a possibility that we shall discuss in details in Chapter 2. It is also important to note that tensor perturbations, in particular, can also be sourced by primordial gravitational waves generated during inflation, if it has indeed occurred, which may provide a direct observational probe of inflation – an important topic that we shall discuss again in Section 1.2 and Chapter 2.

The evolution of perturbations is described by the Einstein equations and depends both on the equation of states of each component and the expansion rate of the universe. Before recombination ($z \gtrsim 1100$), the physical picture is conceptually simple: as photons and baryons were tightly coupled, and as dark matter was effectively cold by definition, the evolution of perturbation of each component can be well approximated by a fluid model, described only by the equivalences of a continuity equation and an Euler equation in the context of an expanding universe, with exceptions for photons and baryons where an interaction term needs to be included accounting for their coupling through Thomson scattering. The results are a set of coupled differential equations with well-posed initial condition problems. Although getting an accurate description of their evolution requires a full numerical treatment of the coupled differential equations, as implemented in codes such as CAMB [2] and CLASS [16], our qualitative descriptions above provide enough ingredients to grasp the essence of the physical picture, as summarized below.

- The competition of gravitational collapse and radiation pressure causes acoustic oscil-

lations in the photon-baryon fluid which stops after photons decouple from baryons at recombination. The acoustic oscillation patterns are imprinted in the CMB and can be seen in the power spectrum of CMB anisotropies, which we shall discuss in Section 1.2.

- The growth of baryon over-densities are suppressed at the sub-horizon scales by the tight couplings between baryons and photons, and by radiative pressures from photons, until photon decoupling.
- As electrons recombine with protons to form neutral atoms, the mean free path of Thomson scattering starts to increase, this causes the acoustic oscillation patterns on the scales smaller than the photon mean free path to get erased – an effect known as the Silk damping.
- Before recombination, the tight coupling between photons and baryons prevents photons from developing any anisotropies apart from a dipole distribution that tightly couples to the velocity perturbation of baryons. As the mean free path of photons increase, higher order anisotropies start to develop. In particular, the quadrapole photon distribution leads to polarization of the CMB photons.

The physics of the evolution of perturbations is well described by the standard model of cosmology, specified by only a small number of cosmological parameters. In general, these parameters contain two categories: those that describe the background densities, and those that describe the perturbations. A non-exhaustive list of some notable cosmological parameters is summarized below:

- Ω_c: The ratio of the dark matter density to the critical density.
- Ω_b: The ratio of the baryon density to the critical density.
- Ω_Λ: The ratio of the dark energy density to the critical density.
- Ω: The ratio of the total energy density to the critical density. $\Omega = 1$ for a flat universe, and deviations from 1 characterizes the spatial curvature of the universe.
- H_0 or h: Hubble (or reduced Hubble) parameter at the present day.
- A_s and n_s: Amplitude and spectral index for the primordial power spectrum which characterizes the statistics of the seed fluctuations from, as we now believe, quantum

fluctuations in the very early universe. The primordial power spectrum $\mathcal{P}(k)$ is often parameterized as a power law around a pivot scale k_0, given by $\mathcal{P}(k) = A_s(k_0)(k/k_0)^{n_s-1}$.

- N_{eff}: The effective number of neutrino species. In the radiation-dominated era, neutrinos, having a negligible mass, are highly relativistic and constitute a fraction of the energy density of radiation, with an energy density given by $\rho_\nu = N_{eff}7/8(4/11)^{4/3}\rho_\gamma$, where ρ_γ is the energy density of photons, and N_{eff} is the effective number of neutrino species defined above, expected to be 3.046 based on predictions from the standard model of particle physics. Neutrinos decouple earlier than the CMB photons, with a temperature lower than that of the photons by a factor of $(4/11)^{4/3}$. The decoupled neutrinos free-stream at nearly the speed of light and induce anisotropic stress to the metric, which is relevant in Chapter 2 due to its interplay with the anisotropic stress from a magnetic field.
- τ: The optical depth to reionization. It characterizes the probability of a CMB photon being scattered by ionized electrons between the time of Reionization to the present day, known to be $\sim 8\%$.
- r: The tensor-to-scalar ratio. Similar to A_s and n_s which parameterize the statistics of the initial scalar perturbation in the form of a power law. Similar parametrization can be done for tensor perturbations, with A_T and n_T the amplitude and spectral index of the power law, respectively. The tensor-to-scalar ratio, as the name suggests, is defined as $r = A_T/A_s$. As primordial gravitational waves are expected to generate tensor perturbations to the metric, the tensor-to-scalar ratio r is often used to parameterize the expected size of the primordial gravitational wave signal, as will be used in Chapter 2. The tensor spectral index n_T, on the other hand, is often fixed as $n_T = -r/8$, known as the "consistency relation" [15].

As the physics of the early universe gets imprinted in the cosmic microwave background, precision measurements of the CMB anisotropies will allow us to put stringent constraints on the cosmological parameters and validate our cosmological model.

1.2 Cosmic microwave background

The discovery of the Cosmic Microwave Background (CMB) is an interesting story by itself. Early in 1940, Andrew McKellar had noted based on interstellar absorption lines that the population of excited rotational states of CN molecules is consistent with being in thermal equilibrium with a background temperature of $\sim 2.3\,\mathrm{K}$ [17], and similar results were noted by Walter Adam in 1941 [18], both of which were likely early evidences of the CMB, though little attention was paid to their results. Subsequently in 1955, Emile Le Roux noted an isotropic emission at a wavelength of $\lambda = 33\,\mathrm{cm}$ corresponding to a blackbody temperature of $T = 3 \pm 2\,\mathrm{K}$ [19], and a similar observation was made by T.A. Shmaonov in 1957 at a wavelength of $\lambda = 3.2\,\mathrm{cm}$ that corresponds to a blackbody temperature of $4 \pm 3\,\mathrm{K}$ [20]. The significance of their results were unappreciated at the time. Finally in 1965, two astronomers, Penzias and Wilson, while working on long-distance radio communications at the Bell Laboratories, discovered, quite unexpectedly, a uniform noise source across the sky. They soon realized its importance from a talk given by P.J.E Peebles in Princeton and published their results in a short paper titled "measurement of excess antenna temperature at $\lambda = 7.3\,\mathrm{cm}$" [21]. Their results were soon confirmed by Dicke, Peebles, Roll, and Wilkinson in Princeton, fully explaining the implications [22], and the scientific significance of the signal was finally realized. CMB has since then become the cornerstone of our understanding of the universe.

As the oldest light in the universe, the CMB was formed when the universe was $\sim 400,000\,\mathrm{yrs}$ old when it was still a hot and dense plasma. As the universe expands and cools, the CMB photons decouple from electrons and free-stream across space to reach us today. The presence of the CMB is a compelling evidence of the hot big bang model first proposed by George Gamow [23]. The observed CMB is uniform across the sky, fluctuating only on the level of a few parts in 10^5, following a blackbody spectrum with a mean temperature of $2.725\,\mathrm{K}$. The remarkable uniformity in the observed CMB is a compelling evidence of the isotropy of the universe on large scale, and it also poses a challenge known as the horizon problem in understanding the uniformity of CMB temperature above the degree scale which are too far apart to have established any causal contact in the past. This eventually leads

to the hypothesis of inflation which proposes a period of exponentially fast expansion of the universe that allows such causal contacts to be established above degree scale in the CMB sky (see [24] for a pedagogical review). In addition, the anisotropies of CMB, despite being tiny, also carry important cosmological information on the density fluctuations in the early universe, produced from the quantum fluctuations during inflation.

1.2.1 CMB temperature

We can define $\Theta(\hat{n}) = \delta T(\hat{n})/T$ to denote the anisotropies in CMB temperatures. It can be decomposed into spherical harmonics as

$$\Theta(\hat{\mathbf{n}}) = \sum_{l=0}^{\infty} \sum_{m=-l}^{l} a_{\ell m} Y_{\ell m}(\hat{\mathbf{n}}), \tag{19}$$

where $Y_{\ell m}$ is the spherical harmonic functions. The expansion coefficients can be reversely calculated as

$$a_{\ell m} = \int d\Omega \; \Theta(\hat{\mathbf{n}}) Y^*_{\ell m}(\hat{\mathbf{n}}) \tag{20}$$

Assuming that the fluctuations in CMB temperature follow Gaussian statistics, all the information about the field can be described using its 2-point correlation function, defined as

$$\langle \Theta(\hat{\mathbf{n}}) \Theta(\hat{\mathbf{n}}') \rangle = \frac{1}{4\pi} \sum_{l=0}^{\infty} (2\ell + 1) C_\ell P_\ell(\cos\theta) \tag{21}$$

with $\cos\theta \equiv \hat{\mathbf{n}} \cdot \hat{\mathbf{n}}'$ and $P_\ell(\cos\theta)$ the Legendre polynomial. C_ℓ is known as the CMB power spectrum and is often presented in the form of $\mathcal{D}_\ell \equiv C_\ell(\ell+1)\ell/2\pi$. The CMB power spectrum can be estimated using the following unbiased estimator

$$\widehat{C}_\ell = \frac{1}{2\ell + 1} \sum_{m=-\ell}^{\ell} |a_{\ell m}|^2. \tag{22}$$

The sum indicates that each ℓ mode in C_ℓ is estimated using $2\ell + 1$ measurements. As $a_{\ell m}$ follows a Gaussian distribution, C_ℓ follows a chi-square distribution with $2\ell + 1$ degrees of freedom for each ℓ mode. Hence, the variance of C_ℓ is given by [2]

$$\sigma^2(C_\ell) = \frac{2}{(2\ell + 1) f_{\rm sky}} C_\ell \tag{23}$$

[2]The variance of a chi-square distribution with ν degrees of freedom is 2ν.

where we have defined $f_{\rm sky}$ to approximately account for the effect of partial sky coverage as a reduction in the effective number of measurements. As ℓ gets lower (e.g., $\ell \lesssim 50$), the factor $1/(2\ell+1)$ causes the variance of the estimator to blow up. This is due to the lack of possible measurements that can be made at the large angular scales, causing an irreducible noise contribution known as the cosmic variance, which does not improve with better instruments.

The CMB power spectrum has been measured precisely by Planck [1], yielding cosmic variance limited measurements up to an augular scale of $\ell \lesssim 2000$. In Figure 1.3, we show the Planck measurements of the CMB power spectrum in temperature as compared to the best-fit ΛCDM model. It showcases the excellent agreement between data and our model. The CMB power spectrum in Figure 1.3 also shows a number of notable features: (1). The variance significantly increases at $\ell \lesssim 10$ due to cosmic variance. (2). The power spectrum features peaks and troughs. They are sourced by the photon-baryon coupling in the early universe that leads to sound-wave like acoustic oscillations of the over-density regions and is reflected in the CMB power spectrum. (3). The CMB power spectrum has the highest peak at $l \sim 220$ or $\sim 0.5^\circ$ in angle. This angular scale corresponds to the size of the sound horizon at Recombination which is largest possible distance traveled by the photon-baryon acoustic waves before Recombination. (4). The CMB power spectrum decays exponentially at large ℓ ($\ell \gtrsim 1500$). This is caused by the Silk damping effect which occurs when we have reached scales smaller than the mean free path of the photon and electron interaction (Thomson scattering) at Recombination where all density perturbations get washed out by photon diffusion.

1.2.2 CMB polarization

CMB photons can be polarized through Thomson scatterings when electrons couple to local quadrupole distributions of photons. As briefly discussed in 1.1, quadrupole photon distribution only starts to develop during decoupling, and so is the CMB polarization. This results in CMB being polarized at 10% level, with polarization anisotropies tracing the velocity perturbations and thus carry important information of the early universe that complements the temperature anisotropies. It is common to express the polarization mea-

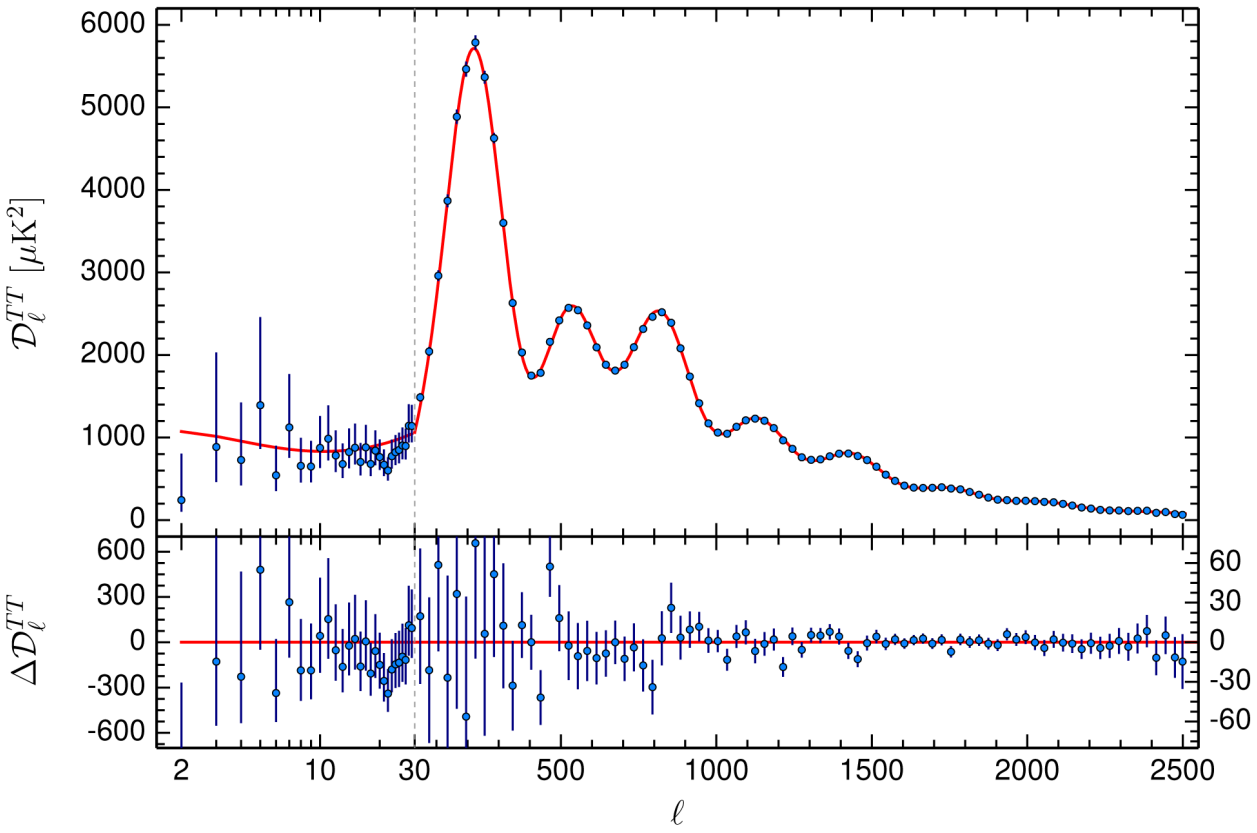

Figure 1.3: CMB temperature power spectrum measured from Planck 2015 are shown in comparison to the best-fit ΛCDM model (shown in red solid line). Image taken from Planck [1].

surements in terms of *Stokes parameters* I, Q, U, and V: consider a monochromatic wave with frequency ω_0 propagating along the $+z$ direction,

$$\begin{aligned} E_x(t) &= a_x \cos(\omega_0 t + \phi_x(t)), \\ E_y(t) &= a_y \cos(\omega_0 t + \phi_y(t)). \end{aligned} \tag{24}$$

The Stokes parameters can be defined as time averages

$$\begin{aligned} I &= \langle a_x^2 \rangle + \langle a_y^2 \rangle, \\ Q &= \langle a_x^2 \rangle - \langle a_y^2 \rangle, \\ U &= \langle 2 a_x a_y \cos(\theta_x - \theta_y) \rangle, \\ V &= \langle 2 a_x a_y \sin(\theta_x - \theta_y) \rangle. \end{aligned} \tag{25}$$

In particular, I describes the total intensity of the light, Q and U describe the linear polarization of the light, and V describes the circular polarization. CMB are expected to be linearly polarized due to Thomson scattering but not circularly polarized, which is consistent with observations from Planck [1].

Define complex stoke parameters ${}_{\pm 2}A(\hat{\mathbf{n}}) \equiv Q(\hat{\mathbf{n}}) \pm iU(\hat{\mathbf{n}})$, it can be decomposed as

$${}_{\pm 2}A(\hat{\mathbf{n}}) = \sum_{lm} {}_{\pm 2}A_{lm} \; {}_{\pm 2}Y_{lm}(\hat{\mathbf{n}}), \tag{26}$$

where ${}_{\pm 2}Y_{lm}(\hat{\mathbf{n}})$ are spin-weighted spherical harmonics given by Ref. [25]. The coefficients ${}_{\pm 2}A_{lm}$ can further be combined to form rotationally invariant combinations

$$\begin{aligned} a_{lm}^E &= \frac{1}{2} \left[{}_{+2}A_{lm} + {}_{-2}A_{lm} \right], \\ a_{lm}^B &= \frac{1}{2i} \left[{}_{+2}A_{lm} - {}_{-2}A_{lm} \right], \end{aligned} \tag{27}$$

where a_{lm}^E and a_{lm}^B are known as the the curl-free "E-mode" and the gradient-free "B-mode" of the polarization field, respectively, as shown schematically in Figure 1.4. The figure shows that the E-mode polarization features an even parity when flipped, while the B-mode

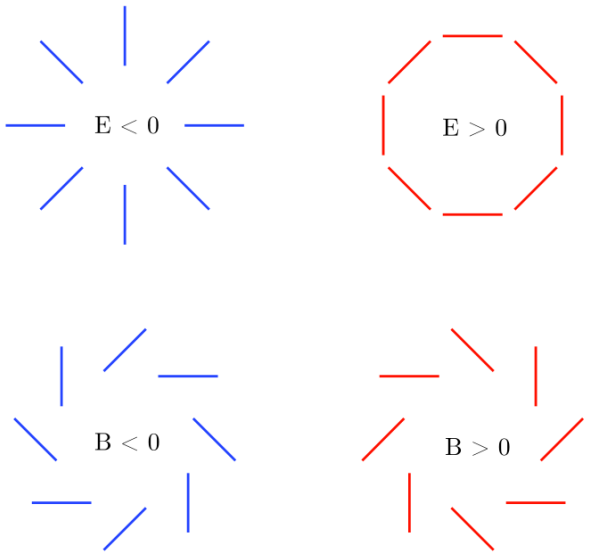

Figure 1.4: Schematics illustrating the E-mode and B-mode signal. In particular, B-mode features a handedness that changes sign when flipped. Image taken from [3].

polarization features an odd parity. The power spectra of E- and B-mode polarization, including the cross spectrum with temperature, are given by

$$\begin{aligned}
\langle a^{E*}_{lm} a^{E}_{l'm'} \rangle &= \delta_{ll'}\delta_{mm'} C^{EE}_l, \\
\langle a^{B*}_{lm} a^{B}_{l'm'} \rangle &= \delta_{ll'}\delta_{mm'} C^{BB}_l, \\
\langle a^{T*}_{lm} a^{E}_{l'm'} \rangle &= \delta_{ll'}\delta_{mm'} C^{TE}_l, \\
\langle a^{T*}_{lm} a^{B}_{l'm'} \rangle &= \delta_{ll'}\delta_{mm'} C^{TB}_l, \\
\langle a^{E*}_{lm} a^{B}_{l'm'} \rangle &= \delta_{ll'}\delta_{mm'} C^{EB}_l.
\end{aligned} \tag{28}$$

Among the set of six power spectra (including C^{TT}_l), C^{EB}_l and C^{TB}_l are parity-odd whereas the rest are parity-even. As there is no evidence that the CMB anisotropies feature an odd parity, we expect $C^{EB}_l = C^{TB}_l = 0$. In practice, these two spectra are often used to test for instrumental systematics [26]. Thus the non-zero power spectra of interests to us are C^{TT}_l, C^{TE}_l, C^{EE}_l, and C^{BB}_l.

The decomposition of CMB polarization into E-mode and B-mode is well motivated as scalar density perturbations only induce E-mode polarization. As previously discussed,

CMB E-mode polarization can be generated through Thomson scatterings in the presence of a local quadruple photon distribution. B-mode polarization signal, on the other hand, can only be generated by tensor-mode density perturbation such as that caused by the primordial gravitational waves, which is the hypothesized gravitational waves generated during the inflationary epoch sourced by the exponential expansion of spacetime. Detecting such signal will be a solid evidence of inflation and acts as a smoking gun for inflationary models [27]. Therefore, it is one of the most important scientific targets for the current and upcoming CMB experimental efforts. It is also worth noting that, in addition to primordial gravitational waves, CMB lensing effect – a deflection of the CMB photon from its propagation path as it traverses gravitational potentials of the large scale structures – is also known to induce B-mode polarization in the CMB, and may pose a challenge as a source of confusion in the CMB B-mode signal [28].

Figure 1.5 shows the expected CMB power spectra for both temperature and polarization. It shows a few notable features: (1). The E-mode polarization power spectrum is about ~ 2 orders of magnitude lower than the temperature (TT) power spectrum, indicating that CMB is polarized at $\sim 10\%$ level. (2). The E-mode power spectrum features acoustic oscillations that are out of phase with the temperature power spectrum. This is because the CMB polarization field traces the velocity perturbations of the acoustic oscillations which is $\pi/2$ out of phase with the density perturbation, similar to the case of a harmonic oscillator. (3). The TE cross spectrum shows that the temperature and E-mode polarization maps are correlated at $\sim 20\%$ level. (4). The B-mode power spectrum is dominated by the signal from CMB lensing for $\ell \gtrsim 100$, and the B-mode signal from primordial gravitational wave is likely most prominent in the large scales at $\ell \lesssim 100$, which correspond to angles above a degree. The tensor-mode signal from the primordial gravitational waves is known up to a undetermined amplitude which characterizes the amplitude of the tensor-mode perturbation in the earlier universe. It is parameterized using the tensor-to-scale ratio r that denotes the ratio between the amplitude of primordial tensor power spectra and the primordial scalar power spectra.

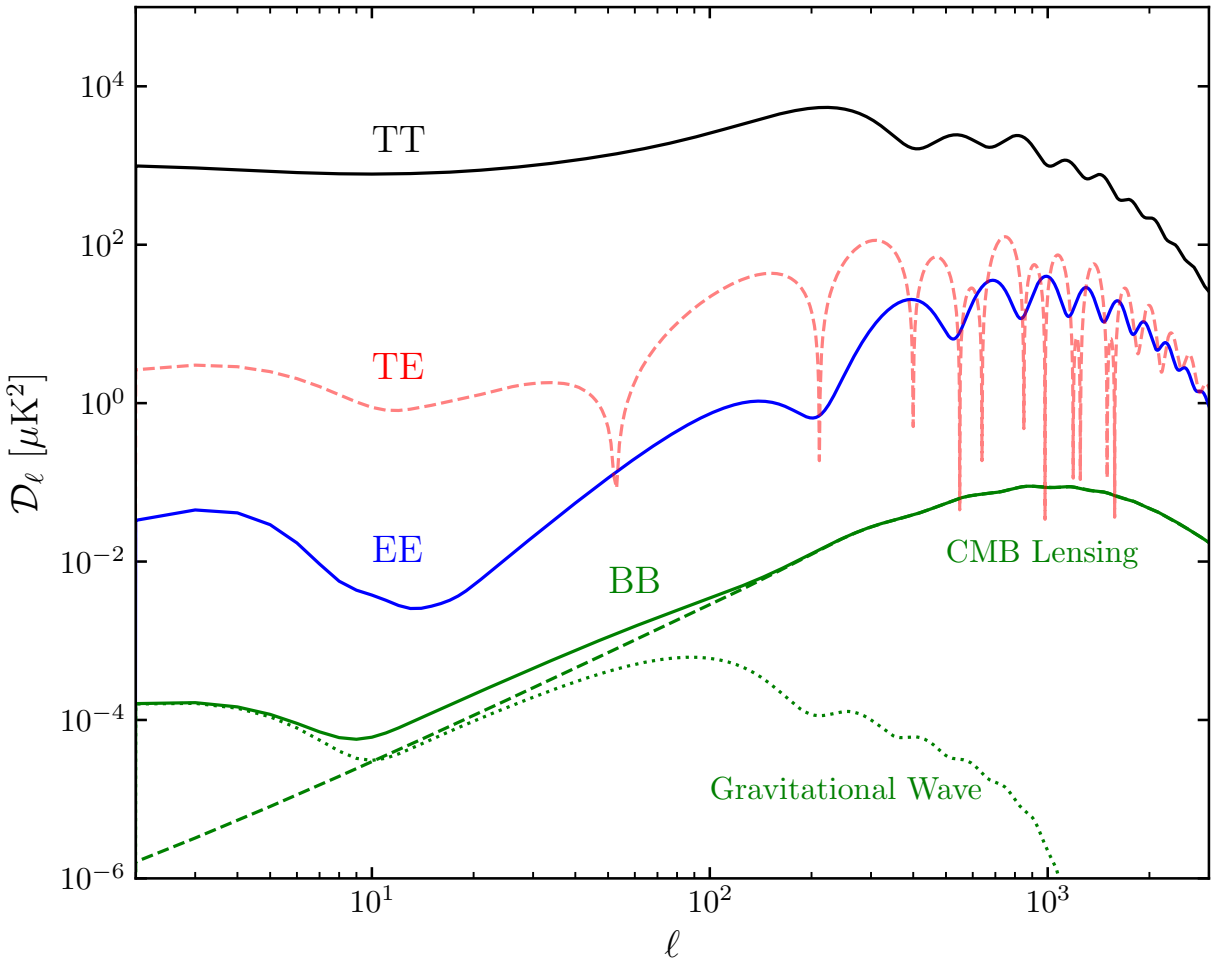

Figure 1.5: CMB power spectra calculated using CAMB [2]. The power spectra $\mathcal{D}_\ell \equiv C_\ell(\ell+1)\ell/2\pi$ for temperature (TT), E-mode (EE), and B-mode (BB) are shown as solid lines in black, blue, and green, respectively. The TE cross spectrum is shown as a red dashed line in its absolute value. In addition, the B-mode polarization has contributions from CMB lensing effect (shown as the green dashed line) and primordial gravitational wave (shown as the green dotted line).

2.0 Impacts of Primordial Magnetic Field on the Future B-mode Searches in the Cosmic Microwave Background

In this chapter I describe a work in which we try to answer the question – whether a signal from the primordial magnetic field may confuse us as the signal from the primordial gravitational waves from inflation in the CMB? The content of this chapter is based on a manuscript led by me which has been submitted to Physical Review D journal for publication.

2.1 Introduction

One of the primary goals of the next generation CMB experiments is to detect the primordial B-mode signal from the tensor perturbations generated by inflation. A detection of such signal will be a solid evidence of inflation and allow us to discriminate various inflationary models. The current best constraint on the tensor-to-scalar ratio is $r < 0.056$ at 95% confidence level through a combined analysis of Planck and BICEP2 [29]. This bound is expected to be lowered to $r \sim 10^{-3}$ by the upcoming CMB experiments such as the Simons Observertory [30], BICEP3 [31], LiteBIRD [32], and CMB-S4 experiment [33]. However, the tensor perturbations from inflation may not be the only source of B-mode polarization in the CMB. Foregrounds and lensing, in particular, both are known to contribute B-mode polarization – we have measured both. Polarized dust emission, in particular, is an important nuisance that confuses B-mode signal. The cautionary tale from BICEP which confused dust as inflationary signal has taught us that we need to carefully account for B-mode foregrounds in order to separate them from any primordial signal [34, 35, 36]. In order to do this, the coming generation of large-angle B-mode experiments (BICEP3, Simons Observatory, LiteBIRD) will measure in many frequency bands and test the spatial isotropy of any signal.

We also have known for a long time that the lensing B-mode signal has a low-ℓ contribution whose power spectrum can be mistaken for or confused with a low-amplitude primordial signal [37]. We have made great progress at measuring lensing signals through their non-

Gaussian 4-point signature (see, e.g., [38]), and now reconstruct maps of the lensing deflection potential from ACT [39], SPT [40], and Planck data [41]. In principle, this can be done with very high precision, given clean enough maps with low enough noise (see, e.g., [42, 28]). But in practice there is a limit to how well low-ℓ lensing can be reconstructed due to having imperfect data with non-zero noise. For example, although detecting a signal with $r \sim 10^{-6}$ is theoretically achieveable without considering any systematic noise, sky cut, and foreground [28], realistic forecasts that include such effects generally predict a much lower sensitivity at the level of $\sigma(r) \sim 10^{-3}$ [43].

Foregrounds and lensing are the two most important confusion signals for primordial B-mode polarization, and detailed studies and modeling of those are well in hand (see [44] for a review). What else could confuse us? Perhaps the next most-likely signal would be from a primordial magnetic field. Such concern has previously been brought up in, e.g., Refs. [45, 46], and discussed in Ref. [47]. While the signal from PMF may not be completely degenerate with the primordial tensor signal, as one might argue, to what extent can we distinguish the two sources, given imperfect data with non-zero noise, is unclear and deserves more attention, thus motivating the present study.

Primordial magnetic field is proposed to explain the ubiquitous magnetic field found in the universe, with strengths of a few micro-Gauss (μG) extending across galactic and cluster scales (see [48] for a review). Furthermore, evidence from the non-observation of the inverse compton cascade γ-rays from the TeV blazars [49] suggests that magnetic field may even be present in the inter-galactic medium, with a lower limit of $\sim 10^{-7}$ nano-Gauss (nG), extending across mega-parsec (Mpc) scale. On the other hand, the physical origin of the cosmic magnetic field remains poorly understood. One intriguing possibility is that cosmic magnetic fields are present before the structure formation and are produced in the very early universe such as during inflation [50] or during the phase transitions [51]. Such magnetic fields that are present before the decoupling of CMB photons are known as the primordial magnetic field (PMF hereafter).

If present, PMF impacts both ionization history and structure formation of the universe, leaving imprints on the CMB and the matter power spectrum [52]. In particular, PMF sources all kinds of metric perturbations including scalar, vector, and tensor types, and

influences the baryonic physics through the effect of Lorentz force. In addition, PMF also introduces a net rotation of the linear polarization of the CMB photons through an effect known as the Faraday rotation which leaves observable pattern in the CMB polarization power spectrum [53].

On the other hand, PMF is not well constrained by the existing observations. The amplitude of the comoving magnetic field B_0 present today is constrained to be no more than a few nG (see, e.g., [54, 55]). However, it has been previously shown that a field of $\sim 1\,\mathrm{nG}$ is large enough to generate a degenerate pattern in CMB B-mode power spectrum as an inflationary tensor-mode signal with $r \sim 0.004$ [47] which is the targeting value of the upcoming CMB experiments. Hence, a lack of knowledge on the PMF may potentially leads us to a wrong conclusion if a tensor-mode signal were to be detected by the upcoming CMB experiments. Therefore, it is important to evaluate the extent of the confusion between the two degenerate models beforehand.

In this work we aim to review and re-evaluate, with particular focus on the upcoming CMB experiments, the potential degeneracy between a B-mode signal from a PMF model and that from primordial gravitational waves (sometimes also referred to as the primordial tensor-mode signal in the text). In particular, we evaluate the degeneracy for different targets of tensor-to-scalar ratio r, in the context of different experimental settings that emulate the sensitivity of the upcoming CMB experiments. Additionally, we also investigate the extent of which we can break the degeneracy with the help of the Faraday rotation effect from magnetic field, in both the power spectrum level and the map level, as discussed in details in Section 2.4 and Section 2.5, respectively.

This chapter is organized as the following. In Section 2.2, we review the basics of the primordial magnetic field. In Section 2.3, we briefly review the PMF contributions to the CMB power spectrum and evaluate the potential confusion to the tensor-mode signal from inflation. In Section 2.4, we briefly review the physics of Faraday rotation from PMF and discuss to what extent this effect allows us to break the degeneracy between PMF and primordial tensor-mode signals. In Section 2.5, we first review the reconstruction of Faraday rotation through quadratic estimators and then discuss to what extent it helps us break the degeneracy. Finally, we discuss our results and conclude in Section 2.6.

2.2 Primordial magnetic field

2.2.1 Statistics of stochastic magnetic fields

We consider a stochastic background of magnetic fields generated prior to recombination and shall assume that the magnetic field is weak enough to be treated as a perturbation to the main background density in the universe. As the universe is highly conductive prior to recombination, any electric field generated quickly dissipates, while magnetic field is effectively "frozen-in" due to the negligible magnetic diffusion on the cosmological scales. Hence, the conservation of magnetic flux gives the scaling relation $B^i(x^j, \tau) = B^i(x^j)/a(\tau)^2$, with a the scale factor, τ the conformal time, and x^j the comoving coordinates. We shall also assume that the stochastic background of magnetic fields follows the statistics of a Gaussian random field, and the energy density of magnetic fields, which scales quadratically with the magnetic field strength ($\propto B^2$), follows a chi-square statistics. In Fourier space [1], the statistics of the magnetic fields can be completely described by its 2-point correlation function,

$$\langle B_i^*(\mathbf{k}) B_j(\mathbf{k}') \rangle = (2\pi)^3 \delta^{(3)}(\mathbf{k} - \mathbf{k}') [P_{ij} P_B(k) + i\epsilon_{ijl} \hat{k}_l P_H(k)], \tag{29}$$

where $P_{ij} \equiv \delta_{ij} - \hat{k}_i \hat{k}_j$ is a projection operator to the plane transverse to $\hat{k}$ such that $P_{ij} k_j = 0$, and ϵ_{ijl} is the total anti-symmetric tensor. Here P_H and P_B refer to the helical and non-helical part of the magnetic field power spectrum, respectively. For the interests of simplicity we shall assume that the helical magnetic field component vanishes, though we should note that helical magnetic field is predicted by some proposed magnetogenesis scenarios (see, e.g., [56, 57]).

We assume that the power spectrum of magnetic field follows a power law with a cut-off scale k_D, given by

$$P_B = A_B k^{n_B}, \quad k \leq k_D, \tag{30}$$

which vanishes for $k > k_D$. The dissipation scale k_D reflects the suppression of magnetic field due to radiation viscosity in the small scales. A_B and n_B denote the amplitude and

[1] In this chapter we used the following Fourier convention:
$\tilde{f}(\mathbf{k}) = \int d^3x \; e^{i\mathbf{k}\cdot\mathbf{x}} f(\mathbf{x})$, and $f(\mathbf{x}) = \frac{1}{(2\pi)^3} \int d^3k \; e^{-i\mathbf{k}\cdot\mathbf{x}} \tilde{f}(\mathbf{k})$.

spectral index of magnetic field power spectrum, respectively, both of which are sensitive to the specific magnetogensis scenerios. In particular, an inflationary magnetogenesis model prefers a scale-invariant spectrum with a spectral index $n_B \approx 3$, while a causally-generated magnetic field in the post-inflationary epoch prefers a spectrum with $n_B \geq 2$ [46]. Following the conventions in literature, we smooth magnetic field with a Gaussian kernel $f_\lambda(x) = N \exp(-x^2/2\lambda^2)$ on a comoving scale of $\lambda = 1\,\mathrm{Mpc}$. The magnetic field fluctuation on the comoving scale of λ can then be characterized by B_λ^2,

$$B_\lambda^2 \equiv \langle \mathbf{B}_\lambda(\mathbf{x}) \cdot \mathbf{B}_\lambda(\mathbf{x}) \rangle = \frac{1}{\pi^2} \int_0^\infty dk\ k^2 e^{-k^2\lambda^2} P_B(k), \tag{31}$$

which relates to the power spectrum amplitude A_B by

$$A_B = \frac{(2\pi)^{n_B+5} B_\lambda^2}{2\Gamma(\frac{n_B+3}{2}) k_\lambda^{n_B+3}}. \tag{32}$$

The damping scale k_D can also be approximated as [58],

$$\begin{aligned} k_D = (5.5 \times 10^4)^{\frac{1}{n_B+5}} \left(\frac{B_\lambda}{1\,\mathrm{nG}}\right)^{-\frac{2}{n_B+5}} \left(\frac{2\pi}{\lambda/\mathrm{Mpc}}\right)^{\frac{n_B+3}{n_B+5}} \\ \times h^{\frac{1}{n_B+5}} \left(\frac{\Omega_b h^2}{0.022}\right)^{\frac{1}{n_B+5}} |_{\lambda=1\mathrm{Mpc}}\ \mathrm{Mpc}^{-1}, \end{aligned} \tag{33}$$

with h the reduced Hubble parameter defined as $h \equiv H_0/100\,\mathrm{km\,s^{-1}\,Mpc^{-1}}$.

2.2.2 Magnetic perturbations

Consider a particular realization of stochastic background of magnetic fields, with the magnitude of the field at x and conformal time τ given by $B^i(\mathbf{x}, \tau)$, its energy-momentum tensor can be written as

$$\begin{aligned} T^0{}_0 &= -\frac{1}{8\pi a^4} B^2(\mathbf{x}), \\ T^0{}_i &= T^i{}_0 = 0, \\ T^i{}_j &= \frac{1}{4\pi a^4}\left[\frac{1}{2} B^2(\mathbf{x})\delta^i{}_j - B^i(\mathbf{x}) B_j(\mathbf{x})\right], \end{aligned} \tag{34}$$

where we have used the "freeze-in" condition $B^i(\mathbf{x}, \tau) = B^i(\mathbf{x})/a(\tau)^2$. For notation brevity we shall omit the time dependence by implicitly assuming $\tau = \tau_0$, with τ_0 the conformal time today; the generic expression at different redshifts can then obtained by simple scaling. We note that magnetic fields, being part of the rank-2 tensor, are not invariant under general coordinate transformations. Thus the form of energy-momentum tensor in Equation 34 is valid only in one particular frame; in this case, it is in the "cosmic rest frame", in which cosmic radiation field is isotropic, that we can assume the form of energy-momentum tensor in Equation 34. As we consider magnetic perturbations to be fully inhomogeneous and perturbatively small (i.e. no homogeneous background component), the magnetic perturbations are invariant under *infinitesimal* coordinate transformations *up to the leading order*. In this sense, magnetic perturbations are manifestly gauge invariant[2].

The spatial part of the magnetic energy-momentum tensor can be written as

$$T_{ij}(\boldsymbol{x}) = \frac{1}{4\pi}\left[\frac{1}{2}\delta_{ij} B^2(\boldsymbol{x}) - B_i(\boldsymbol{x}) B_j(\boldsymbol{x})\right], \tag{35}$$

and in Fourier space, multiplications become convolutions,

$$\tilde{T}_{ij}(\boldsymbol{k}) = \frac{1}{4\pi}\int \frac{d^3p}{(2\pi)^3}\left[\frac{1}{2}\delta_{ij}\tilde{B}_l(\boldsymbol{p})\tilde{B}_l(\boldsymbol{k}-\boldsymbol{p}) - \tilde{B}_i(\boldsymbol{p})\tilde{B}_j(\boldsymbol{k}-\boldsymbol{p})\right]. \tag{36}$$

[2]This conclusion holds in general when perturbations that are vanishing or constant in the background, that they are automatically gauge-invariant; it is known as the Stewart-Walker lemma [59].

The magnetic field energy momentum tensor induces scalar, vector, and tensor perturbations. In particular, the scalar perturbations are given by

$$\begin{aligned} \rho_B &= 3\mathcal{P}_B = -\delta^{ij}\tilde{T}_{ij}, \\ L_B &= \hat{k}^i\hat{k}^j\tilde{T}_{ij}, \\ \sigma_B &= S^{ij}\tilde{T}_{ij}, \end{aligned} \tag{37}$$

where we defined traceless tensor $S^{ij} \equiv \hat{k}^i\hat{k}^j - \frac{1}{3}\delta^{ij}$. $\rho_B = -T^0{}_0$ is the energy density perturbation from magnetic field, and $\mathcal{P}_B$ is the pressure perturbation which is related to the energy density by $\rho_B = 3\mathcal{P}_B$ consistent with that of photons. L_B can be interpreted as the scalar part of the Lorentz force, and σ_B is the anisotropic stress perturbation (see, e.g., Ref. [60]). Note that the three scalar perturbations defined in Equation 37 are not independent as they are related by $\sigma_B = L_B + \frac{1}{3}\rho_B$; this allows us to consider only two out of three scalar perturbations, or in other words, there are only two independent scalar degrees of freedom.

The scalar perturbations defined in Equation 37 are relevant as they source scalar metric perturbations through the Einstein equation. Following the notations in Ref. [12] and in Conformal Newtonian Gauge, the metric perturbation, $\delta g_{\mu\nu}$, can be parametrized with $\delta g_{00} = 2a^2\psi$, $\delta g_{0i} = a^2 w_i$, and $\delta g_{ij} = -a^2(2\phi\delta_{ij} + \chi_{ij})$, where χ_{ij} is a traceless tensor. The quantity ϕ and ψ are sourced by magnetic scalar perturbations defined in Equation 37,

$$\begin{aligned} k^2\phi + 3\frac{\dot{a}}{a}\left(\dot{\phi} + \frac{\dot{a}}{a}\psi\right) &= 4\pi G a^2\left(\sum_n \rho_n\delta_n + \rho_B\right), \\ k^2\left(\dot{\phi} + \frac{\dot{a}}{a}\psi\right) &= 4\pi G a^2 \sum_n (\rho_n + P_n)\theta_n, \\ \ddot{\phi} + \frac{\dot{a}}{a}(\dot{\psi} + 2\dot{\phi}) + \left(2\frac{\ddot{a}}{a} - \frac{\dot{a}^2}{a^2}\right)\psi + \frac{k^2}{3}(\phi - \psi) &= \frac{4\pi}{3}G a^2\left(\sum_n c_{sn}^2\rho_n\delta_n + \frac{\rho_B}{3}\right), \\ k^2(\phi - \psi) &= 12\pi G a^2\left(\sum_n (\rho_n + P_n)\sigma_n + \sigma_B\right), \end{aligned} \tag{38}$$

where we have adopted the notations in Ref. [12] with ρ_n, P_n the density and pressure density of a particular component n, δ_n, θ_n, σ_n the density, velocity, and anisotropic stress perturbation from this component, and $c_{sn} = \delta P_n/\delta\rho_n$ the corresponding sound speed. In addition

to the effects of ρ_B and σ_B, Lorentz force also affects the evolution of baryon fluid through

$$\dot{\theta}_b = -\mathcal{H}\theta_b + k^2 c_{sb}^2 \delta_b - k^2 \frac{L_B}{\rho_b}, \tag{39}$$

with $\mathcal{H}$ the conformal Hubble factor defined as $\mathcal{H} \equiv a'/a$. As we are considering stochastic background of magnetic fields, the relevant quantity is not ρ_B, σ_B, and L_B but their two-point correlation functions. We can define the two-point correlation function of the spatial part of the energy momentum tensor as $C_{abcd}(\boldsymbol{k}, \boldsymbol{k'}) \equiv \langle T^*_{ab}(\boldsymbol{k}) T_{cd}(\boldsymbol{k'})\rangle$, and one can then obtain the two-point correlation function of the scalar perturbation modes as [52],

$$\begin{aligned}
\langle \rho_B^*(\boldsymbol{k})\rho_B(\boldsymbol{k'})\rangle &= \delta^{ij}\delta^{lm} C_{ijlm} = \frac{\delta^{(3)}(\boldsymbol{k}-\boldsymbol{k'})}{32\pi^2}\int d^3q\ P_B(q)P_B(|\boldsymbol{k}-\boldsymbol{q}|)(1+\mu^2),\\
\langle \sigma_B^*(\boldsymbol{k})\rho_B(\boldsymbol{k'})\rangle &= S^{ij}\delta^{lm} C_{ijlm} = \frac{\delta^{(3)}(\boldsymbol{k}-\boldsymbol{k'})}{12\pi^2}\int d^3q\ P_B(q)P_B(|\boldsymbol{k}-\boldsymbol{q}|)\\
&\qquad \times \left[1 - \frac{3}{2}(\gamma^2+\beta^2) + \frac{3}{2}\gamma\beta\mu - \frac{1}{2}\mu^2\right],\\
\langle \sigma_B^*(\boldsymbol{k})\sigma_B(\boldsymbol{k'})\rangle &= S^{ij}S^{lm} C_{ijlm} = \frac{\delta^{(3)}(\boldsymbol{k}-\boldsymbol{k'})}{18\pi^2}\int d^3q\ P_B(q)P_B(|\boldsymbol{k}-\boldsymbol{q}|)\\
&\qquad \times \left[1 - \frac{3}{4}(\gamma^2+\beta^2) + \frac{9}{4}\gamma^2\beta^2 - \frac{3}{2}\gamma\beta\mu + \frac{1}{4}\mu^2\right],
\end{aligned} \tag{40}$$

with $\gamma \equiv \hat{k}\cdot\hat{q}$, $\beta \equiv \hat{k}\cdot\hat{p}$, $\mu \equiv \hat{p}\cdot\hat{q}$, and $\hat{p} \equiv \widehat{(k-q)}$. In doing so we have also used Wick's theorem to expand 4-point correlation functions, which relies on the assumption that the stochastic magnetic fields background follows Gaussian statistics. We note that the two-point correlation functions will be sensitive to cut-off scales k_D when magnetic power spectrum are significantly blue-tilted, but such dependence is nonetheless not unphysical as the dissipation scale k_D corresponds to a measurable physical scale.

Similarly, the vector perturbations from T_{ij} can be expressed as

$$T_{ij}^{(V)} = \Pi_i^{(V)}\hat{k}_j + \Pi_j^{(V)}\hat{k}_i \tag{41}$$

with $\Pi_i^{(V)}$ being a divergenceless three vector, $\hat{k}^i\Pi_i^{(V)} = 0$. This allows one to obtain $\Pi_i^{(V)}$ by constructing [58],

$$\Pi_i^{(V)} = \hat{k}^m T_{mi} - \hat{k}_i\hat{k}^m\hat{k}^n T_{mn} = P^n{}_i\hat{k}^m T_{mn}, \tag{42}$$

where we have defined $P^n{}_i \equiv \delta^n{}_i - \hat{k}^n \hat{k}_i$. In the infinite conductivity limit[3], the vector perturbation $\Pi_i^{(V)}$ relates to the divergenceless part of Lorentz force, L_i, by $L_i = k\Pi_i^{(V)}$ [58]. The two-point function of $\Pi_i^{(V)}$ is given by

$$\begin{aligned}\langle \Pi_i^{*(V)}(\boldsymbol{k}) \Pi_j^{(V)}(\boldsymbol{k'}) \rangle &= \hat{k}^a P^b{}_i(\boldsymbol{k}) \hat{k}'^c P^d{}_j(\boldsymbol{k'}) C_{abcd} \\ &= P_{ij}(\boldsymbol{k}) \frac{\delta^{(3)}(\boldsymbol{k}-\boldsymbol{k'})}{32\pi^2} \int d^3p \; P_B(p) P_B(|\boldsymbol{k}-\boldsymbol{p}|) \\ &\quad \times \left[(1+\beta^2)(1-\gamma^2) + \gamma\beta(\mu - \gamma\beta)\right].\end{aligned} \tag{43}$$

If we denote the vector-type metric perturbation as $\delta g_{0i}^{(V)} = -a^2 V_i$, it can then be sourced by $\Pi_i^{(V)}$ as

$$\dot{V}_i + 2HV_i' = -16\pi G \frac{\Pi_i^{(V)}}{a^2 k}. \tag{44}$$

In addition, the vector part of Lorentz force, L_i, also affects the baryon evolution in a similar way as Equation 39, given by [58]

$$\dot{\Omega}_{bi} + \frac{\dot{a}}{a}\Omega_{bi} - \frac{\dot{\tau}}{R}(v_{\gamma i}^{(V)} - v_{bi}^{(V)}) = \frac{L_i}{a^4(\rho_b + p_b)}, \tag{45}$$

with Ω_{bi}, $v_{bi}^{(V)}$ the vorticity and the divergenceless velocity perturbation of baryons, respectively, and $v_{\gamma i}^{(V)}$ the divergenceless velocity perturbation of photons.

Similarly, the tensor perturbations $\Pi_{ij}^{(T)}$ from T_{ij} can be expressed as

$$\Pi_{ij}^{(T)} = \left(P^m{}_i P^n{}_j - \frac{1}{2} P_{ij} P^{mn} \right) T_{mn}. \tag{46}$$

It sources tensor-type metric perturbation,

$$\ddot{h}_{ij}(\eta, \mathbf{k}) + 2\frac{\dot{a}}{a}\dot{h}_{ij}(\eta, \mathbf{k}) + k^2 h_{ij}(\eta, \mathbf{k}) = 8\pi G \Pi_{ij}^{(T)}(\mathbf{k})/a^2, \tag{47}$$

[3]the conductivity is to be compared with the hubble rate; near matter-radiation equality, $\sigma/H \sim 10^{22}(T/eV)^{-3/2} \gg 1$ (see Appendix in Ref. [61] for more detailed discussion), so in practice it can be considered infinite.

with h_{ij} the transverse-traceless part of the metric tensor perturbation, which accounts for gravitational radiation. The two-point correlation function of $\Pi_{ij}^{(T)}$ can be written as

$$\begin{aligned}\langle \Pi_{ij}^{*(T)}(\boldsymbol{k})\Pi_{tl}^{(T)}(\boldsymbol{k'})\rangle &= \left[P^a{}_i(\boldsymbol{k})P^b{}_j(\boldsymbol{k}) - \frac{1}{2}P_{ij}(\boldsymbol{k})P^{ab}(\boldsymbol{k})\right] \\ &\quad \times \left[P^c{}_t(\boldsymbol{k'})P^d{}_l(\boldsymbol{k'}) - \frac{1}{2}P_{tl}(\boldsymbol{k})P^{cd}(\boldsymbol{k})\right] C_{abcd} \\ &= \mathcal{M}_{ijtl}(\boldsymbol{k})\frac{\delta^{(3)}(\boldsymbol{k}-\boldsymbol{k'})}{64\pi^2}\int d^3p\ P_B(p)P_B(|\boldsymbol{k}-\boldsymbol{p}|) \\ &\quad \times (1+2\gamma^2+\gamma^2\beta^2),\end{aligned} \tag{48}$$

with $\mathcal{M}_{ijtl} \equiv P_{it}P_{jl} + P_{il}P_{jt} - P_{ij}P_{tl}$.

Note that as the 2-point correlation functions between different perturbations are proportional to the 4-point correlation function of magnetic fields, one can obtain the 2-point correlation functions at any conformal time τ by scaling the corresponding expressions with $a^{-8}(\tau)$ [52].

The question of particular interests to the discussion in this chapter is how does magnetic perturbations source B-mode polarization. We shall see that both vector-mode and tensor-mode perturbations from magnetic field can source B-mode polarization signal in the CMB. In particular, B-mode polarization can be expressed as a line-of-sight integral [62],

$$\frac{B_\ell^{(m)}(\eta_0,k)}{2\ell+1} = -\sqrt{6}\int_0^{\eta_0} d\eta\ \dot{\tau}e^{-\tau}P^{(m)}(\eta)\beta_\ell^{(m)}(k(\eta_0-\eta)), \tag{49}$$

with m denoting either vector mode (V) or tensor mode (T), and it relates to the B-mode power spectrum by

$$C_l^{\mathrm{BB(m)}} = \frac{4}{\pi}\int dk\ k^2 \frac{B_l^{(m)}(\eta_0,k)}{2l+1}\frac{B_l^{(m)*}(\eta_0,k)}{2l+1}. \tag{50}$$

In particular, for vector and tensor modes respectively,

$$\beta_\ell^{(V)}(x) = \frac{1}{2}\sqrt{(\ell-1)(\ell+2)}\frac{j_\ell(x)}{x}, \quad \beta_\ell^{(T)} = \frac{1}{2}\left[j'_\ell(x) + 2\frac{j_\ell(x)}{(x)}\right], \tag{51}$$

and

$$P^{(V)} = \frac{\sqrt{3}}{9}\frac{k}{\dot{\tau}}v_b^{(V)}, \quad P^{(T)} = -\frac{1}{3}\frac{\dot{h}}{\dot{\tau}}, \tag{52}$$

with $v_b^{(V)}$ the vector part of baryon velocity, and $\dot{h}$ the root-mean-square spectra defined as

$$\langle \dot{h}_{ij}(\eta, \mathbf{k}) \dot{h}_{kl}(\eta, \mathbf{k}') \rangle = \mathcal{M}_{ijkl}(\mathbf{k}) \delta(\mathbf{k} - \mathbf{k}') |\dot{h}(\eta, \mathbf{k})|^2, \tag{53}$$

with h_{ij} the transverse-traceless part of metric perturbation. As both $\dot{h}$ and $v_b^{(V)}$ can be sourced by magnetic field (as shown in Equation 45 and Equation 47), it is therefore expected that both the vector and tensor perturbations from magnetic fields source B-mode polarization pattern.

As magnetic fields may induce independent mode of metric perturbations to that of inflation, the initial conditions of magnetically-induced modes can be decomposed into three types: (1) compensated [63, 64], (2) passive [65, 52], and (3) inflationary [66] magnetic modes. In particular, compensated magnetic mode arises when the magnetic contributions to the metric perturbations are compensated by fluid modes to the leading order in the super-horizon scales. It includes the contributions from magnetic field after neutrino decoupling, and is finite in the $\tau \to 0$ limit. The passive magnetic mode, on the other hand, accounts for magnetic contribution prior to neutrino decoupling. In this period, the universe is dominated by a tightly-coupled radiative fluid which prevents any anisotropic stress from developing. Without neutrino free-streaming, magnetic field acts as the only source of anisotropic stress, leading to a logarithmically growing mode [65]. This logarithmically growing mode survives neutrino decoupling as a constant offset on the amplitude of the non-magnetic mode. Inflationary magnetic mode, as another type of initial condition, depends on specific generation mechanism [66], and is therefore not considered in this chapter in order to maintain generality of our results to different magnetic field models.

From the physical picture it is apparent that the size of the perturbations from magnetic field depends on the epoch of its generation relative to the epoch of neutrino decoupling, as can be parametrized by $\log_{10}(\tau_\nu/\tau_B)$, with τ_ν the neutrino decoupling time and τ_B the magnetic field generation time. Though the exact number for this quantity remains unknown and can be model-dependent, we shall assume $\log_{10}(\tau_\nu/\tau_B) = 17$ for simplicity following Ref. [67]. This is, nevertheless, without a loss of generality, as τ_ν/τ_B can be degenerate with the amplitude of the perturbations (e.g., B_λ or A_B) [52]. In addition, magnetic field also introduces a Lorentz force acting on the baryons in the primordial plasma. It effectively

augments the pressure perturbations of the baryon-photon fluid which prevent photons and baryons from falling into their gravitational wells. This effect is analogous to a change in baryon energy density which affects the sound speed of the baryon-photon fluid and change their acoustic oscillations [68, 69, 70].

2.3 Impacts on CMB power spectra

PMF influences CMB anisotropies through both the effect of metric perturbation and the Lorentz force and generates perturbations of scalar, vector, and tensor types. To study their impacts on the scientific goals of the upcoming CMB experiments, with particular focus on the CMB B-mode searches, we make use of the publicly available code MagCAMB [4] [54] which extends the Boltzmann code CAMB [71] to include the effects of PMF as we discussed in Section 2.2. In Figure 2.1 we show an example set of CMB power spectra that are sourced by a stochastic background of PMF with $B_{1\mathrm{Mpc}} = 1\,\mathrm{nG}$ and a nearly scale-invariant spectrum ($n_B = -2.9$). In particular, contributions from different magnetic modes are highlighted in different colors, from which one observes that the passive tensor-mode signal in C_ℓ^{BB} has significant power at $\ell \lesssim 100$ resembling that of an inflationary tensor-mode signal and hence may pose as a potential source of confusion. On the other hand, the compensated vector-mode contribution dominates at $\ell \gtrsim 1000$ in both C_ℓ^{TT} and C_ℓ^{BB} which is not degenerate with the inflationary tensor-mode signal. Hence, this vector-mode perturbation from PMF may give us a potential handle to break the degeneracy.

To evaluate the extent of the confusion for the upcoming CMB experiments, we simulate different sets of CMB power spectra using CAMB with the standard ΛCDM model and the Planck best-fit cosmological parameters as our fiducial model [1], while varying the tensor-to-scalar ratio r to reflect different science targets, with the spectral index n_T fixed by the consistency relation $n_T = -r/8$. In addition, we consider different experimental settings that emulate the targeting performance of some of the upcoming CMB experiments and simulate

[4] https://github.com/alexzucca90/MagCAMB

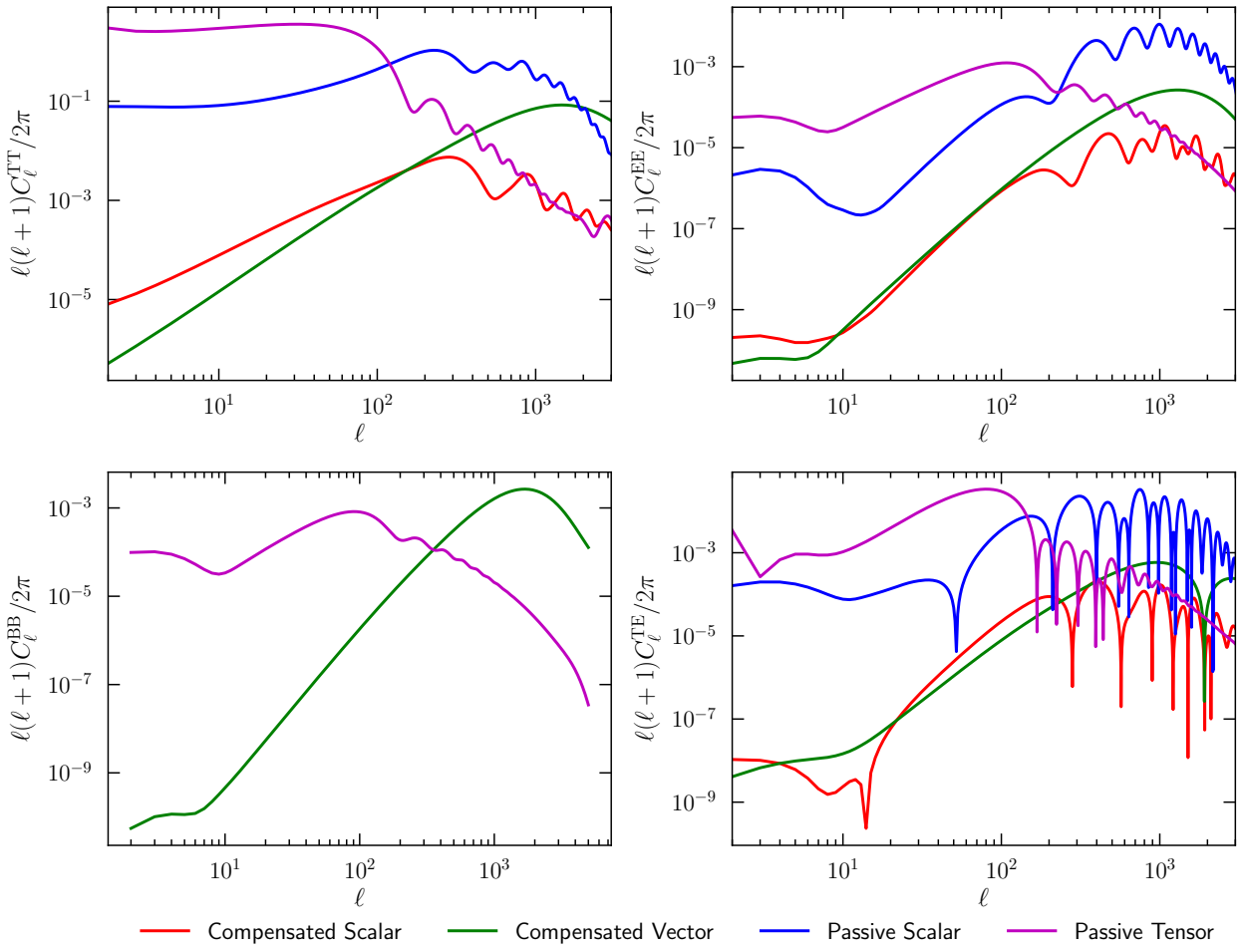

Figure 2.1: Contributions of different magnetic modes on the CMB power spectra from a stochastic background of PMF with $\mathrm{B}_{1\mathrm{Mpc}} = 1$ nG, $\log_{10}\tau_B/\tau_\nu = 17$, and $n_B = -2.9$ (nearly scale-invariant) generated using MagCAMB. Plots are in units of $\mu\mathrm{K}^2$.

the observed power spectra for each experiment with an idealistic noise model given by

$$N_\ell = w^{-1} \exp\left(\ell(\ell+1)\theta^2/8\ln 2\right), \tag{54}$$

where $w^{-1/2} \equiv \sqrt{4\pi\sigma_{\rm pix}^2/N_{\rm pix}}$ denotes the expected noise level of an experiment, with $\sigma_{\rm pix}$ the per-pixel noise level, $N_{\rm pix}$ the total number of pixels, and θ the full-width-half-minimum (FWHM) size of the telescope beam which we assume to be Gaussian. Additionally, we also assume that the noises in polarization and in temperature are related simply by $(\sigma_{\rm pix}^{\rm P})^2 = 2(\sigma_{\rm pix}^{\rm T})^2$.

With the simulated CMB power spectra, we then perform a Monte Carlo Markov Chain (MCMC) based model-fitting to find the best-fit cosmologies for two competing models: (1) a model with a non-zero tensor-to-scalar ratio r but no PMF contribution (ΛCDM+r hereafter); (2) a model with $r = 0$ but non-zero PMF contribution (ΛCDM+PMF hereafter). In particular, we find the best-fit cosmology using a maximum likelihood approach with the log-likelihood given by [72]

$$\begin{aligned} -2\ln\mathcal{L}\left(\left\{\hat{\mathbf{C}}_\ell\right\}|\{\mathbf{C}_\ell\}\right) = \sum_l (2l+1)\Bigg\{ &\mathrm{Tr}\left[\hat{\mathbf{C}}_\ell \mathbf{C}_\ell^{-1}\right] \\ &- \ln\left|\hat{\mathbf{C}}_\ell \mathbf{C}_\ell^{-1}\right| - 3\Bigg\}, \end{aligned} \tag{55}$$

where $\mathbf{C}_\ell$ contains the theory power spectra given by

$$\mathbf{C}_\ell \equiv \begin{pmatrix} C_\ell^{\rm TT} & C_\ell^{\rm TE} & 0 \\ C_\ell^{\rm TE} & C_\ell^{\rm EE} & 0 \\ 0 & 0 & C_\ell^{\rm BB} \end{pmatrix}, \tag{56}$$

and $\hat{\mathbf{C}}_\ell$ contains the observed power spectra given by

$$\hat{\mathbf{C}}_\ell \equiv \frac{1}{2\ell+1}\sum_m \boldsymbol{a}_{\ell m}\boldsymbol{a}_{\ell m}^\dagger, \tag{57}$$

with $\boldsymbol{a}_{\ell m} \equiv (a_{\ell m}^{\rm T} \;\; a_{\ell m}^{\rm E} \;\; a_{\ell m}^{\rm B})^T$. Note that the full set of power spectra, $C_\ell^{\rm TT}$, $C_\ell^{\rm EE}$, $C_\ell^{\rm BB}$, and $C_\ell^{\rm TE}$, are used in the model-fitting.

As the simulated data is generated with the ΛCDM+r model, by fitting the same data with a ΛCDM+PMF model, we aim to find a degenerate ΛCDM+PMF model that fits the

Name	Beam [arcmin]	Noise [μK arcmin]	$\ell_{\rm min}$	$\ell_{\rm max}$	$f_{\rm sky}$
A	17	2	30	1000	0.1
B	1.4	6	30	3000	0.4
C1	17	2	30	1000	0.1
	1.4	6	30	3000	0.4
C2	17	1	30	1000	0.1
	1.4	2	30	3000	0.4
C3	17	0	30	1000	0.1
	1.4	0	30	3000	0.4

Table 2.1: Different sets of experimental settings considered in this chapter. Expt A represents a ground-based small-aperture telescope, while Expt B represents a ground-based large-aperture telescope. C1, C2, and C3 represent a combination of Expt A and B at various noise levels.

data well. Although in theory the expected power spectra from the two competing models are not completely degenerate due to, for instance, the vector-mode signal from the PMF, in practice the difference may not be detectable with non-negligible experimental noises, especially when $B_{\rm 1Mpc} \lesssim 1\,{\rm nG}$. By computing the $\Delta\chi^2$ between the two best-fit models, we evaluate the extent of the degeneracy between the ΛCDM+r model and the ΛCDM+PMF model at various r targets and experiment sensitivities (as specified in Table 2.1).

2.3.1 Fiducial cosmology with $r = 0.01$

We first consider a target of $r = 0.01$ which is one of the primary goals of the upcoming CMB experiments such as the Simons Observatory (SO) [30]. In particular, SO will have two separate instruments for measuring different angular scales of the CMB power spectrum: a large-aperture telescope (LAT) which mainly focuses on small-scale CMB anisotropies, and a small-aperture telescope (SAT) which mainly focuses on the large-scale CMB anisotropies.

As the tensor-mode signal from inflation is expected to show up predominantly in the large angular scales, it is thus the main target of the SO SAT experiment.

Suppose that we live in a universe well described by a ΛCDM+r model with $r = 0.01$, and we measure the CMB power spectrum with an SO SAT-like experiment, specified as Expt A in Table 2.1. As mentioned in the preceding section, we simulate the observed CMB power spectra for Expt A between angular scales of $\ell_{\rm min} = 30$ and $\ell_{\rm max} = 3000$, with a sky fraction of $f_{\rm sky} = 0.3$, to account for the effect of partial sky coverage from a ground-based experiment.

We then fit the simulated data with both the ΛCDM+r and the ΛCDM+PMF models. The resulting CMB power spectra ($C_\ell^{\rm BB}$ in particular) for the two best-fit models are shown in Figure 2.2 in comparison to the simulated data. It shows that the two competing models can be highly degenerate in the angular scales probed by the simulated experiment (Expt A; $30 \lesssim \ell \lesssim 3000$), with a difference much smaller than the variance of the observed data. To be more specific, one can model the variance of the observed data as

$$\sigma^2 \left(C_\ell \right) = \frac{2}{(2\ell + 1) f_{\rm sky}} \left(C_\ell + N_\ell \right)^2 , \tag{58}$$

and compare it to the difference between the two sets of best-fit power spectra, as shown in Figure 2.3, from which one notes that the difference in the best-fit power spectra is ~ 2 orders of magnitudes below the expected variance of the observed power spectrum, indicating that breaking the degeneracy between the two models is impossible with the given experiment without external information. With these observations, it is then unsurprising that we also get a $\Delta\chi^2 \simeq 0.1$ between the two best-fit models. One should also note that as we consider only idealistic experiments here, the degeneracy becomes even stronger with a more realistic experiment.

In fact, the degeneracy between the two models is not too surprising because in the large angular scales ($\ell \lesssim 100$) the passive tensor-mode dominates over the other contributions from the PMF, and the passive tensor-mode is mathematically equivalent to the inflationary tensor-mode signal, so the degeneracy is unavoidable if one observes only at the large angular scales. On the other hand, one does see noticeable difference between the two models at $\ell \lesssim 10$, indicating that the two models are not completely degenerate on all angular scales.

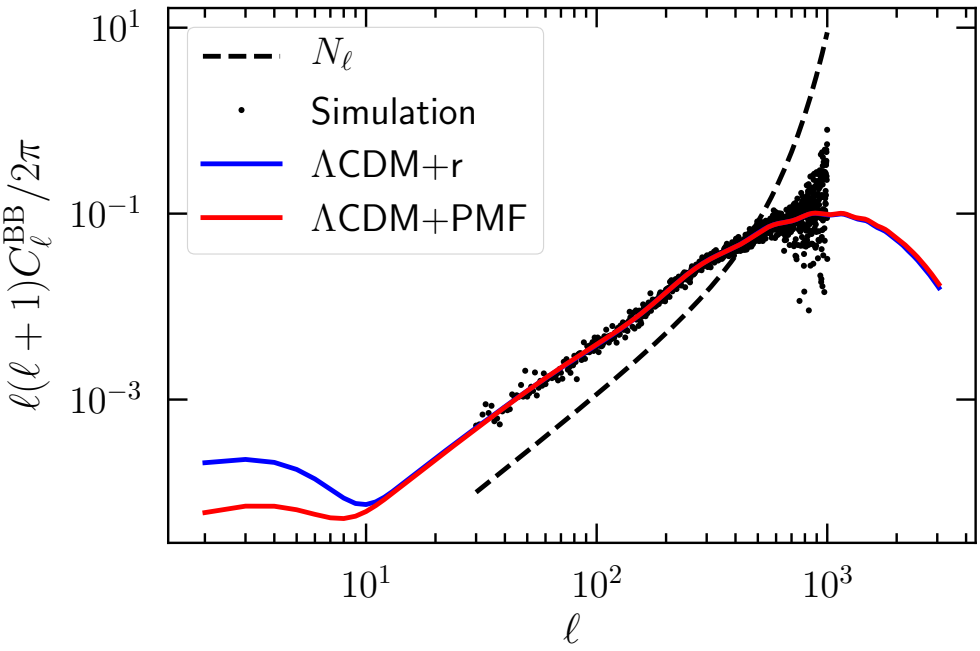

Figure 2.2: $C_\ell^{\rm BB}$ power spectrum showcases the model-fitting and degeneracy between the two models. The blue and red curves are the best-fit power spectrum for the ΛCDM+r and ΛCDM+PMF models, respectively. The black dots represent the simulated data after removing noise model, and the black dashed line represents the noise model for this given simulation which is specified as Expt A in Table 2.1. Plot is in units of μK^2.

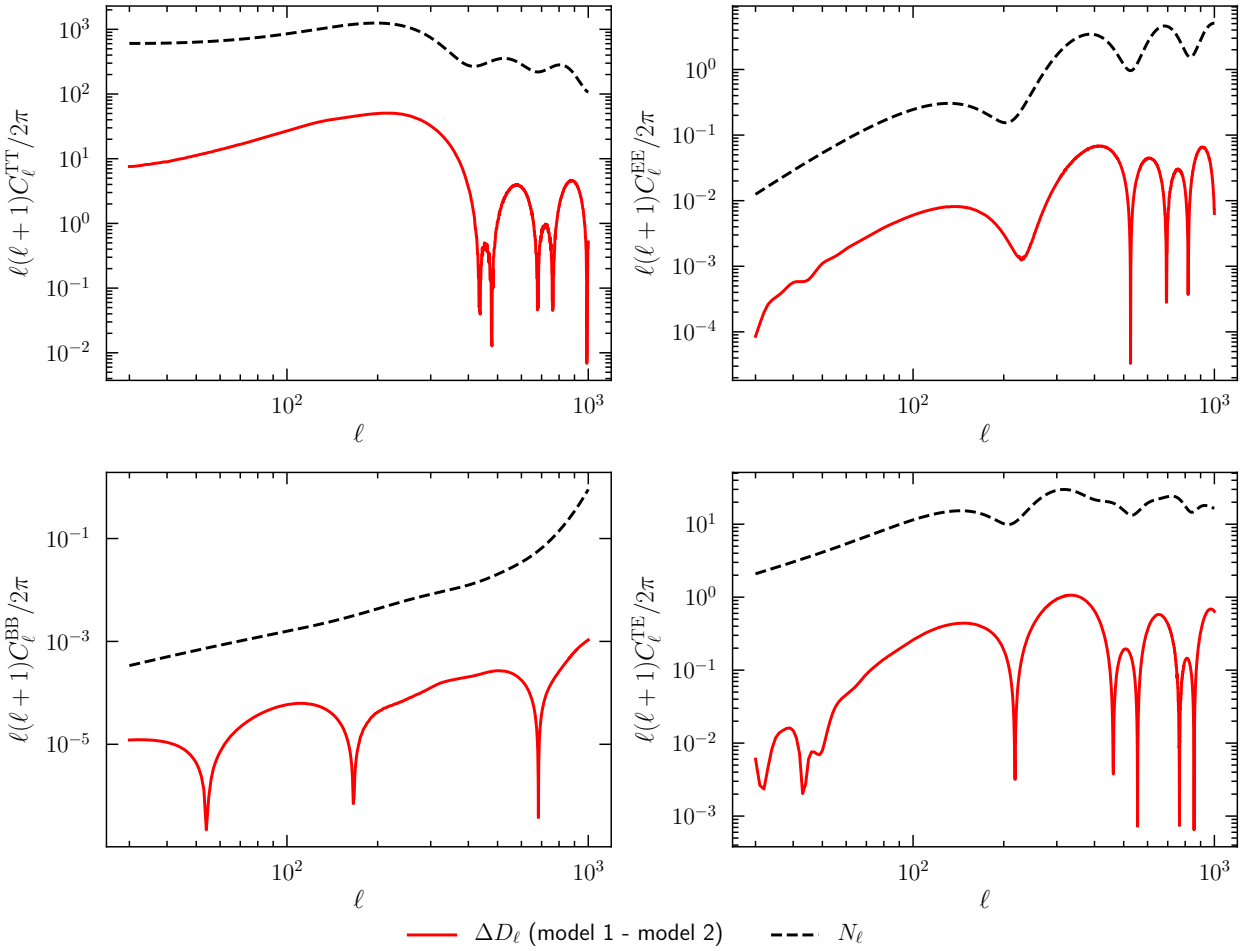

Figure 2.3: Difference of two best-fit CMB power spectra from both models is shown in the red solid line (where model 1 refers to ΛCDM+r and model 2 refers to ΛCDM+PMF) when fitting a cosmology with $r = 0.010$. The black dashed line shows the analytic covariance of the simulated power spectrum. Plots are in units of μK^2.

This is expected because in the small angular scales ($\ell \gtrsim 1000$), the compensated vector mode signal from PMF, which the ΛCDM+r model has no resemblance of, starts to dominate over the other magnetic modes in the $C_\ell^{\rm BB}$ power spectrum. This also implies that the small scale CMB anisotropies likely contain crucial information that helps break the degeneracy between the two models. Nonetheless, measuring such angular scales is likely outside the observational limits of experiments like the SO SAT, so before claiming a 3σ detection when it is detected at such an experiment, one needs to include the constraining power on the small scales from an experiment like the SO LAT to rule out a degenerate ΛCDM+PMF model.

In Figure 2.4 we show the posterior distributions of the magnetic field parameters ($\rm B_{1Mpc}$ and n_B) from the ΛCDM+PMF model. Specifically, we obtain a best-fit PMF model with $\rm B_{1Mpc} = 1.42^{+0.42}_{-0.54}\,nG$ at 68% confidence level, on par with the observational constraints set by Planck in 2015 [67]. We also note that a nearly scale-invariant spectrum, with a spectral index of $n_B < -2.49$, is preferred by the simulated data, which we find a generic feature of the class of degenerate ΛCDM+PMF models to ΛCDM+r. An apparent degeneracy between the amplitude of the magnetic field $\rm B_{1Mpc}$ and the magnetic spectral index n_B can also be seen. This is because as n_B increases, the power spectrum of PMF tilts toward the smaller scales, leading to less power in the large scale modes which Expt A (or an SO SAT-like experiment) is sensitive to, and thus the loss of power gets complemented by a stronger magnetic field, leading to the observed degeneracy. In addition, the inclusion of PMF also induces shifts in the standard cosmological parameters, as shown Figure 2.5. In particular, one notes that the ΛCDM+PMF model favors less dark matter, more baryons, and a higher Hubble constant H_0, the last of which may be of potential interests in the context of the highly debated Hubble tension problem (see, e.g., [73], for a review). This increase in H_0 is likely a side effect of the increased Ω_b and lowered Ω_m due to the presence of magnetic contributions in the metric.

Now suppose that one obtains additional observations from a large-aperture telescope like the SO LAT, specified as Expt B in Table 2.1, which allows us to constrain the small-scale CMB anisotropies precisely. One can then combine its constraining power with Expt A to jointly constrain the PMF on both small and large angular scales. For simplicity, we

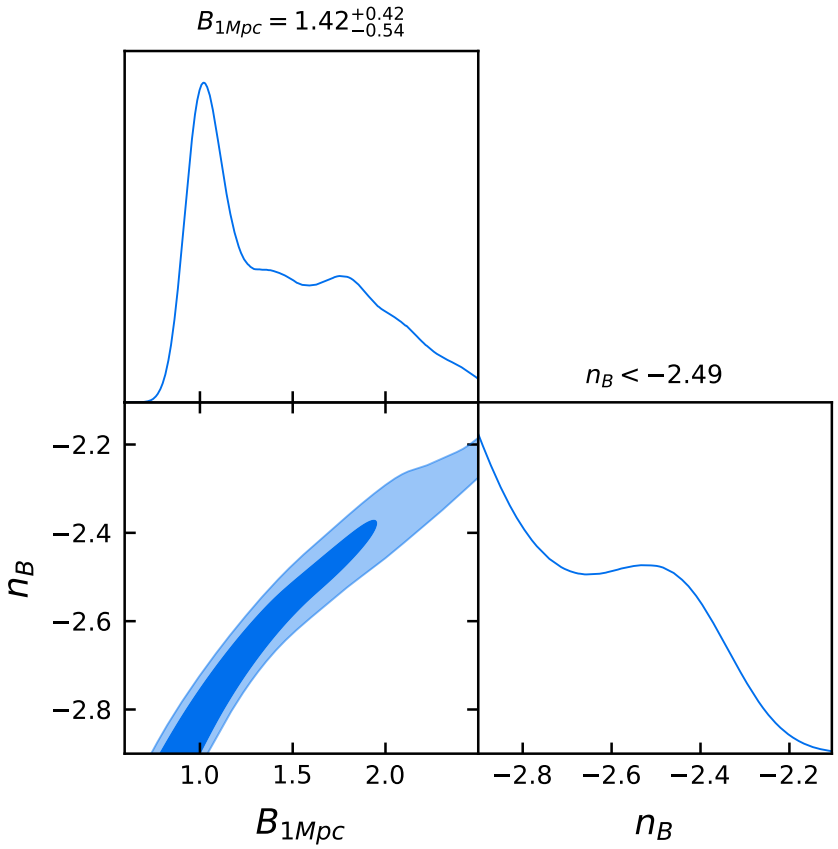

Figure 2.4: Joint posterior distributions for the ΛCDM+PMF model parameters after fitting the simulated data (generated with a ΛCDM+r model with $r = 0.01$) to a ΛCDM+PMF model. B_{1Mpc} is in unit of nG.

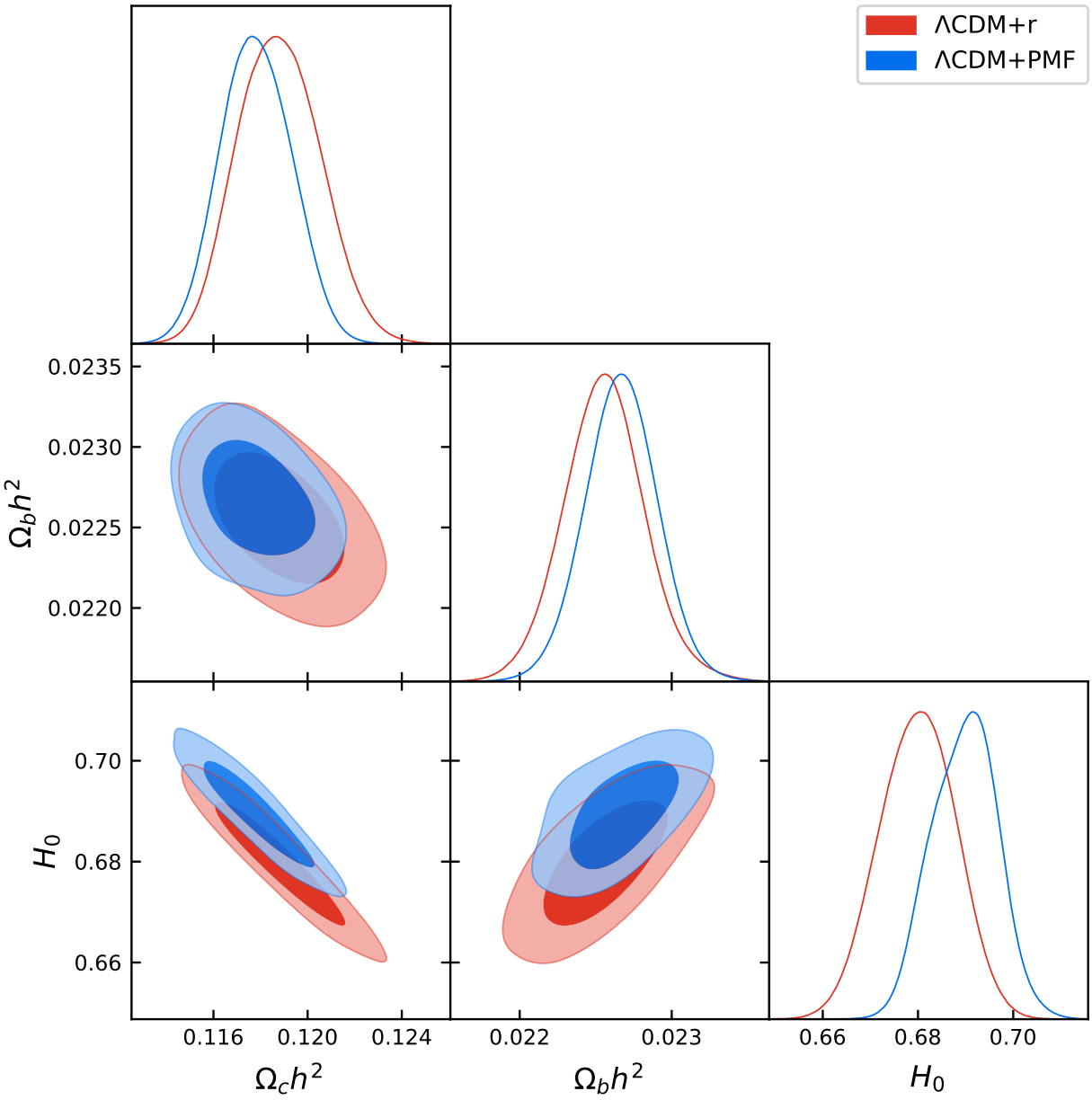

Figure 2.5: Joint posterior distributions of selected cosmological parmaters for the two competing models after fitting both models to the simulated data respectively. The red contours represent the ΛCDM+r model, and the blue contours represent the ΛCDM+PMF model. H_0 is in unit of $100\,\mathrm{km\,s^{-1}\,Mpc^{-1}}$.

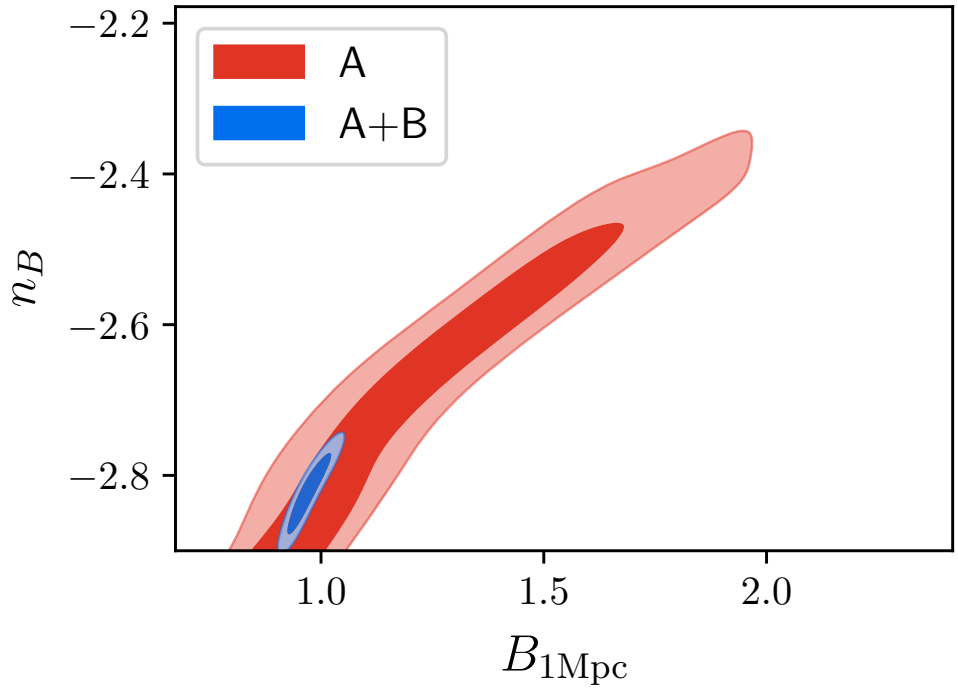

Figure 2.6: Joint posterior distributions of the magnetic field parameters after fitting a ΛCDM+PMF model to the simulated CMB power spectra with a fiducial model of $r = 0.01$. The red contour shows the posterior distribution obtained from Expt A only, while the blue contour shows the posterior distribution as a result of a joint constraint from Expt A and Expt B, as specified in Table 2.1. The levels indicate the 68% and 95% confidence levels, respectively. $\mathrm{B}_{1\mathrm{Mpc}}$ is in unit of nG.

simulate the observed power spectra of the combined constraint by simulating two separate experiments with the same underlying CMB realization and combining them trivially by using the experiment that gives the lowest variance at each ℓ to avoid mode double counting.

In Figure 2.6, we show how the joint posterior distribution of the magnetic field parameters ($B_{1\mathrm{Mpc}}$ and n_B) changes after we include the data from Expt B to the constraint. As discussed in the preceding text that the degeneracy between n_B and $\mathrm{B}_{1\mathrm{Mpc}}$ seen in the blue contour is due to a lack of constraining power in the small scale modes by the Expt A, we see that such degeneracy is broken when the additional observations from Expt B (or an SO LAT-like experiment) are included which tightly constrains the small scale modes of the PMF. The joint constraint leads to a much tighter parameter space for a degenerate ΛCDM+PMF model to live, shown as the red contour, favoring a PMF with $\mathrm{B}_{1\mathrm{Mpc}} \sim 1\,\mathrm{nG}$ and a scale-invariant spectrum. We find a $\Delta\chi^2 \simeq -2.5$ between the best-fit ΛCDM+r model and the ΛCDM+PMF model, showing a stronger preference to the ΛCDM+r model. This improvement in $\Delta\chi^2$ is likely contributed by the stronger constraining power in the small angular scales on the compensated vector-mode signal from PMF which dominates at small angular scales ($\ell \gtrsim 1000$) and has no degenerate signal in ΛCDM+r. This indicates that if a primordial B-mode signal is detected, performing a joint constraint using both the large angular scale and the small angular scale measurements is a promising approach to rule out a degenerate ΛCDM+PMF model.

2.3.2 Lower r targets

In addition to the fiducial model with $r = 0.01$ discussed in the preceding section, we also repeat the study in Section 2.3.1 for different targets of r ranging from 0.001 to 0.010, and compute $\Delta\chi^2$ between the two best-fit models for each set of the simulations of a given r. In particular, we consider three sets of combined observations specified as C1, C2, C3 in Table 2.1. C1 represents the set of observations considered in Section 2.3.1 as a joint constraint of Expt A and B, C2 represents a similar set of experiments with lower noise levels, and C3 represents the same set of experiments in a noise-less limit.

The results of model-fitting show that the degenerate ΛCDM+PMF models generally

favor a nearly scale-invariant spectrum ($n_B \simeq -2.9$) with $B_{1\mathrm{Mpc}} \lesssim 0.8\,\mathrm{nG}$, which is below the current observational limits. Figure 2.7 shows how the amplitude of the magnetic field in the degenerate ΛCDM+PMF model varies with r. This is useful as it gives us a reference to what range of the PMF parameter space is of interests to a particular r target. It shows that, in general, one needs only worry about scale-invariant PMF models with $B_{1\mathrm{Mpc}} \gtrsim 0.5\,\mathrm{nG}$ when targetting $r \gtrsim 0.001$. The results also show that, as the noise level of the experiment improves, more magnetic field parameter space will be strongly constrained, thus reducing the allowed amplitude of the degenerate PMF model.

In Figure 2.8 we show how $\Delta\chi^2$ between the two best-fit models changes as we vary r for each of the three sets of simulated observations. As a reference, we compare the $\Delta\chi^2$ with a 95% confidence level of a χ^2 distribution with one degree of freedom ($\Delta\chi^2 = -3.841$) since the two competing models differ by one degree of freedom. We note that the results feature an apparent trend particularly for Expt C2, and also some fluctuations particularly at $r \lesssim 0.004$. This is likely due to a combination of realization-induced randomness and a poor convergence of some of the MCMC chains. Nevertheless, combined with Figure 2.7, one sees a generic trend in the reduction of $B_{1\mathrm{Mpc}}$ and the increasing of $\Delta\chi^2$ as noise level reduces or as r is lowered, which matches our expectations. Thus our results are likely sensible approximations of the future performances, which are sufficient for our discussion here. In particular, one can see that the performance of Expt C1 in breaking the degeneracy between the two models quickly degrades as $r \lesssim 0.008$. With Expt C2 which has a much lower noise level similar to the targeting performance of the CMB-S4 experiments [74], the situation is much improved as the degeneracy is effectively broken for any $r \gtrsim 0.004$. In the noise-less limit (C3), the degeneracy limit is pushed further down to $r \lesssim 0.002$. This implies that we will be cosmic variance limited to make a distinction between an inflationary tensor-mode signal and a PMF signal below $r \lesssim 0.002$.

Note that our conclusions so far are based entirely on constraining PMF through its effects on the CMB power spectra by means of metric perturbations and Lorentz force. However, this is not the only way one can constrain PMF signals. In fact, PMF also induces a Faraday rotation effect on the polarization of the CMB photons [53], thus providing an additional means to constrain PMF models. Hence, in the subsequent sections we will examine whether

such effect can improve our ability to distinguish the two models.

2.4 Faraday rotation on CMB B-mode

Another probe of PMF is through the effect of Faraday rotation, in which the presence of magnetic field causes a net rotation of the linear polarization directions of the CMB photons along their path, with a rotation angle depending on the frequency of observation and the integrated electron density along the line of sight, given by

$$\alpha = \frac{3}{16\pi^2 e}\lambda_0^2 \int \dot{\tau}(\eta)\tilde{\mathbf{B}}(\mathbf{x}) \cdot d\boldsymbol{l}, \tag{59}$$

where λ_0 is the observed wavelength, $\dot{\tau} \equiv n_e \sigma_T a$ is the differential optical depth which characterizes the electron density along the line of sight, with dominant contribution coming from the photon last scattering surface, and $\tilde{\mathbf{B}} \equiv \mathbf{B}a^2$ is the comoving magnetic field. For a homogeneous magnetic field with a present day amplitude of $\sim 1\,\mathrm{nG}$, the net rotation on the polarization angle is about a degree at 30 GHz, with the size of the effect scaling with frequency as $\alpha \propto v^{-2}$ [58]. In a stochastic background of PMF with a given power spectrum $P_B(k)$, the rotation field $\alpha(\hat{\mathbf{n}})$ is anisotropic with a 2-point correlation function given by [75]

$$\begin{aligned}\langle \alpha(\hat{n})\alpha(\hat{n}')\rangle = \left(\frac{3\lambda_0^2}{16\pi^2 e}\right)^2 \int \frac{d^3k}{(2\pi)^3} P_B(k) \int d\eta \int d\eta' \\ \times \dot{\tau}(\eta)\dot{\tau}(\eta') e^{-i\mathbf{k}\cdot\hat{n}\eta} e^{i\mathbf{k}\cdot\hat{n}'\eta'} [\hat{n}\cdot\hat{n}' - (\hat{k}\cdot\hat{n})(\hat{k}\cdot\hat{n}')],\end{aligned} \tag{60}$$

which can also be written as

$$\langle \alpha(\hat{n})\alpha(\hat{n}')\rangle = \sum_L \frac{2L+1}{4\pi} C_L^{\alpha\alpha} P_L(\hat{n}\cdot\hat{n}'), \tag{61}$$

with $P_L(x)$ the Legendre polynomials and $C_L^{\alpha\alpha}$ the rotational power spectrum. Thus it can be shown that the rotational power spectrum follows

$$C_L^{\alpha\alpha} = \left(\frac{3\lambda_0^2}{16\pi^2 e}\right)^2 \frac{2L(L+1)}{\pi} \int_0^\infty \frac{dk}{k} k^3 P_B(k) T_L^2(k), \tag{62}$$

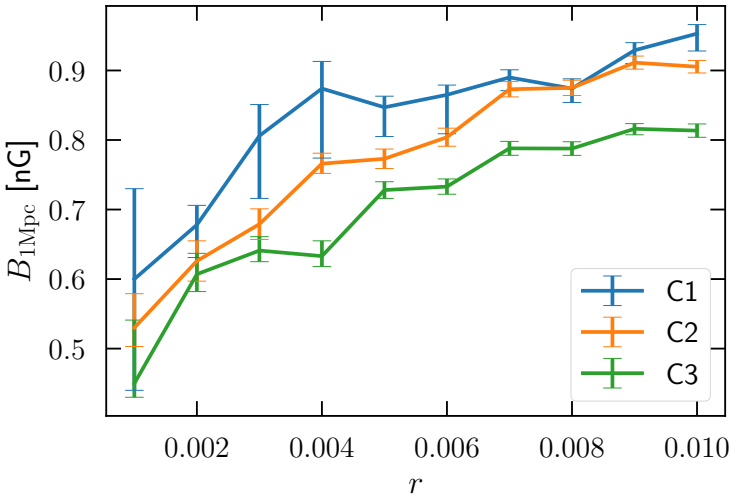

Figure 2.7: The magnitudes of magnetic field ($\mathrm{B}_{1\mathrm{Mpc}}$) that fits the simulated data at different target r for experiment C1, C2, C3 specified in Table 2.1. The error bars indicate the 68% confidence interval for the marginal posterior distribution.

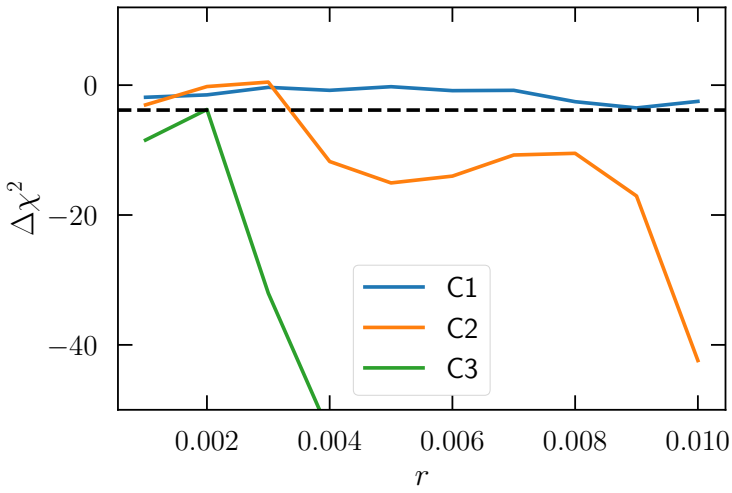

Figure 2.8: How $\Delta\chi^2$ varies with different targets of r. The three lines represent the three simulated set of observations specified in Table 2.1. The black dashed line shows a reference level of $\Delta\chi^2 = -3.841$ which corresponds to the 95% confidence level for a χ^2 distribution with one degree of freedom.

where we have defined a transfer function $T_L(k)$ as

$$T_L(k) \equiv \int_0^{k\Delta\eta} \frac{dx}{x}\, \dot{\tau}(\eta_0 - x/k) j_L(x). \tag{63}$$

Here η_0 is the conformal time today, $j_L(x)$ is the Spherical Bessel function, and $\Delta\eta \equiv \eta_0 - \eta_*$ with η_* corresponding to the conformal time at the maximum visibility. Equation 62 provides the general expression for the rotational power spectrum generated by a PMF model with a given $P_B(k)$.

The rotation field is relevant because the rotation of the polarization direction of CMB photons effectively turns E-mode polarization into B-mode polarization, leading to a B-mode power spectrum $C_\ell^{\rm BB}$ given by [75],

$$C_\ell^{\rm BB} = \frac{1}{\pi} \sum_L (2L+1) C_L^{\alpha\alpha} \sum_{\ell_2} (2\ell_2 + 1) C_{\ell_2}^{\rm EE} \left(H_{\ell\ell_2}^L\right)^2, \tag{64}$$

where $H_{\ell\ell_2}^L$ is defined through the Wigner 3j symbol [76] as

$$H_{\ell\ell_2}^L \equiv \begin{pmatrix} \ell & L & \ell_2 \\ 2 & 0 & -2 \end{pmatrix}. \tag{65}$$

Equation 64 gives the expected signal in $C_\ell^{\rm BB}$ from an anisotropic rotation field $\alpha(\hat{\mathbf{n}})$ with a power spectrum $C_L^{\alpha\alpha}$, giving us an additional means to probe the PMF model through the Faraday rotation effect.

2.4.1 Faraday rotation from a scale-invariant PMF

As discussed in Section 2.3.1, PMF models that generate potentially degenerate B-mode signals to the primordial gravitational wave are approximately scale-invariant. Hence we shall focus exclusively on the this class of PMF models (with $n_B \simeq -2.9$) in this section. In addition, we shall make another simplifying assumption that the magnetic modes with scales smaller than the thickness of the last scattering surface contribute negligibly to the total Faraday rotation, and this means that we only consider magnetic modes for $k \lesssim k_D$ with $k_D \simeq 2\,\mathrm{Mpc}^{-1}$. This assumption is motivated by the fact that the total Faraday rotation is dominated by the large-scale modes, as the rotation generated by magnetic modes with scales smaller than the thickness of the last scattering surface tends to cancel each other due to the Faraday depolarization effect [77].

With the assumptions above, the transfer function $T_L(k)$ defined in Equation 63 can then be approximated as

$$T_L(k) \simeq \frac{j_L(k\eta_0)}{k\eta_0}, \tag{66}$$

where we have used the approximation that $\Delta\eta \approx \eta_0$ and the fact that the differential optical depth $\dot{\tau}$ is sharply peaked relative to the slowly varying magnetic field (as we have ignored the fast varying modes with scales smaller than the thickness of the last scattering surface) and quickly integrates to ~ 1 near the last scattering surface. The rotation power spectrum $C_L^{\alpha\alpha}$ then becomes

$$\begin{aligned} C_L^{\alpha\alpha} &= \frac{9L(L+1)\lambda_0^4}{4(2\pi)^5 e^2 \eta_0^3} \int_0^{k_D} \mathrm{d}k\ P_B(k) j_L^2(x) \\ &= \frac{9L(L+1)B_\lambda^2 \nu_0^{-4}}{(4\pi)^3 \Gamma\left(\frac{n_B+3}{2}\right) e^2} \left(\frac{\lambda}{\eta_0}\right)^{n_B+3} \int_0^{x_D} dx\ x^{n_B} j_L^2(x), \end{aligned} \tag{67}$$

where $x_D \equiv k_D\eta_0$, ν_0 is the observing frequency, $\lambda = 1\,\mathrm{Mpc}$ is the size of the smoothing kernel. This result is consistent with that given in Ref. [78]. Specifically, we follow the same approximation as in Ref. [78] that replaces $j_L^2(x)$ with $1/2x^2$ after the second zero of $j_L(x)$ in Equation 67 to simplify the numerical integration of the fast oscillating functions. In Figure 2.9 we show the rotation power spectrum of a PMF with $\mathrm{B}_{1\mathrm{Mpc}} = 1\,\mathrm{nG}$ for different n_B, as calculated from Equation 67. The results show that as the spectral index approaches $n_B \simeq$

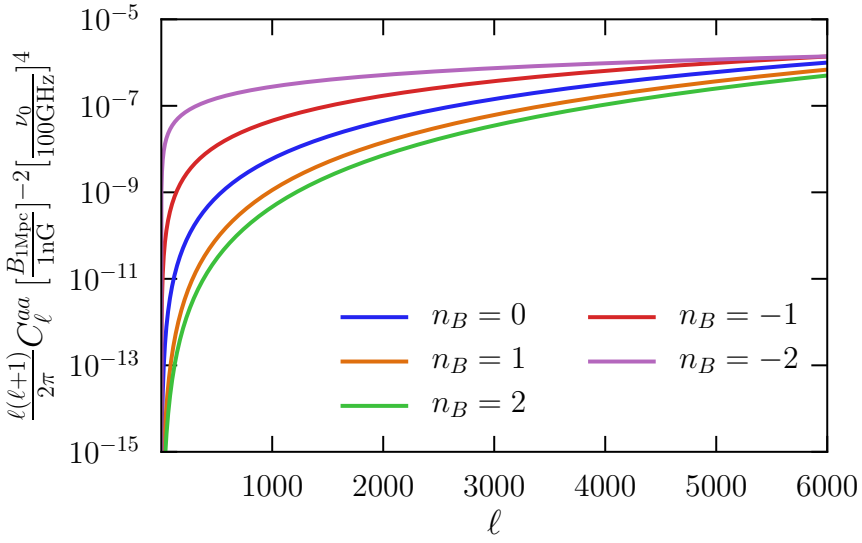

Figure 2.9: Rotation power spectrum for different magnetic spectral indices n_B calculated using Equation 67 with the Planck 2018 best-fit cosmology [1], $\nu_0 = 100\,\mathrm{GHz}$, and $\mathrm{B}_{1\mathrm{Mpc}} = 1\,\mathrm{nG}$. The amplitude of the power spectrum scales with $\mathrm{B}_{1\mathrm{Mpc}}^2$ and ν_0^{-4}.

-3, the rotation spectrum approaches a scale-invariant limit as expected. We should also note that the above derivations assume the CMB polarization is generated instantaneously in the beginning of recombination, which is not true. A proper calculation needs to consider the fact that Faraday rotation occurs alongside with the generation of CMB polarization. Nonetheless, such effect has been calculated by Ref. [75] and shown to result in a small enough difference for our order of magnitude estimate here. Thus we shall ignore such effect for the subsequent discussion.

With the rotational power spectrum $C_\ell^{\alpha\alpha}$, one can then estimate the expected C_ℓ^{BB} power spectrum sourced by the rotation field using Equation 64. In Figure 2.10, we show the expected B-mode power spectrum sourced by a nearly scale-invariant PMF with $n_B = -2.9$ and $\mathrm{B}_{1\mathrm{Mpc}} = 1\,\mathrm{nG}$, observed at $100\,\mathrm{GHz}$. The result shows two noticeable features: (1). Faraday rotation signal in C_ℓ^{BB} peaks in the small angular scales (at $\ell \sim 1000$), similar to the CMB lensing signal, with a significantly lower amplitude likely being two orders of

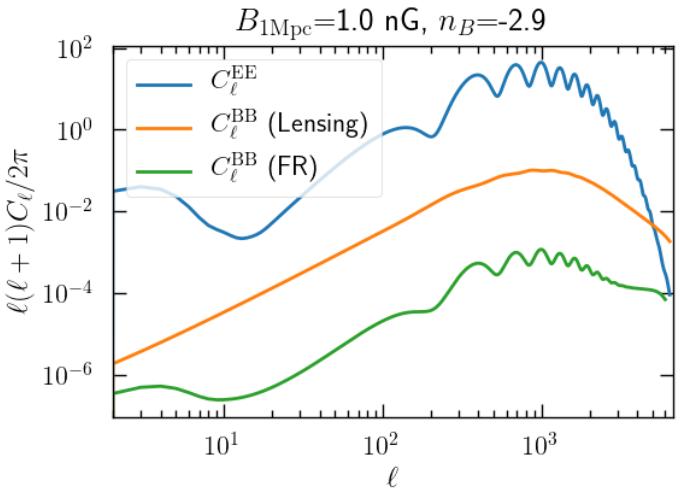

Figure 2.10: The green curve shows the B-mode signal generated by the Faraday rotation of a PMF with $n_B = -2.9$ and $\mathrm{B}_{1\mathrm{Mpc}} = 1\,\mathrm{nG}$ at $\nu_0 = 100\,\mathrm{GHz}$. The orange curve shows the expected lensing signal and the blue curve shows the C_ℓ^{EE} signal. Note that "FR" denotes Faraday rotation. Plot is in unit of $\mu\mathrm{K}^2$.

magnitude lower compared to that of CMB lensing. (2). Unlike the CMB lensing signal, the B-mode signal from the rotation field features acoustic oscillations similar to those in CMB E-mode power spectrum. This is expected as, according to Equation 64, the B-mode signal from the rotation field is effectively a convolution of the E-mode power spectrum C_ℓ^{EE} with the rotation power spectrum $C_\ell^{\alpha\alpha}$ in ℓ-space. Since $C_\ell^{\alpha\alpha}$ is scale invariant, the ℓ dependence in the resulting C_ℓ^{BB} is determined by that of C_ℓ^{EE}, thus featuring the acoustic oscillations. This is a unique feature that allows one to distinguish the rotation signal from the lensing signal in the C_ℓ^{BB}.

To project the performance of future CMB experiments in constraining the PMF by measuring the Faraday rotation signal, we define the signal-to-noise (SNR) ratio as

$$\left(\frac{S}{N}\right)^2 = \sum_\ell \frac{(2\ell+1) f_{\mathrm{sky}} \left(C_\ell^{\mathrm{BB,FR}}\right)^2}{2\left(C_\ell^{\mathrm{BB,tot}} + N_\ell^{\mathrm{BB}}\right)^2}, \tag{68}$$

with $C_\ell^{\rm BB,FR}$ the expected B-mode signal from the Faraday rotation, and $C_\ell^{\rm BB,tot}$ the total B-mode signal that includes the contributions both the Faraday rotation signal and the CMB lensing signal. $N_\ell^{\rm BB}$ refers to the expected B-mode noise power spectrum from a given experiment as approximated by Equation 54. The factor $f_{\rm sky}$ is added to approximate the effect of the partial sky coverage of a realistic experiment, in the form of a reduction in the number of available measurements and thus a reduction in the total SNR. In addition, we assume an observing frequency of 100 GHz for the subsequent discussion, which is where we expect the highest SNR to come from, due to the ν^{-4} dependence of $C_L^{\alpha\alpha}$.

As the Faraday rotation signal is significant mainly on the small angular scales, the experiments relevant to detecting such signal are the large-aperture experiments, which are more sensitive to these scales. Specifically, we consider the Expt B as specified in Table 2.1 with different noise levels: $6\,\mu$K arcmin, $2\,\mu$K arcmin, and $0\,\mu$K arcmin, and compute the SNR for each experiment for a scale invariant PMF with the amplitude $\rm B_{1Mpc}$ varying from 0.1 nG to 1 nG. The resulting SNRs are presented in Figure 2.11, which shows that, for an SO LAT-like experiment with a noise level of $6\,\mu$K arcmin, the Faraday rotation signal is not detectable in the power spectrum, hence contributing negligible constraining power on the PMF. In comparison, a CMB S4-like experiment with a noise level of $2\,\mu$K arcmin barely detects a PMF with $\rm B_{1Mpc} \gtrsim 0.9\,nG$ at $\rm SNR \gtrsim 1$, while at the noise-less limit, one can detect a PMF with $\rm B_{1Mpc} \gtrsim 0.5\,nG$ with $\rm SNR \gtrsim 1$, and $\rm B_{1Mpc} \gtrsim 0.8\,nG$ with $\rm SNR \gtrsim 3$. As concluded from Figure 2.7, degenerate PMF models of interests to the upcoming experiments generally have amplitudes $\rm B_{1Mpc}$ ranging from $\sim 0.5 - 1\,$nG, comparable to the detection limit of the noise-less case. This suggests that Faraday rotation signal in the B-mode power spectrum is unlikely a strong constraint on the PMF.

On the other hand, it is worth noting that the above SNR estimates neglect the effect of delensing, which is a proposed algorithm to remove the CMB lensing signal from the B-mode power spectrum (see, e.g., [79]). As the CMB lensing signal is generally orders of magnitude higher than the Faraday rotation signal in $C_\ell^{\rm BB}$, being able to remove a significant portion of the lensing signal significantly reduces the total variance in the B-mode power spectrum, thus improving the SNR. To be more specific, we can denote the $C_\ell^{\rm BB,tot}$ in Equation 68 as

$$C_l^{\rm BB,tot} = C_l^{\rm BB,CMB} + C_l^{\rm BB,FR} + A_{\rm delens} C_\ell^{\rm BB,lensing}, \tag{69}$$

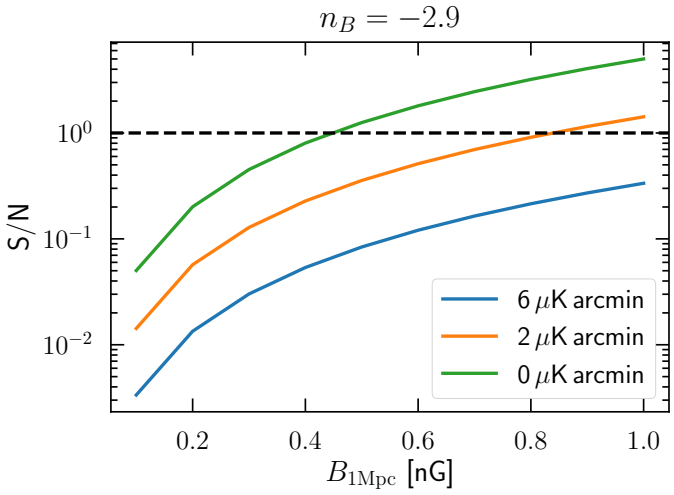

Figure 2.11: Signal-to-noise ratio for various $\mathrm{B}_{1\mathrm{Mpc}}$. The three different solid curves show the S/N curve for three experiments with various noise levels. The dashed curve indicates the threshold of $S/N = 1$.

where $C_l^{\mathrm{BB,CMB}}$, $C_\ell^{\mathrm{BB,FR}}$, and $C_\ell^{\mathrm{BB,lensing}}$ denote the B-mode signal from the CMB, PMF, and lensing, respectively, and A_{delens} denotes the residual fraction of delensing which characterizes the delensing efficiency. Optimistic estimates suggest that an SO-like experiment can achieve $A_{\mathrm{delens}} \sim 0.5$ with inputs from external datasets [30], and a CMB S4-like experiment with a noise level of $\sim 2\mu\mathrm{K}\,\mathrm{arcmin}$ can achieve $A_{\mathrm{delens}} \sim 0.4$ [74]. If the B-mode power spectrum is signal dominated, delensing can improve the signal-to-noise ratio by a factor of A_{delens}^{-1}, thus lowering the PMF detection limit by a factor of $A_{\mathrm{delens}}^{-1/2}$.

2.5 Rotational field reconstruction from PMF

The effect of Faraday rotation is also apparent in the CMB polarization maps, which acts as an effective rotation field $\alpha(\hat{\mathbf{n}})$ that rotates the CMB polarization maps with

$$ {}_{\pm2}A(\hat{\mathbf{n}}) \equiv (Q \pm iU)(\hat{\mathbf{n}}) = e^{\pm 2i\alpha(\hat{\mathbf{n}})}(\tilde{Q} \pm i\tilde{U})(\hat{\mathbf{n}}), \tag{70} $$

where Q and U refer to the Stoke parameters for the rotated CMB photons, and we use tilde to denote the unrotated CMB maps for which no rotation has occurred. In the limit that $\alpha(\hat{\mathbf{n}}) \ll 1$, $\delta_{\pm 2}A(\hat{\mathbf{n}}) \simeq 2i\alpha(\hat{\mathbf{n}})_{\pm 2}\tilde{A}(\hat{\mathbf{n}})$. The corresponding multiple moments are

$$\begin{aligned}\delta_{\pm 2}A_{lm} \simeq &\pm 2i \sum_{\mathrm{LM}} \sum_{l_2 m_2} \alpha_{LM\pm 2}A_{l_2 m_2} \\ &\times \int d\hat{\mathbf{n}}\ {}_{\pm 2}Y^*_{lm}(\hat{\mathbf{n}})Y_{LM}(\hat{\mathbf{n}})_{\pm 2}Y_{l_2 m_2}(\hat{\mathbf{n}}),\end{aligned} \tag{71}$$

where the notation ${}_sY_{lm}$ denotes the spin-weighted spherical harmonics [80]. The integral can be performed with the formula

$$\begin{aligned}\int d\hat{\mathbf{n}}_{s_1}Y_{l_1 m_1}(\hat{\mathbf{n}})_{s_2}Y_{l_2 m_2}(\hat{\mathbf{n}})_{s_3}Y_{l_3 m_3}(\hat{\mathbf{n}}) = &\left[\frac{\prod_{i=1}^{3}2l_i+1}{4\pi}\right]^{1/2} \\ \times \begin{pmatrix} j_1 & j_2 & j_3 \\ m_1 & m_2 & m_3 \end{pmatrix} &\begin{pmatrix} j_1 & j_2 & j_3 \\ -s_1 & -s_2 & -s_3 \end{pmatrix},\end{aligned} \tag{72}$$

and gives

$$\delta_{\pm 2}A_{lm} \simeq \pm 2i \sum_{\mathrm{LM}} \sum_{l_2 m_2} \alpha_{LM\pm 2}A_{l_2 m_2}\xi^{LM}_{lml_2 m_2 \pm}H^L_{ll_2}, \tag{73}$$

with

$$\xi^{LM}_{lml_2 m_2} \equiv (-1)^m \sqrt{\frac{(2L+1)(2l_2+1)(2l+1)}{4\pi}} \begin{pmatrix} l & L & l_2 \\ -m & M & m_2 \end{pmatrix}, \tag{74}$$

and

$${}_{\pm}H^L_{ll_2} \equiv \begin{pmatrix} l & L & l_2 \\ \pm 2 & 0 & \mp 2 \end{pmatrix} = (-1)^{l+L+l_2}{}_{\mp}H^L_{ll_2}. \tag{75}$$

The polarization field ${}_{\pm 2}A_{lm}$ can be decomposed into the curl-free (E-mode) and the gradient-free (B-mode) components with

$$\begin{aligned}E_{lm} &= \frac{1}{2}\left({}_{+2}A_{lm} + {}_{-2}A_{lm}\right), \\ B_{lm} &= \frac{1}{2i}\left({}_{+2}A_{lm} - {}_{-2}A_{lm}\right).\end{aligned} \tag{76}$$

This gives

$$\delta E_{lm} = -2i \sum_{LM} \sum_{l_2 m_2} \alpha_{LM}\xi^{LM}_{lml_2 m_2}H^L_{ll_2}\left(\beta_{lLl_2}\tilde{E}_{l_2 m_2} + \epsilon_{lLl_2}\tilde{B}_{l_2 m_2}\right), \tag{77}$$

and

$$\delta B_{lm} = 2\sum_{LM}\sum_{l_2m_2}\alpha_{LM}\xi^{LM}_{lml_2m_2}H^L_{ll_2}\left(\epsilon_{lLl_2}\tilde{E}_{l_2m_2} - \beta_{lLl_2}\tilde{B}_{l_2m_2}\right), \tag{78}$$

where we have defined $H^L_{ll_2} \equiv {}_+H^L_{ll_2}$ and

$$\begin{aligned}\epsilon_{lLl_2} &\equiv \frac{1+(-1)^{l+L+l_2}}{2},\\ \beta_{lLl_2} &\equiv \frac{1-(-1)^{l+L+l_2}}{2}.\end{aligned} \tag{79}$$

Equation 77 and Equation 78 describe the effect of Faraday rotation on the CMB E-mode and B-mode polarization maps respectively which effectively mixes the two maps through rotation. This introduces couplings between the E-mode and B-mode maps at different l which otherwise do not exist, given by

$$\langle E_{lm}B^*_{l'm'}\rangle_{\rm CMB} = \sum_{LM}\alpha_{LM}\xi^{LM}_{lml'm'}f^{\rm EB}_{lLl'}, \tag{80}$$

with

$$f^{\rm EB}_{lLl'} = 2\epsilon_{lLl'}[H^L_{l'l}\tilde{C}^{\rm EE}_l - H^L_{ll'}\tilde{C}^{\rm BB}_l]. \tag{81}$$

The $\langle ...\rangle_{\rm CMB}$ denotes that the average is to be taken over CMB realisations only. The coupling also allows one to reconstruct the rotation field a_{LM} with a quadratic estimator approach similar to the reconstruction of CMB lensing [81]. One can similarly define an unbiased quadratic estimator for rotation field as

$$\hat{\alpha}_{LM} = A^{\rm EB}_L\sum_{ll'}\sum_{mm'}\xi^{LM}_{lml'm'}g^{\rm EB}_{ll'}E_{lm}B^*_{l'm'}, \tag{82}$$

with the normalization factor to ensure the estimator is unbiased, given by

$$\left(A^{\rm EB}_L\right)^{-1} = \sum_{ll'}\frac{(2l+1)(2l'+1)}{4\pi}g^{\rm EB}_{ll'}f^{\rm EB}_{lLl'}, \tag{83}$$

in doing so we have used

$$\sum_{mm'}\xi^{LM}_{lml'm'}\xi^{L'M'}_{lml'm'} = \frac{(2l+1)(2l'+1)}{4\pi}\delta_{LL'}\delta_{MM'}. \tag{84}$$

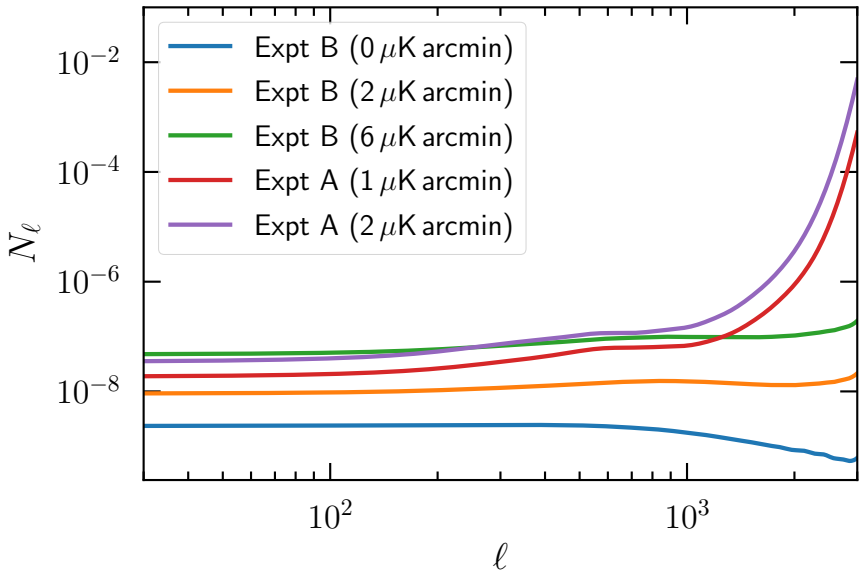

Figure 2.12: Gaussian noise covariance $N_L^{\rm EB}$ for experiments specified in Table 2.1 with varying noise levels.

The weights $g_{ll'}^{\rm EB}$ can be chosen to minimize the total variance of the estimator $\langle \alpha_{LM}^* \alpha_{LM} \rangle$ with

$$g_{ll'}^{\rm EB} = \frac{f_{lLl'}^{\rm EB}}{C_l^{\rm EE} C_{l'}^{\rm BB}}, \tag{85}$$

and the resulting variance of the reconstructed rotation field α_{LM}, denoted as $N_L^{\rm EB}$, is related to the normalization factor by

$$N_L^{\rm EB} = \left(A_L^{\rm EB}\right)^{-1} = \sum_{ll'} \frac{(2l+1)(2l'+1)}{4\pi} \frac{(f_{lLl'}^{\rm EB})^2}{C_l^{\rm EE} C_{l'}^{\rm BB}}, \tag{86}$$

with $C_l^{\rm EE}$ and $C_{l'}^{\rm BB}$ the observed E- and B-mode power spectrum, respectively. Here $N_L^{\rm EB}$ is a dimensionless quantity that characterizes the variance of the reconstructed rotation angle at each L.

In Figure 2.12, we show the expected reconstruction noise N_L^{EB} calculated using Equation 86 for experiments considered previously in Table 2.1, and for a nearly scale invariant PMF with varying amplitudes of $\rm B_{1Mpc}$ and $n_B = -2.9$. In particular, we consider Expt A

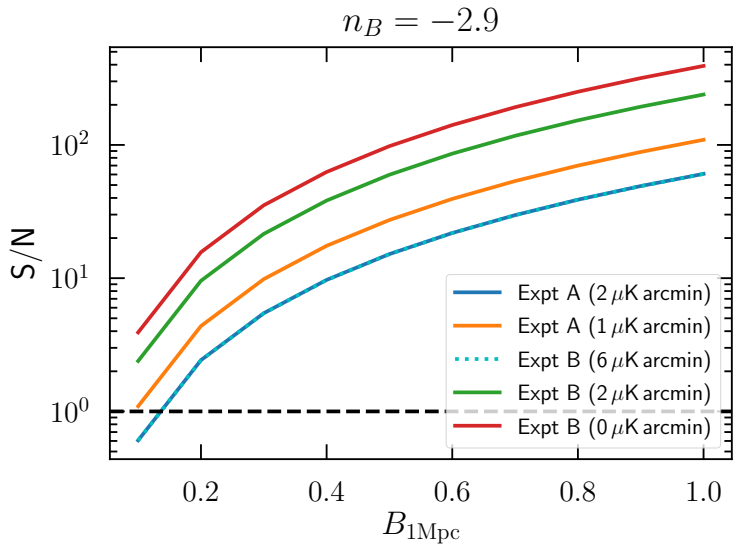

Figure 2.13: Signal-to-noise ratio expected for the quadratic estimator in a variety of experimental settings. The black dashed line represents S/N=1.

with noise levels of 2 μK arcmin and 1 μK arcmin, and Expt B with noise levels of 6 μK arcmin, 2 μK arcmin, and 0 μK arcmin. The results show that the large-aperture experiments have orders of magnitude lower reconstruction noise at $\ell \gtrsim 1000$, confirming our expectation that the small-scale CMB anisotropies have stronger constraining power on the Faraday rotation signal.

To forecast the expected performance of the quadratic estimator for future CMB experiments, we define the SNR as

$$(S/N)^2 = \sum_{L=L_{\mathrm{min}}}^{L_{\mathrm{max}}} f_{\mathrm{sky}} \frac{2L+1}{2} \left(\frac{C_L^{\alpha\alpha}}{N_L^{EB}} \right)^2 , \tag{87}$$

where, similar to Section 2.4, we use f_{sky} to approximate the partial sky coverage. We also assume the observations are made at 100 GHz, which is the frequency channel expected to contribute the highest SNR.

In Figure 2.13 we show the expected SNR for the same set of experiments considered previously. It shows that reconstructing a rotation field using the quadratic estimator approach

results in an order of magnitude improvement in the SNR as compared to constraining its effects on the CMB B-mode power spectrum. This is unsurprising as the effect of a rotation field α on $C_\ell^{\rm BB}$ scales with $\sim \alpha^2$, which is a second order effect, whereas its effect on the cross-correlation $\langle EB \rangle$ scales with $\sim \alpha$ (see Equation 80), which is a first order effect, thus giving a significantly improved SNR. The results also show that large-aperture experiments (Expt B) have better SNR in general as a result of the significantly lower reconstruction noise (as shown in Figure 2.12). Specifically, a SO SAT-like experiment with a noise level of $2\,\mu$K arcmin gives comparable SNR to an SO LAT-like experiment with a noise level of $6\,\mu$K arcmin, both of which are capable of constrain PMF models down to $\mathrm{B_{1Mpc}} \gtrsim 0.3\,\mathrm{nG}$ with $S/N \gtrsim 3$, and this limit may be pushed further down with the CMB S4-like noise levels to $\mathrm{B_{1Mpc}} \gtrsim 0.1\,\mathrm{nG}$. This indicates that the degenerate PMF models to the ranges of r of interests to the upcoming CMB experiments will likely be strongly constrained by the small-scale anisotropies. Note that similar to 2.4 we have neglected the effect of delensing which may further improve the PMF constraint.

2.6 Discussion

We have investigated the question – whether the PMF signal in the CMB may be a source of confusion for the inflationary B-mode signal from primordial gravitational waves? The possibility of such degeneracy has raised concerns (see, e.g., [46, 47]), particularly on whether one can prove with confidence that a tensor-mode signal detected in the CMB B-mode power spectrum comes from inflation instead of some other sources such as the PMF. We found that the answer may be "yes" if one utilizes only the information in the large-scale CMB anisotropies ($\ell \lesssim 1000$), as PMF also sources large-scale B-mode signal by sourcing tensor-mode metric perturbations in a mathematically equivalent form to that of the primordial gravitational waves, thus generating a completely degenerate signal on the large angular scales. However, after including the constraining power on the small-scale CMB anisotropies ($\ell \gtrsim 1000$), the answer clearly becomes "no", thanks to the high sensitivity measurements on the small angular scales by the upcoming CMB experiments which significantly constrain the

unique signatures of the PMF model including its vector-mode perturbation and the effects of Faraday rotation on the CMB. Our findings confirm previous claims in, e.g., Refs. [82, 45], and are in a broad agreement with the findings in Refs. [47, 46], that the PMF model does not pose a challenge to the future B-mode searches.

Our analysis extended the previous works in considering a much wider ranges of targeting tensor-to-scalar ratios, magnetic field models, and experimental settings, and in establishing the empirical relation between r and the magnetic field amplitude of the degenerate PMF model through simulations and MCMC-based model-fittings. In particular, we established that the degenerate PMF models for $r \gtrsim 0.001$ generally have $\mathrm{B_{1Mpc}} \gtrsim 0.5\,\mathrm{nG}$. We also considered the Faraday rotation effect of the PMF in both the B-mode power spectrum and the EB off-diagonal cross correlations, and showed that the PMF models with $\mathrm{B_{1Mpc}} \gtrsim 0.5\,\mathrm{nG}$ can be ruled out with high confidence, particularly with the off-diagonal EB cross correlation, by the upcoming CMB experiments. Our work can also be regarded as a demonstration of a methodology that can be used in systematically ruling out a possible source of confusion to the tensor-mode signal in the context of the upcoming searches.

3.0 Constraining Cosmic Birefringence with Atacama Cosmology Telescope

Having seen the possibility of detecting rotations in the CMB polarization fields through the use of EB cross correlation in Chapter 2, one could apply this method to experimental data to constrain exotic physical scenarios that may induce polarization rotations. Such effect is broadly known as cosmic birefringence, which refers to the phenomenon where photons with different linear polarizations propagate differently. It could be caused by the PMF as we discussed in Chapter 2 or by physics beyond the standard model, thus providing a promising avenue to search for new physics signal. In this chapter I describe a work in which we perform a search for cosmic birefringence signal in the data collected by the Atacama Cosmology Telescope (ACT). The manuscript that this chapter is based on was published in April 2020 in the Physics Review D journal [83] produced by a collaborative work of Toshiya Namikawa, Omar Darwish, Blake D. Sherwin, and myself, as an ACT collaboration paper.

3.1 Introduction

The Atacama Cosmology Telescope (ACT) experiment, a ground-based CMB experiment located in the Atacama Desert in Chile, is a 6-m diameter telescope scanning in millimeter sky in both temperature and polarization [84]. The precision measurements of the CMB polarization by ACT makes it possible to search for signs of new physics by searching for a rotation of linear polarization in the CMB photons, a phenomenon known as cosmic birefringence which is absent in the Standard Model. Cosmic birefringence can be sourced by several types of beyond-Standard-Model physics. For example, axion-like particles within a mass range of $10^{-33} \lesssim m_a \lesssim 10^{-28}$eV can couple to photons through a so-called Chern-Simons interaction and source cosmic birefringence (see, e.g., [85, 86, 87, 88, 89] and a review, [90]). In addition, birefringence-inducing pseudo-scaler fields are also a viable solution to the Hubble's tension [91]. Cosmic birefringence can also be generated by primordial magnetic fields

(PMFs) via Faraday rotation effect on the CMB polarization, as we discussed in Chapter 2, though PMF-induced cosmic birefringence has a frequency dependence that distinguishes itself from the other generating mechanisms.

Cosmic birefringence can be both isotropic and anisotropic. In particular, anisotropic birefringence can be a result of the spatial variation of the inducing sources. Such models are well motivated theoretically (see, e.g., [85, 92, 93, 94, 95, 96]). Thus, being able to measure and place constraints on an anisotropic polarization rotation in CMB provides valuable insights to fundamental physics.

Observationally, isotropic cosmic birefringence causes a transfer of CMB E mode power into B mode, leading to non-zero odd-parity EB cross spectra – an effect we discussed in Section 2.5 – which is absent from standard cosmological model. Hence, such effect allows one to constrain isotropic cosmic birefringence by measuring the EB power spectra. One caveat of such approach is that a mis-calibration in the global polarization angle in the instrument can lead to a spurious isotropic cosmic birefringence signal. In fact, EB power spectra has often been used to calibrate the global polarization angle. Galactic foreground components, on the other hand, may also lead to odd-parity spectra and may help break the degeneracy between global polarization angle calibration and an isotropic cosmic birefringence signal.

When the cosmic birefringence is anisotropic, it induces direction-dependent EB correlation, as a result of statistical anisotropy. In this case, cosmic birefringence acts effectively as an anisotropic rotation field $\alpha(\hat{\mathbf{n}})$, mixing Stokes parameter $Q(\hat{\mathbf{n}})$ and $U(\hat{\mathbf{n}})$ in every direction. In Fourier space, the rotation field effectively mixes E and B modes of different angular scales, leading to non-zero off-diagonal ($\ell \neq \ell'$) elements in the CMB covariance. Such off-diagonal covariance, therefore, allows us to reconstruct the underlying rotation field $\alpha(\hat{\mathbf{n}})$ in a way similar to the CMB lensing reconstruction [81]. Although birefringence also induces other cross correlation, such as between temperature and E mode maps, reconstruction using EB has been shown to give the highest signal-to-noise ratio, and therefore we focus on birefringence reconstruction using EB correlations in this work.

Previous works have placed constraints on anisotropic cosmic birefringence, making use of temperature and polarization data from WMAP [97], POLARBEAR [4], BICEP2/Keck Array [5], and Planck [6]. It is evident that reconstructing birefrigence power spectrum

from off-diagonal CMB covariance has become the most powerful probe to measure the anisotropies of the cosmic birefringence and has indeed lead to the current best constraints [5, 6].

Data obtained from the Atacama Cosmology Telescope Polarimeter (ACTPol) provides CMB polarization measurements with high angular resolution and increasingly better sensitivity. It is thus expected that ACT data gives better constraint on anisotropic cosmic birefringence signal. Therefore, we focus on the reconstruction of anisotropic cosmic birefringence using CMB polarization data from ACTPol in this work. Specifically, we focus on frequency-independent signal which excludes the possibility of a PMF-induced birefringence. We leave a reconstruction of frequency-dependent birefringence signal to future work.

This chapter will be structured as the following. In Section 3.2, we review the basics of cosmic birefrigence, including its effects on CMB. In Section 3.3, we describe the data and simulations used in the study. In Section 3.4, we describe the algorithm used to estimate the rotation field. In Section 3.5 we study the potential systematics that may affect the measurements. In Section 3.6 we present the results, i.e., the reconstructed rotation spectrum. We discuss the implications of our results and conclude in Section 3.7.

3.2 Effects of cosmic birefringence in CMB

Cosmic birefrigence acts effectively as a rotation field $\alpha(\hat{\mathbf{n}})$ that rotates the linear polarization of CMB photons. The effect of rotation field $\alpha(\hat{\mathbf{n}})$ on the CMB polarization has been discussed in details in Section 2.5, so we only briefly review the relevant results here. Assuming $\alpha(\hat{\mathbf{n}})$ follows a Gaussian random statistics, its two-point correlation function is given by

$$\langle \alpha(\hat{\mathbf{n}})\alpha(\hat{\mathbf{n}}')\rangle = \sum_L \frac{2L+1}{4\pi} C_L^{\alpha\alpha} P_L(\hat{\mathbf{n}}\cdot\hat{\mathbf{n}}'), \tag{88}$$

with $C_L^{\alpha\alpha}$ the power spectrum of the rotation field that completely specifies the statistical property of $\alpha(\hat{\mathbf{n}})$ and $P_L(\cos\theta)$ the Legendre polynomials. For a scale-invariant rotation

field, we parametrize its power spectrum as

$$\frac{L(L+1)}{2\pi}C_L = A_{\rm CB} \times 10^{-4}, \tag{89}$$

with $A_{\rm CB}$ the amplitude of the cosmic birefringence signal. The effect of a rotation field $\alpha(\hat{\mathbf{n}})$ on the Stokes parameters Q and U is given by

$$Q \pm iU = e^{2i\alpha(\hat{\mathbf{n}})}(\tilde{Q} \pm i\tilde{U}), \tag{90}$$

where quantities with tildes denote unrotated CMB polarization fields. As discussed in Section 2.5, in the weak-field limit, i.e., $\alpha(\hat{\mathbf{n}}) \ll 1$, the rotation field induces off-diagonal correlation between the E-mode and B-mode polarization fields, given by

$$\langle E_{lm} B^*_{l'm'} \rangle = \sum_{LM} \alpha_{LM} \xi^{LM}_{lml'm'} f^{\rm EB}_{lLl'}, \tag{91}$$

where

$$f^{\rm EB}_{lLl'} = 2\epsilon_{lLl'}[H^L_{l'l}\tilde{C}^{\rm EE}_l - H^L_{ll'}\tilde{C}^{\rm BB}_l], \tag{92}$$

$$\xi^{LM}_{lml_2m_2} \equiv (-1)^m \sqrt{\frac{(2L+1)(2l_2+1)(2l+1)}{4\pi}} \begin{pmatrix} l & L & l_2 \\ -m & M & m_2 \end{pmatrix}, \tag{93}$$

$$\epsilon_{lLl_2} \equiv \frac{1+(-1)^{l+L+l_2}}{2}, \tag{94}$$

and

$$H^L_{\ell\ell_2} \equiv \begin{pmatrix} \ell & L & \ell_2 \\ 2 & 0 & -2 \end{pmatrix}. \tag{95}$$

This allows one to invert Equation 91 to obtain α_{LM} with a minimum variance estimator

$$\hat{\alpha}_{lm} = A^{\rm EB}_L \sum_{ll'} \sum_{mm'} \xi^{LM}_{lml'm'} g^{\rm EB}_{ll'} E_{lm} B^*_{l'm'}, \tag{96}$$

with

$$g^{\rm EB}_{ll'} = \frac{f^{\rm EB}_{lLl'}}{C^{\rm EE}_l C^{\rm BB}_{l'}}, \tag{97}$$

and $A_{\rm EB}$ a normalization factor, which is related to the variance of the estimator by

$$N^{\rm EB}_L = (A^{\rm EB}_L)^{-1} = \sum_{ll'} \frac{(2l+1)(2l'+1)}{4\pi} \frac{(f^{\rm EB}_{lLl'})^2}{C^{\rm EE}_l C^{\rm BB}_{l'}}. \tag{98}$$

This is the known as the minimum-variance quadratic estimator and will be used to reconstruct the anisotropic cosmic birefringence signal from the CMB polarization maps in this study.

3.3 Data and simulations

In this work we analyze ACTPol nighttime polarization data collected from two seasons of observations taken in 2014 and 2015, as described in Ref. [98]. In particular, the constraints are derived from one region of the sky, labeled as D56, which spans $\sim$ 456 deg^2 of the sky in two frequency bands, labeled as f090 and f150 centered approximately at 98 GHz and 143 GHz, respectively. The maps have an effective noise level of 14μK arcmin in polarization. Another patch of sky, called BOSS-N, was observed in the 2015 season covering 1633 deg^2 of the sky with an effective noise level of $\sim 30\,\mu$K arcmin in polarization. Due to the much higher statistical noise in this patch, data from BOSS-N contributes negligibly ($\lesssim 3\%$) to the cosmic birefringence constraint and hence is used for (swap-patch) null test only. We combined maps from different frequency bands, detector arrays, and seasons following the same Fourier-space based approach described in Ref. [39], resulting in one set of E and B maps for each sky patch (D56 and BOSS-N).

To test our reconstruction pipeline, we make Monte Carlo simulations with the standard ΛCDM Cosmology that include lensing and realistic instrument effects such as beams and inhomogeneous map noise (see [99, 100] for more details), referred to as standard simulation hereafter and are used mainly to test our reconstruction pipeline, compute biases in the power spectrum measurement, perform null tests, and compute the covariance matrix for likelihood analysis. In addition, we also generate simulations that include an anisotropic cosmic birefringence signal with varying amplitude $A_{\rm CB}$, as defined in Equation 89, to estimate transfer function for the reconstructed spectrum. To estimate the impacts of systematic errors in the reconstruction, we also generate simulated maps with global polarization angle mis-calibration and polarized dust emission obtained from Galactic dust simulation of Ref. [101] [1].

[1]The simulation provides non-Gaussian full-sky dust Q/U map at 353 GHz, which is scaled to ACT frequency assuming a modified black-body with a dust temperature and spectral index given by Ref. [102].

3.4 Analysis

We reconstruct the rotational field, $\alpha(\hat{\mathbf{n}})$, from the rotation-induced off-diagonal mode-coupling using the quadratic estimator given by Equation 96, from polarization maps in E mode and B mode. The power spectrum of the anisotropic rotation angle can then be obtained following Equation 88 (see Ref. [102] for detailed verification of this reconstruction algorithm).

To account for ground and atmospheric noise, we use the same filter as is applied for CMB power spectrum and lensing analysis in Refs. [39, 100], where Fourier modes with $|\ell_x| < 90$ and $|\ell_y| < 50$ are removed in both E and B maps. The filtered E and B maps are then projected to HEALPIX pixelization and converted to coefficient E_{lm} and B_{lm} using spherical harmonics transform. Note that the curved-sky geometry has been taken into consideration in making the polarization maps of each sky patch, and hence the computed harmonics coefficients do not have any distortion due to ignoring the curved-sky geometry.

Next we reconstruct the rotation field α using the minimum variance estimator defined in Equation 96,

$$\hat{\alpha}_{lm} = A_L^{\rm EB} \sum_{ll'} \sum_{mm'} \xi^{LM}_{lml'm'} f^{\rm EB}_{lLl'} \overline{E}_{lm} \overline{B}^*_{l'm'} \tag{99}$$

where we have used the notation $\overline{X}_{lm} \equiv X_{lm}/C_l^{XX}$ to denote the inverse variance filtered harmonic coefficients, with X being either E or B. In particular, we use CMB multipoles in the range $200 \leq \ell \leq 2048$ for our baseline reconstruction. The dependency of our results on the multipole range is tested in Section 3.5. Finally we correct for the mean-field bias, $\langle\overline{\alpha}\rangle$. This term accounts for the bias caused by non-rotation effects such as survey boundary effect, beam asymmetry effects, lensing effect, and time domain filtering applied in the preprocessing step [99, 103]. It can also be induced by global polarization angle error which we discuss in detail in Section 3.5. We evaluate the mean-field bias by averaging over the standard simulations that are described in Section 3.3. The final estimator can be written as

$$\hat{\alpha}_{LM} = A_L^{\rm EB} \left[\left(\sum_{ll'} \sum_{mm'} \xi^{LM}_{lml'm'} f^{\rm EB}_{lLl'} \overline{E}_{lm} \overline{B}^*_{l'm'} \right) - \langle\overline{\alpha}\rangle \right]. \tag{100}$$

From the reconstructed $\alpha(\hat{\mathbf{n}})$, the cosmic birefringence spectrum can be estimated in a

similar way as the CMB lensing power spectrum [103, 41]. To estimate the power spectrum of α, one effectively evaluates a 4-point correlation function which has two components: a disconnected (or Gaussian) part $N_{L,D}$ and a connected part $N_{L,C}$, following

$$\langle \alpha^*_{LM} \alpha_{L'M'} \rangle = (2\pi)^2 \delta_{LL'} \delta_{MM'} \left(N_{L,D} + N_{L,C} \right), \tag{101}$$

where the disconnected part $N_{L,D}$ dominates the total variance of the estimator $\hat{\alpha}$. As the disconnected part is sourced by the original CMB anisotropies, it is non-zero even when no cosmic birefringence is present [104, 105, 106]. With the minimum variance estimator in Equation 100, this disconnected part is minimized and becomes $N_{L,D} = N_L^{\rm EB}$. The connected part, on the other hand, is a sub-dominant component (two orders of magnitude smaller) in the total variance of the estimator $\hat{\alpha}$, given by

$$N_{L,C} = C_L^{\alpha\alpha} + N_L^{(1)} + O(\alpha^4), \tag{102}$$

where $C_L^{\alpha\alpha}$ is the power spectrum of cosmic birefringence which we are ultimately interested in, and $N_L^{(1)}$ is known as the N1 bias, which is of $O(\alpha^2)$. Therefore, to estimate $C_L^{\alpha\alpha}$, one needs to estimate and substract both the disconnected bias $N_{L,D}$ and the N1 bias. In particular, we estimate the two biases both using the standard simulations and non-zero birefringence simulation, respectively. Furthermore, we adopt a realization-dependent algorithm [107] to estimate $N_{L,D}$, instead of using the theoretical expression for $N_L^{\rm EB}$ in Equation 98. This is known to be robust to possible mismatches between simulation and data. We subsequently substract the disconnected part from the observed variance of the birefringence estimator. The N1 bias, on the other hand, is included in modeling the signal spectrum of the birefringence, instead of being substracted, though in practise the N1 bias is found to be negligible compared to the statistical error from the reconstructed birefringence spectrum which is dominated by $N_{L,D}$.

To validate our reconstruction pipeline, we perform reconstruction on simulations with non-zero birefringence. The cross-spectrum between the input and the reconstructed birefringence agrees with the input spectrum to within 0.3% for $L \geq 20$.

In this work we compute the cosmic birefringence power spectrum up to $L \leq 2048$. At larger L, the statistical uncertainties of the reconstructed spectrum start to increase significantly (see Figure 2.12 for example).

3.5 Potential systematics

The ACT polarization data have been tested for possible systematic errors in several published or forthcoming papers focusing on the CMB [99], lensing [103], and delensed spectra [108], as well as cross-spectra with galaxy surveys [39]. Here, we further test for potential systematic contamination which could bias the measured cosmic birefringence spectrum. Here and in the following sections, we use 200 realizations of the simulations to evaluate the bandpower covariance matrix for the cosmic birefringence spectrum as well as the chi-square probability-to-exceed (PTE).

3.5.1 Uncertainties in polarization angle measurement

Global polarization angle errors induce non-zero odd-parity power spectra [109, 110]. We estimate a constant global rotation angle ψ as follows. Assuming $|\psi| \ll 1$, the global rotation angle is related to the polarization spectra as

$$\psi = C_b^{EB}/2(C_b^{EE} - C_b^{BB}) \equiv a_b \tag{103}$$

at each multipole bin b [109]. We compute the angle by minimizing $\sum_{bb'}(\psi - \widehat{a}_b)\mathrm{Cov}^{-1}_{bb'}(\psi - \widehat{a}_{b'})$ where $\widehat{a}_b$ is the observed value of a_b and Cov is the covariance of a_b computed from 200 realizations of the standard simulation. With the polarization spectra at $200 \leq \ell \leq 2048$, we find that $\psi = 0.12 \pm 0.06$ deg. This global rotation introduces a significant mean-field bias particularly at very large scales, reaching a comparable level to the 1σ statistical error of the reconstructed cosmic birefringence spectrum at $L < 20$. We therefore exclude the large-scale cosmic birefringence spectrum ($L < 20$) from our analysis. Note that this scale roughly corresponds to the size of our sky patch. Thus the measured spectrum below this multipole does not have much information on cosmic birefringence signals.

An additional possible concern is the spatial variation of polarization angle errors over the observational field. In order for such variations to be significant, one would require that (1) different detectors have significantly different polarization angle errors; (2) the relative weights of different detectors vary strongly over the map, because otherwise differential

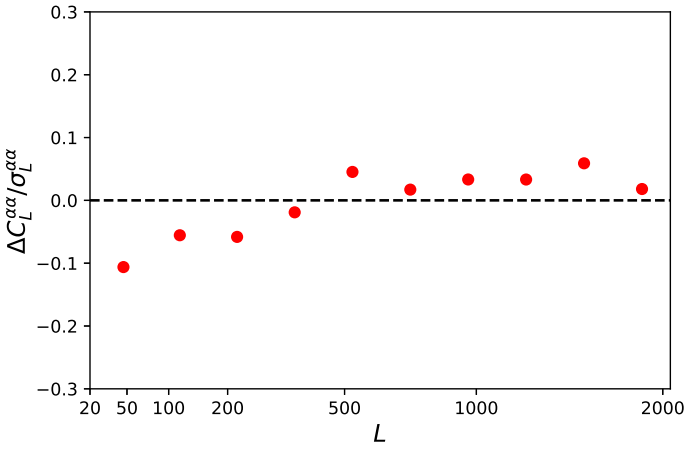

Figure 3.1: The difference of the cosmic birefringence spectra between the standard plus Galactic dust and standard simulations. Each value has been divided by the 1σ statistical uncertainty in the standard cosmic birefringence spectrum.

detector angle errors would be absorbed into the mean; (3) such effect is not significantly reduced by averaging over repeated scans. Since all of these effects are individually unlikely to be large, the likelihood of all three taking place at a significant level is very small, and we therefore neglect such effects. This is further motivated by the fact that our potential upper limits of cosmic birefrigence are, in fact, not degraded by such systematic, since uncertainty in polarization angle measurement is not correlated with a true birefringence signal. Furthermore, as both birefringence and polarization angle error spectra give strictly positive contributions to the estimated birefringence power spectrum, the presence of such a systematic would, in fact, imply stronger constraints on cosmic birefringence from a data-derived upper limit.

3.5.2 Galactic foregrounds

The large scale B-modes are significantly contaminated by Galactic foregrounds, and in principle, non-Gaussian polarized foregrounds could also bias the measured birefringence

spectrum. As our analysis removes multipoles below $\ell < 200$, we expect minimal contamination from the Galactic foregrounds in our maps. To accurately account for any bias to the reconstructed cosmic birefringence spectrum, we nonetheless test the Galactic foreground contributions to our results by adding a simulation of Galactic dust to our standard simulation. In particular, we use 20 different realizations of the Galactic dust simulation provided by Ref. [101] in the D56 region for this purpose. We scale the dust polarization maps to our observing frequencies following Refs. [111, 112], assuming a modified blackbody spectrum for dust and using the dust spectral index and temperature measured by Planck [112]. We then add the scaled polarization maps to 20 realizations of our standard CMB simulation to produce a set of 20 CMB simulations including dust.

In Figure 3.1 we show the difference spectrum between the simulations including dust and the standard simulations, averaged over 20 realizations. The spectrum is further normalized by the 1σ statistical error of the cosmic birefringence spectrum obtained from 200 realizations of the standard simulation. Although we do not yet have sufficient multi-frequency data to fully exclude any impact of Galactic foregrounds, results based our simulations show that the impact of the dust contribution to our reconstructed cosmic birefringence power spectrum is likely small, being approximately $\lesssim 10\%$ of our statistical uncertainty at each multipole bin.

3.5.3 Null tests

As a null test, we compute the cross spectrum of the reconstructed rotation field α obtained from the D56 and BOSS-N fields. As we expect the reconstructed rotation fields to be uncorrelated on these two patches, the cross spectrum should be consistent with zero. Following the same procedures as applied to the D56 field, the cosmic birefringence anisotropies from BOSS-N are reconstructed using the same quadratic estimator described in Section 3.4 and are then cross-correlated with the birefringence map from D56. This cross spectrum can serve as a valuable test of whether our error bars are correct and whether any unforeseen systematic errors exist in the data. Figure 3.2 shows the cross spectrum; we find that the spectrum is consistent with null, with the χ^2 PTE of the cross spectrum within the nominal

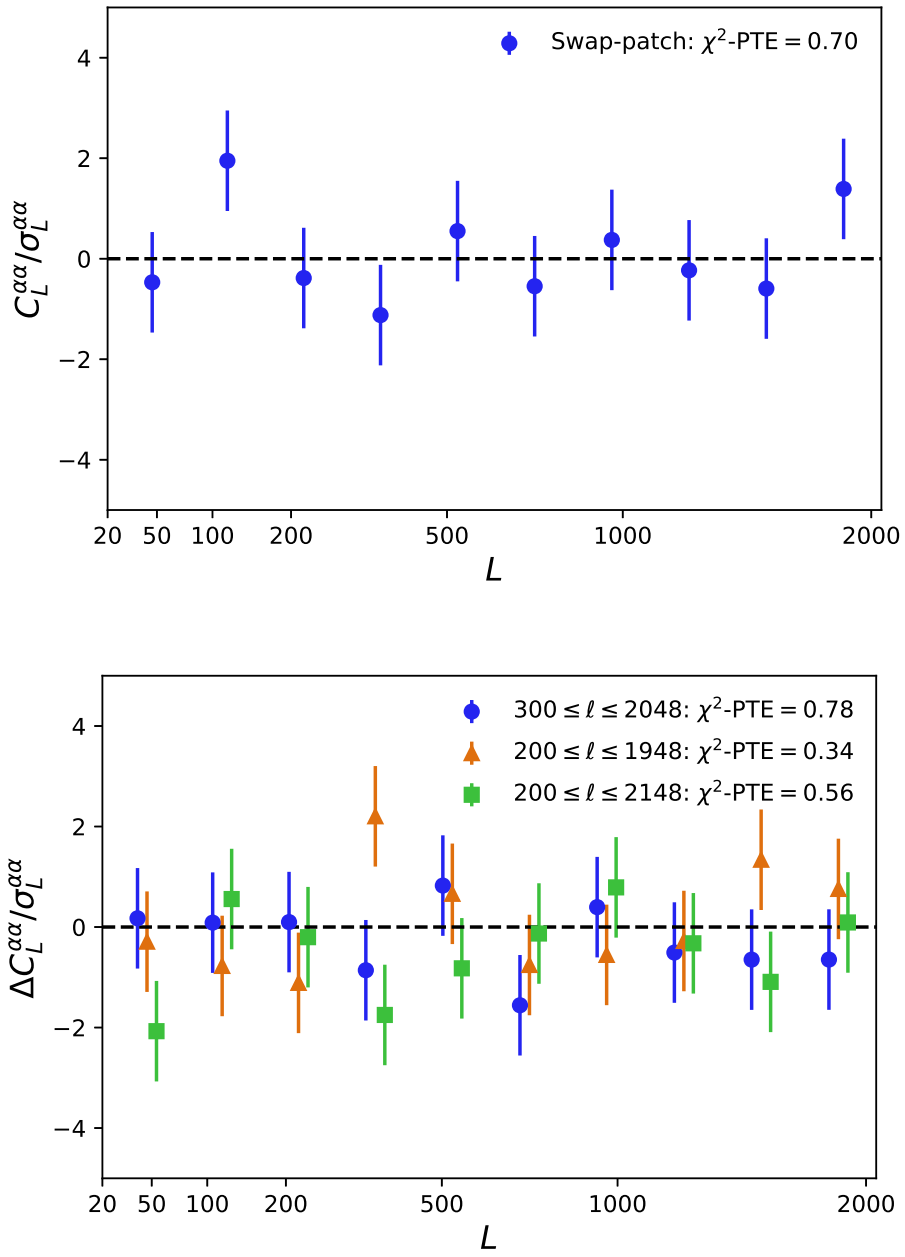

Figure 3.2: The null cosmic birefringence spectra for the swap patch (upper panel) and difference spectra (lower panel) tests, each divided by the statistical 1σ error of the spectrum. For the swap patch, we show the cross spectrum of the reconstructed cosmic birefringence anisotropies between two separate patches of sky, `D56` and `BOSS-N`.

range.

For additional null tests, we also compute the difference between the baseline analysis and cases with different choices of CMB multipole ranges used for the rotation field reconstruction. Figure 3.2 shows the difference spectra and the χ^2 PTE calculated for each difference spectrum. The result shows that difference spectra are consistent with the null hypothesis regardless of the choice of the CMB multipole range.

3.6 Reconstructed spectrum

After passing the null tests in Section 3.5, we unblinded the reconstructed cosmic birefringence spectrum. Figure 3.3 shows the cosmic birefringence spectrum from ACTPol data with error bars estimated from the standard simulation. For comparison, the figure also shows the cosmic birefringence power spectra measured by other recent CMB experiments: BICEP2/Keck Array [5], POLARBEAR [4], and Planck [6]. Compared to other experiments, ACTPol provides the tightest constraint on the cosmic birefringence spectrum at $20 \leq L \leq 2048$. We compute the χ^2 PTE of our measured spectrum based on covariance obtained from simulation, and the value is found to be 0.99, which is in good agreement with zero signal. We also note that the off-diagonal elements of the correlation matrix for this measurement become ~ 0.5 at $L > 1000$, while at lower L the off-diagonal correlations are negligible.

We note that the χ^2 PTE is close to unity, which might be an indication of an overestimation of error bars. To investigate this further, we check the dependency of the χ^2 PTE on analysis choices such as the minimum multipole used to compute the PTE ($L_{\rm min}$) and the size of each bin (N_b). The results are summarized in Table 3.1, which shows that the χ^2 PTE values are typically less than 0.95. Note that the values in Table 3.1 are not statistically independent from the baseline value since we only modify the analyzed data by a small amount by changing $L_{\rm min}$ (and changing the number of multipole bins does not introduce any new data). However, if we had significantly overestimated our error bars, we would expect that with these other analysis choices one would consistently also get very high PTE values,

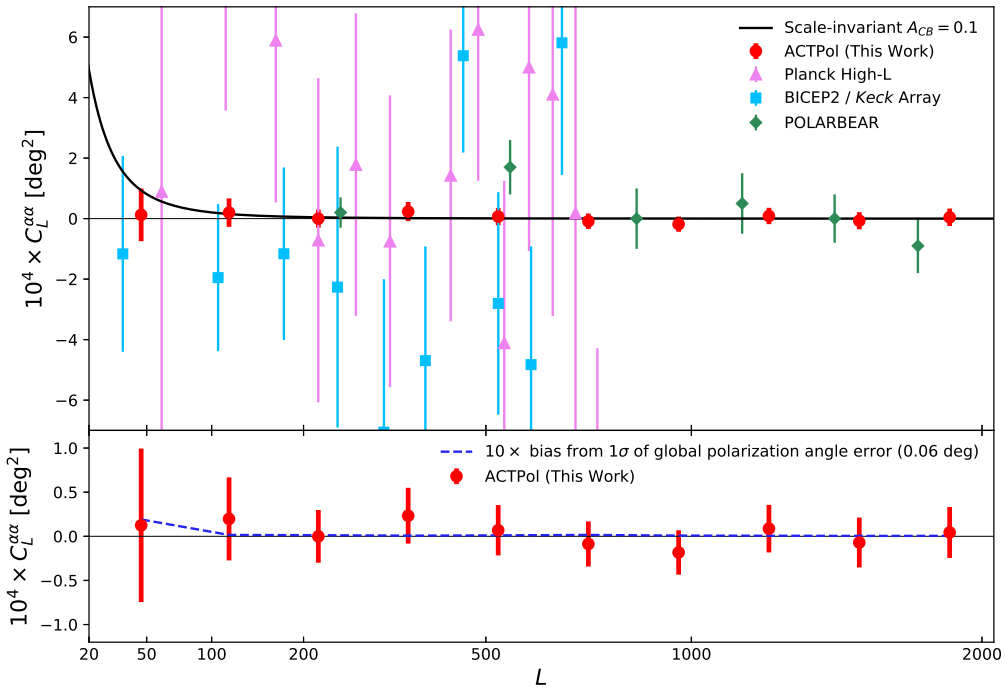

Figure 3.3: The angular power spectrum of the polarization rotation fields $\alpha(\hat{\mathbf{n}})$ measured from ACTPol data over 456 deg^2 of sky, with errors from a standard ΛCDM simulation. The solid line shows a scale-invariant spectrum with the amplitude corresponding to our 2σ upper bound (see Section 3.6). In addition to our work (red), we also show the spectra obtained from POLARBEAR (green) [4], BICEP2/Keck Array (blue) [5] and Planck (magenta) [6]. The Planck Low-L results are not included due to the error bar size. The lower panel shows a zoomed-in view of our birefringence power spectrum measurement; we also show, with a blue dotted line, the potential bias from a global polarization angle systematic error of 0.06 deg, which is of the same size as the one sigma error from an EB-derived constraint. Since this is difficult to see, for visualization, we have multiplied this angle error bias by a factor 10.

$L_{\rm min}$	χ^2 PTE	N_b	χ^2 PTE
10	0.85	15	0.77
30	0.94	20	0.88

Table 3.1: The χ^2 PTE values for our measured cosmic birefringence spectrum with varying the minimum multipole, $L_{\rm min}$, or number of multipole bins, N_b. For the baseline analysis, where $L_{\rm min} = 20$ and $N_b = 10$, the PTE is 0.99; the variation seen in this table, given different analysis choices, is consistent with this high PTE being a fluctuation.

which is not seen. In addition, as described previously, we have performed several null tests where simulations are used to evaluate the scatter, without finding anomalous PTEs. The high χ^2 PTE for the baseline spectrum therefore is likely due to a statistical fluctuation rather than an overestimate of the errors. Of course, if in fact the errors have been slightly overestimated, our limit on the cosmic birefringence will be somewhat conservative.

Note that the minimum CMB multipole used in the cosmic birefringence reconstruction is $\ell_{\rm min} = 200$, which is considerably lower than that of the lensing reconstruction presented in Ref. [103]. In the lensing analysis, the CMB multipoles below $\ell_{\rm min} = 500$ were removed since the simulations are not consistent with temperature data at these scales due to inaccurate atmospheric noise characterization and transfer function estimation. For this analysis, however, the temperature data are not used, and the measured polarization noise spectrum is consistent with simulations for $\ell \geq 200$. In addition, as demonstrated by our null tests in Figure 3.2, changing the minimum multipole used does not produce any spurious signals. To further test this, we evaluate the χ^2 PTE of a measured spectrum analyzed with $\ell_{\rm min} = 300$, finding that the value effectively does not change from the case with $\ell_{\rm min} = 200$; in addition, all our null tests still pass. These facts indicate that the inclusion of low-ℓ CMB polarization data does not introduce non-negligible systematics into our measurement.

As an example of the cosmological implications of our measurement, we consider a con-

straint on the amplitude of the scale-invariant spectrum, $C_L^{\alpha\alpha} \propto 2\pi/L(L+1)$, which can be later translated into, for example, a constraint on the coupling constant of an axion-like particle. To constrain a scale-invariant spectrum, we first construct an approximate likelihood for the reconstructed cosmic birefringence power spectrum. Although we do not use multipoles at $L < 20$, the distribution of the power spectrum in the largest bin is asymmetric and is not well described by a Gaussian based on our simulation. Instead, we assume the log-likelihood proposed by [72]:

$$-2\ln\mathcal{L}(\widehat{\boldsymbol{A}}) = \sum_{bb'} g(c_b^0\widehat{A}_b)[c_b^1 C_b^f]\mathrm{Cov}_{bb'}^{-1}[c_{b'}^1 C_{b'}^f]g(c_{b'}^0\widehat{A}_{b'})\,, \tag{104}$$

where we use the $\widehat{X}$ notation are denote data-derived quantities; those without are theory- or simulation-derived quantities. In particular, $\widehat{A}_b \equiv (\widehat{C}_b^{\alpha\alpha} + \langle\widehat{N}_b^0\rangle)/(C_b^{\alpha\alpha} + \langle\widehat{N}_b^0\rangle)$ is the ratio between the estimated and the expected amplitudes of the quadratic estimator power spectrum. $C_b^{\alpha\alpha}$ is the cosmic birefringence signal at each multipole bin b, and $g(x) \equiv \mathrm{sign}(x-1)\sqrt{2(x-\ln x-1)}$ for $x \geq 0$. The power spectrum, C_b^f, and covariance, $\mathrm{Cov}_{bb'}$, are evaluated as the mean and variance of the quadratic estimator power spectrum obtained from the standard simulation, respectively. Note that we further introduce two free parameters, c_b^0, c_b^1, to match the above likelihood to that obtained from the simulation. In particular, we compute c_b^0 and c_b^1 by fitting the histogram of $\widehat{A}_b$ obtained from the simulation using Equation 104 at each bin. We have also verified that the values of c_b^0 and c_b^1 only change by negligible amounts when using simulations with different levels of birefringence signal, which indicates a sensible fit.

Using Equation 104, we compute the likelihood for the amplitude of the scale-invariant power spectrum defined by $L(L+1)C_L^{\alpha\alpha}/2\pi = A_{\rm CB}\times 10^{-4}$. Assuming a flat prior for $A_{\rm CB} \geq 0$, we then obtain the 2σ upper limit on the amplitude as $A_{\rm CB} \leq 0.10$. This constraint improves the previous best constraints by a factor of between 2 and 3 [6, 5]. Note that, for the scale-invariant power spectrum, the constraint on its amplitude is mostly determined by the largest-scale multipole bin; removing the first multipole bin centered at $L = 47$ degrades the constraint considerably.

3.7 Discussion

Our measured spectrum can be used to constrain various models which lead to cosmic birefringence anisotropies. As an example, we consider the following interaction between axion-like particles and photons in the Lagrangian [113]:

$$\mathscr{L} \supset \frac{g_{a\gamma} a}{4} F_{\mu\nu} \tilde{F}^{\mu\nu} \,, \tag{105}$$

where $g_{\alpha\gamma}$ is the Chern-Simons coupling constant between the axion-like particles and photon, a is the axion-like particle field, $F_{\mu\nu}$ is the electromagnetic field, and $\tilde{F}^{\mu\nu}$ is its dual. The presence of axion-like particles produces a rotation of the polarization angle as [113, 114]:

$$\alpha = \frac{g_{a\gamma}}{2} \Delta a \,, \tag{106}$$

where Δa is the change in a over the photon trajectory. Fluctuations in the axion-like particle field lead to the spatial variation of α. If the axion-like particle is effectively massless during inflation, the primordial power spectrum of the fluctuations of the axion-like particle field is scale-invariant. As a result, the cosmic birefringence power spectrum becomes a scale-invariant spectrum in the large-scale limit ($L \lesssim 100$) [94]:

$$\frac{L(L+1)C_L^{\alpha\alpha}}{2\pi} = \left(\frac{H_I g_{a\gamma}}{4\pi} \right)^2 \,. \tag{107}$$

Here, H_I is the inflationary Hubble parameter and is related to the tensor-to-scalar ratio r, as $H_I = 2\pi M_{\rm pl} \sqrt{A_s r/8} \simeq \sqrt{4r} \times 10^{14}$ GeV where $M_{\rm pl} \simeq 2 \times 10^{18}$ GeV is the reduced Planck mass and $A_s \simeq 2 \times 10^{-9}$ is the amplitude of the primordial scalar perturbations (see, e.g., [115]). Using Equation 107, our $A_{\rm CB}$ constraint can be translated into constraints on coupling between axion-like particles and photons as

$$g_{a\gamma} \leq 4.0 \times 10^{-2} / H_I \,. \tag{108}$$

A detection of the tensor-to-scalar ratio in a future CMB experiment, which determines H_I, will thus allow us to put a upper limit on $g_{\alpha\gamma}$ from the CMB cosmic birefringence.

Measurements of anisotropic cosmic birefringence can be of great importance for testing new physical theories of the early Universe. Future CMB experiments such as the BICEP

Array [116], CMB-S4 [74], LiteBIRD [32], Simons Observatory [117], and SPT-3G [118] will measure cosmic birefringence anisotropies even more precisely [119]. In these experiments, a curved-sky polarization analysis, as we have presented here, will be necessary to tightly constrain a scale-invariant spectrum of cosmic birefringence anisotropies.

4.0 Observing the Galactic Center with the Atacama Cosmology Telescope

Ground-based CMB experiments like ACT provide sensitive and high angular resolution measurements of the millimeter sky in both total intensity and polarization. Not only are such measurements important for the CMB science, they are also valuable for astronomy, though such possibility has not been explored extensively. In this chapter I present a work that explores such possibility in which we make a map of Galactic center region of our Milky way galaxy using data from ACT. This work is a product of collaborative work by Susan E. Clark, Brandon S. Hensley, and myself, in the form of an ACT Collaboration paper. The manuscript that this chapter is based on has been submitted to Astrophysical Journal for publication.

4.1 Introduction

Some of the most extreme interstellar environments in the Galaxy are found in the Galactic center (e.g., [120]). The inner $\sim 500\,\mathrm{pc}$ of the Milky Way is home to the Central Molecular Zone (CMZ), the densest concentration of molecular gas in the Galaxy, with a mean density of $\sim 10^4\,\mathrm{cm}^{-3}$ [121, 122]. The surface density of dense gas greatly exceeds that found in nearby star-forming molecular clouds. Standard prescriptions predict that the CMZ should be an extremely active site of star formation, and yet the observed star formation rate is low; by some estimates, an order of magnitude or more below predictions (e.g., [123, 124, 125] and references therein).

The apparently inefficient star formation in the CMZ makes this region an ideal testbed for star formation theories, with many factors proposed to explain the observations. These include the strong magnetic field in the Galactic center [126, 127, 128], the rate of mass inflow to the CMZ [129], the strength and compressibility of turbulence in the CMZ [130], and the possibility that we are observing a relatively quiescent period between episodic bursts of star formation [131, 132]. Furthermore, the CMZ is in some respects a nearby analogue of

nuclear rings in other galaxies, including high-redshift starbursts. The Galactic center is thus an opportunity for up-close study of the physics relevant to the cosmic history of star formation [133, 134].

The magnetic field in the vicinity of the Galactic center has long been studied with radio polarimetry [135, 136]. The so-called non-thermal radio filaments – thin strands of radio-frequency emission – were some of the earliest observations to shed light on the magnetic field structure toward the Galactic center. The non-thermal radio filaments are, for the most part, strikingly perpendicular to the Galactic plane, and the intrinsic magnetic field inferred from the Faraday de-rotated polarized synchrotron emission tends to lie parallel to the long axis of these filaments [137, 138, 139].

Polarized dust emission provides a complementary means of probing the magnetic field structure in the CMZ. Interstellar dust grains emit partially polarized thermal radiation because they are aspherical and preferentially align their short axes parallel to the ambient magnetic field [140]. The polarization angle of the dust emission is thus a line-of-sight integrated probe of the plane-of-sky component of the magnetic field orientation. Polarized dust emission has been measured at high angular resolution in small regions toward a number of CMZ molecular clouds (e.g., [141, 142, 127, 143, 144]). Recently, the balloon-borne experiment PILOT presented a 240 μm map of the polarized dust emission over the entire CMZ region at 2.2′ resolution [145], along with comparisons to the lower-resolution 353 GHz polarization data measured by the Planck satellite [146].

The Atacama Cosmology Telescope (ACT) measures the polarized microwave sky with higher angular resolution than the Planck satellite and greater sensitivity on small scales. In this chapter we present new dedicated maps of the Galactic center in total intensity and linear polarization in three ACT frequency bands. We combine the ACT data with Planck data to augment the map sensitivity on larger angular scales. The frequency coverage of the maps presented here probe a range of physical emission mechanisms, enabling a comprehensive view of the Galactic center environment. In polarization these maps probe both polarized dust and synchrotron emission, and in total intensity the maps additionally show features from free-free emission and molecular line emission from transition frequencies that fall within the ACT passbands. These data illustrate the potential of sensitive CMB polarization

experiments for Galactic science.

We describe the ACT observations in Section 4.2 and the mapmaking and Planck coadd procedures in Section 4.3. In Section 4.4 and 4.5, we present the maps in total intensity and polarization, respectively, and discuss derived properties including emission mechanisms, magnetic field orientation, and polarization fraction. In Section 4.6, we identify notable Galactic center objects and compare to observations at other frequencies. We conclude in Section 4.7.

4.2 Observations

ACT is a 6-meter off-axis Gregorian telescope located at an elevation of 5190 m on Cerro Toco in the Atacama Desert in Chile [147, 84]. ACT scans the millimeter-wave sky with arcminute resolution, complementary to the full-sky lower angular-resolution measurements from satellite missions such as the Wilkinson Microwave Anisotropy Probe (WMAP) [148] and Planck [149].

In 2019, the target ACT observating fields were expanded to include the Galactic center region. Between June 6 and November 29, 2019 a total duration of ~ 35 hours of data were taken with three Advanced ACTPol dichroic detector arrays PA4, PA5, and PA6 [150, 151, 152], at three frequency bands f090, f150, and f220 centered roughly at 98 GHz, 150 GHz, and 224 GHz, respectively. The beam full-width-half-maximum (FWHM) at each band is $2.0'$, $1.4'$, and $1'$, respectively. The observation field extends roughly from $-89°$ to $-97°$ in declination and $-33°$ to $-25°$ in right ascension. This study focuses specifically on a 32 deg^2 field near the CMZ with Galactic longitude $|l| \leq 4°$ and Galactic latitude $|b| \leq 2°$.

In this chapter we present the maps made using the nighttime observations only, which constitute roughly two-thirds of the total data collected. The daytime observations are affected by a time-dependent beam deformation due to the heating from the Sun that is challenging to correct for in detailed high-resolution maps, and hence those data are excluded from this analysis. Correcting for this beam deformation will be a subject of future study, and the daytime observations may be included for future versions of these maps.

4.3 Mapmaking

4.3.1 Mapmaking with ACT

The instrument records observations in the form of time-ordered data (TOD) in units of $\sim$ 10 minutes. We largely follow the mapmaking pipeline as described in Ref. [98] with a few key differences, as we briefly summarize below.

First, we cut bad samples affected by glitches in each TOD. To prevent bright sources in the Galactic center region from being mistaken for glitches, we mask sources brighter than 5 mK with a radius of $3'$ prior to applying the glitch finder. We note that this mask is only applied when identifying glitches and not used during mapmaking. Timestreams with outlying statistical properties in terms of noise levels and optical responsiveness are then flagged and removed from the analysis. We further split the dataset into two independent subsets for each frequency band and detector array respectively, resulting in 12 datasets in total. We then obtain the sky maps for each dataset by solving the mapping equation,

$$d = Pm + n, \tag{109}$$

for a set of Stokes parameters (I, Q, U), where d is the pre-processed time-streamed data, P is the pointing matrix, m is the output map of interest, and n is the noise model. This equation yields a maximum likelihood solution for m by inverting

$$(P^T N^{-1} P)m = P^T N^{-1} d, \tag{110}$$

where N is the detector-detector noise covariance.

There are two notable differences between the pipeline used in this study and that presented in Ref. [98]. First, we have adopted a new calibration method that improves gain stability and reduces biases from thermal contamination as compared to the method in ACT Data Release 4 (DR4) [98]. The second difference relates to the handling of point sources and extended hot regions that are common in the Galactic center region but uncommon in CMB fields. Directly applying the mapmaking pipeline in ACT DR4 leads to stripes around the bright sources caused by model errors as explained in Ref. [153]. This happens for two

reasons. (1). A pixelated map does not capture the sub-pixel behavior of the sky. These residuals are proportional to the gradient of the signal across a pixel and are often fractionally small. However, if the sky is sufficiently bright, such as in the brightest parts of the Galactic center, they can still end up being large in absolute terms. Since the map m in Equation 109 cannot capture these residuals, the model forces them to be interpreted as part of the noise n. (2). The correlated noise model used in the mapmaker induces a non-local response to the sub-pixel noise, leading to biases on the scale of the noise correlation length. To avoid this problem, we first identify the regions that source the strongest model errors, namely the brightest parts of the Galaxy, and then eliminate model errors in these pixels by allocating an extra degree of freedom for each sample that hit them, as described in Ref. [153].

A caveat concerning these maps is that the bright parts of the Galaxy were not masked when building the noise model N. The noise model estimator assumes that the time-ordered data is noise-dominated ($d \approx n$), and uses this to measure the noise covariance directly from d. This breaks down when the telescope scans across the Galactic center, resulting in an overestimate of the noise amplitude especially on smaller scales. This has two consequences: (1). The data are weighted sub-optimally in Equation 110, resulting in slightly higher noise. Since the maps are strongly signal-dominated, this can be ignored. (2). Because the noise model is contaminated by the same signal it is applied to, there is a small loss in signal power in the maps; pixels where noise happens to add constructively to the signal have more power in d than in pixels where they partially cancel. Since we use inverse variance weighting, the latter are up-weighted compared to the former. The size of this effect is limited because the problematically bright regions make up a small fraction of the total samples used to build N. We have not measured the precise size of this effect, but estimate it to be $\lesssim 1\%$ based on experience with other high-S/N regions, and hence we expect it to have negligible impact on the interpretation of the maps in this chapter. This deficiency will be rectified in the upcoming ACT DR6 maps.

A final known issue requiring mitigation is temperature-to-polarization (T-to-P) leakage. ACT typically scans a given region of the sky both during its rising and setting. As the Galactic center region is at relatively low declination, rising scans and setting scans are poorly cross-linked (for more information on ACT scan strategy see Ref. [154]). Furthermore,

the ACT beam is known to leak temperature to polarization at the percent level. This beam leakage effect averages down effectively in the nominal CMB maps which are well cross-linked, but in the Galactic center region the T-to-P leakage is apparent at a $\sim$ 1–2% level that contaminates the polarization maps in the bright Galactic plane. To reduce the contamination from beam leakage, we build a 2D leakage beam model for each dataset using observations of Uranus made in the same observation year (2019), and deproject the expected T-to-P leakage from the polarization maps in each dataset.

Following these methods, we produced two-way split maps of the Galactic center region at $0.5'$ resolution in Plate Carreé (CAR) projection for each frequency band (f090, f150, f220) and detector array (PA4, PA5, PA6) resulting in a total of 12 maps.

4.3.2 Coadd with Planck

The large angular scales in the ACT maps are affected by atmospheric noise contamination and complicated co-variances at large scales. These modes can be recovered, however, by coadding ACT maps with maps from Planck, which dominate the signal-to-noise at large scales $\ell \lesssim 1000$. In particular, we have used a similar algorithm as presented in ACT DR5 [155], in combination with the Planck High Frequency Instrument (HFI) maps processed through the NPIPE pipeline [156], which are two-way split maps featuring improved noise level and systematic control as compared to the previous Planck data releases.

As the coadding algorithm is presented in detail in Ref. [155], we only briefly summarize the steps and note differences here. First, we re-project the Planck maps and noise models from HEALPix[1] [157] projection with $N_{\rm side} = 2048$ into the ACT Galactic center observation footprint in CAR projection with $0.5'$ pixelization using bi-cubic interpolation. We have used the same passbands as in Ref. [155] and similarly matched the Planck 100 GHz maps with ACT f090 maps, 143 GHz with ACT f150, 217 GHz with ACT f220. This process assumes that the ACT and Planck passbands are equivalent. We note that this introduces additional scale dependence to the effective band-centers [155]. This is expected to have negligible impact on the results presented here but is relevant for component-separation analysis, which

[1] `http://healpix.sf.net`

will be the subject of follow-up work.

We then solve for the maximum likelihood coadded maps using a block-diagonal equation

$$\begin{pmatrix} m_0 \\ m_1 \\ \vdots \end{pmatrix} = \begin{pmatrix} B_0 \\ B_1 \\ \vdots \end{pmatrix} B_{\rm out}^{-1} m + n, \tag{111}$$

where m_i refers to each individual map, B_i refers to its corresponding beam transfer function, m refers to the final coadded map with a desired beam $B_{\rm out}$, which is the ACT beam in this case. n refers to the map noise, which is assumed to be Gaussian and block-diagonal across individual maps, i.e., individual maps have independent noise realizations. Of the noise models presented in Ref. [155], we have adopted the constant correlation noise model, though the choice makes little difference in practice as we are considering only a small patch of sky with close to uniform noise levels. We invert Equation 111 to find a maximum-likelihood solution to the coadded map at f090 and f150, respectively. Because the PA4 array had a poor detector yield over the course of the observation, maps at f220 are treated differently from the other two frequencies. The resulting excess noise in the ACT f220 maps leads to a lack of convergence when solving for a coadded map through a maximum likelihood approach. Therefore, we instead perform a straightforward inverse-variance weighting in Fourier space to obtain the coadded map at f220.

One caveat in using the Planck HFI maps is that a Cosmic Infrared Background (CIB) monopole model was deliberately included on a per-frequency basis due to a lack of sensitivity to the absolute emission level. We therefore subtracted the CIB monopole in each coadded map following Table 12 in Ref. [158].

This procedure yields a total of three coadded maps in both temperature and polarization at f090, f150, and f220, as summarized in Table 4.1. We present a side-by-side comparison between Planck maps and our three coadded maps in total intensity in Figure 4.1, and a similar comparison for polarized intensity for f150 in Figure 4.2. It is apparent that the addition of ACT data significantly improves the angular resolution of the maps in both temperature and polarization. The coadd polarization maps are presented in Figure 4.3 in Galactic coordinates. We use the IAU polarization convention, in which the polarization

band	Planck dataset	ACT datasets	total
f090	100 GHz	f090 PA5+PA6	6
f150	143 GHz	f150 PA4+PA5+PA6	8
f150	217 GHz	f220 PA4	4

Table 4.1: Subsets of maps coadded at each frequency band. All input maps are two-way split maps. The column "total" shows the total number of maps coadded in each band. For example, 6 different maps went into making the f090 coadd map, consisting of two splits from ACT PA4, ACT PA5, and Planck 100 GHz, respectively.

angle measures 0° towards Galactic North and increases counter-clockwise [159]. The ACT Collaboration has adopted the IAU convention for all ACT data products since DR4. This is in contrast to the COSMO convention [157] adopted in, e.g., the Planck data releases, that is related to the IAU convention via a sign flip of Stokes U, i.e., $U_{\rm COSMO} = -U_{\rm IAU}$.

A detailed discussion of these maps is presented in Section 4.4 for total intensity maps and in Section 4.5 for polarization maps. The final coadded maps have median noise levels of 36 μK arcmin at f090, 33 μK arcmin at f150, and 270 μK arcmin at f220.

4.4 Total intensity maps

Figure 4.1 shows the total intensity maps for both Planck-only and the coadded maps for our three frequency bands (f090, f150, f220). Many prominent features that were obscured or unresolved in the Planck maps become apparent with the addition of ACT data, and qualitative changes in map morphology with frequency are evident. The Galactic Center Radio Arc (GCRA), a prominent filament in the Galactic center, is visible at both f090 and f150 near the center of the coadded maps and to a lesser extent at f220, consistent with it being a strong source of synchrotron radiation [160].

The ACT frequency coverage probes a variety of emission mechanisms, including synchrotron, free-free, thermal dust, and molecular line emission, at different levels in each of the three bands. To better visualize the different structures probed at each frequency band, we combine the coadded maps from three frequency bands into a multi-color image shown in the upper panel of Figure 4.4. The red, green, and blue image channels represent the f090, f150, and f220 maps, respectively, after appropriate re-scaling. The intensity scaling (as detailed in the Figure 4.4 caption) was chosen to highlight structures in different bands and to make feature identification easier. An annotated zoom-in of the three-color intensity map in Figure 4.4 is provided in the top panel of Figure 4.5.

The coherent structures visible in the different colors of Figure 4.4 and 4.5 arise from spatial variations in the relative strengths of the various emission mechanisms. The radio spectrum of supernova remnants (SNR) originates primarily from synchrotron emission [161], and thus objects like the SNR candidate G357.7-0.1 ("the Tornado") [162] and SNR0.9+0.1 [163] appear reddish yellow in Figure 4.4. Similarly, Sgr A* and the GCRA (see, e.g., [164, 165]) are strikingly highlighted in this color, consistent with their strong synchrotron emission spectrum. Pulsar wind nebulae (PWN), like the Crab Nebula, also emit highly polarized synchrotron emission with a flat spectral index [166], in contrast to SNRs which generally emit synchrotron with a slightly lower polarization fraction and a steeper spectrum.

Thermal emission from interstellar dust dominates Galactic emission at far-infrared / submillimeter frequencies. Known molecular clouds like the Brick (G0.253+0.016; e.g., [167]), the 20 $\mathrm{km\,s^{-1}}$ Cloud (G359.889–0.093) and 50 $\mathrm{km\,s^{-1}}$ Cloud (G0.070-0.035; e.g., [168]),

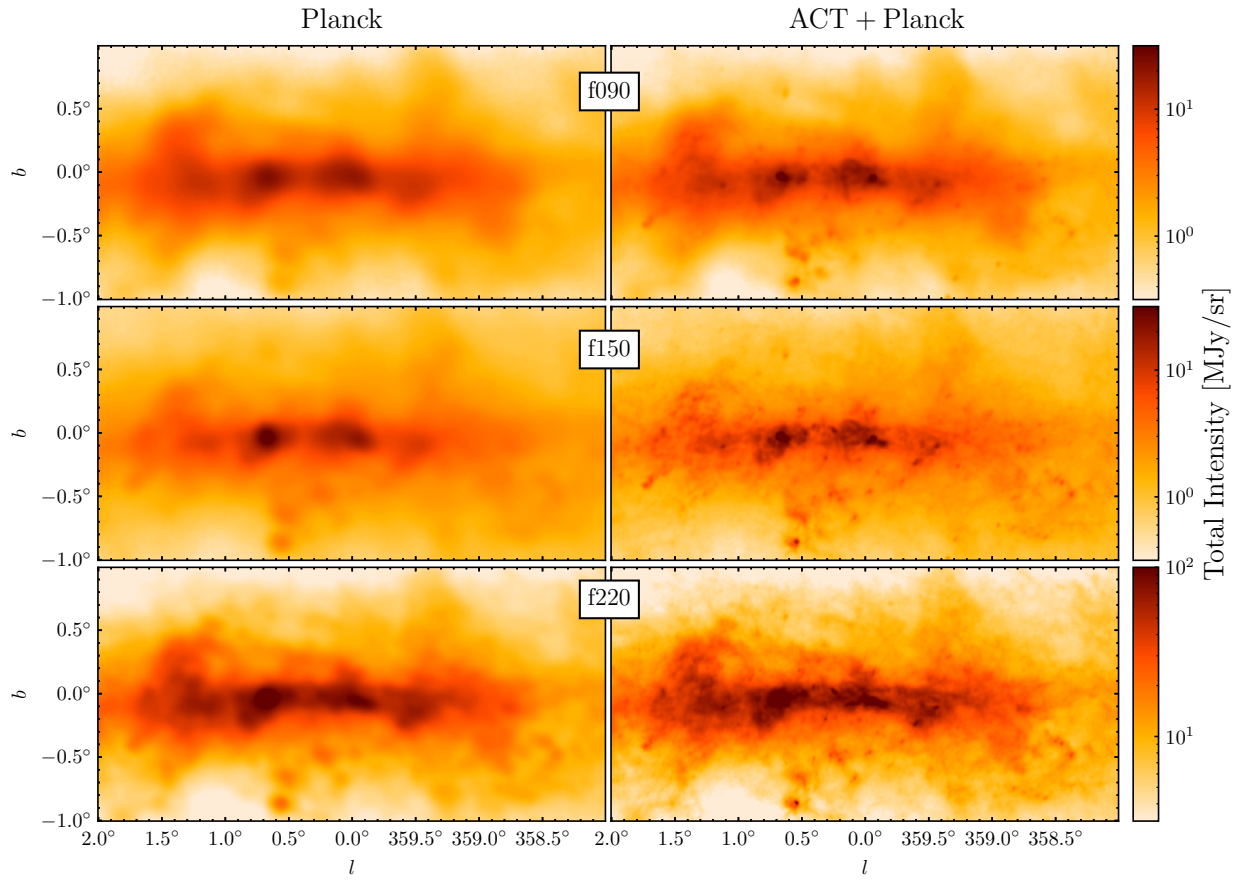

Figure 4.1: Comparison between Planck only maps (left column) and ACT+Planck coadded maps (right column) in total intensity. Rows from top to bottom correspond to f090, f150, and f220 respectively. Each map extends from $|l| \leq 2°$, $|b| \leq 1°$ and is plotted on a logarithmic color scale from 0.3–30 MJy sr^{-1} for f090 and f150, and from from 3–100 MJy sr^{-1} for f220.

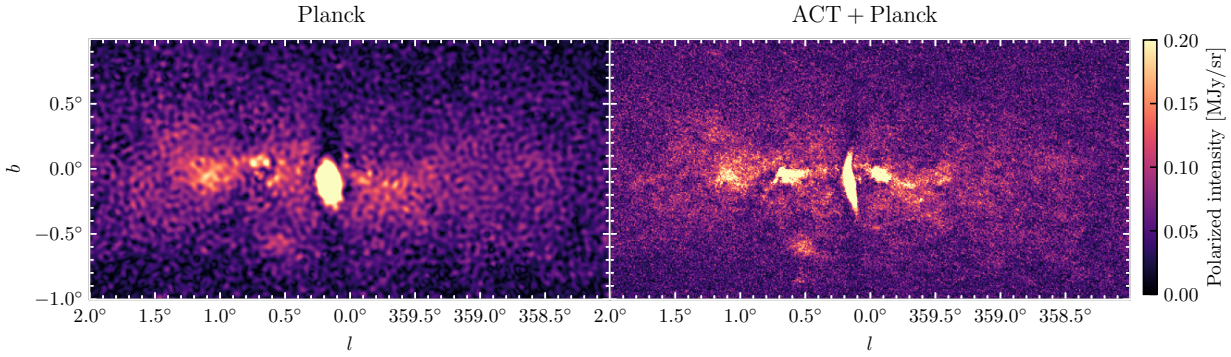

Figure 4.2: A side-by-side comparison between Planck only (left) and the ACT+Planck coadded (right) for f150 in polarized intensity.

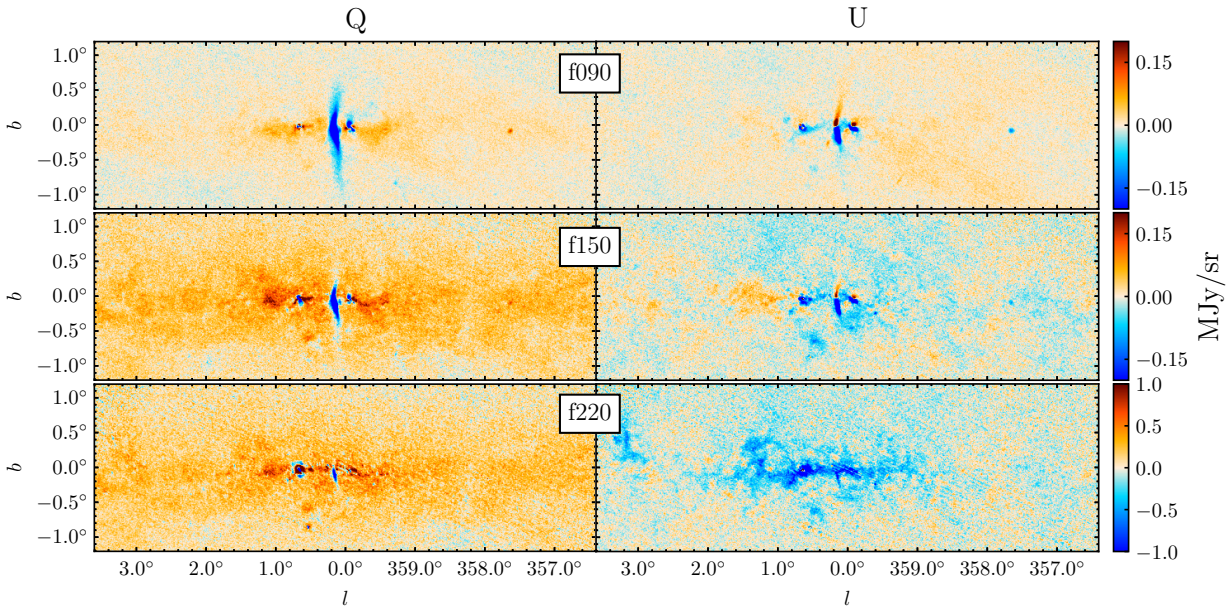

Figure 4.3: Polarization maps in Stokes Q (left column) and U (right column) in Galactic coordinates and using the IAU polarization convention. Top to bottom are the f090, f150, and f220 maps, respectively.

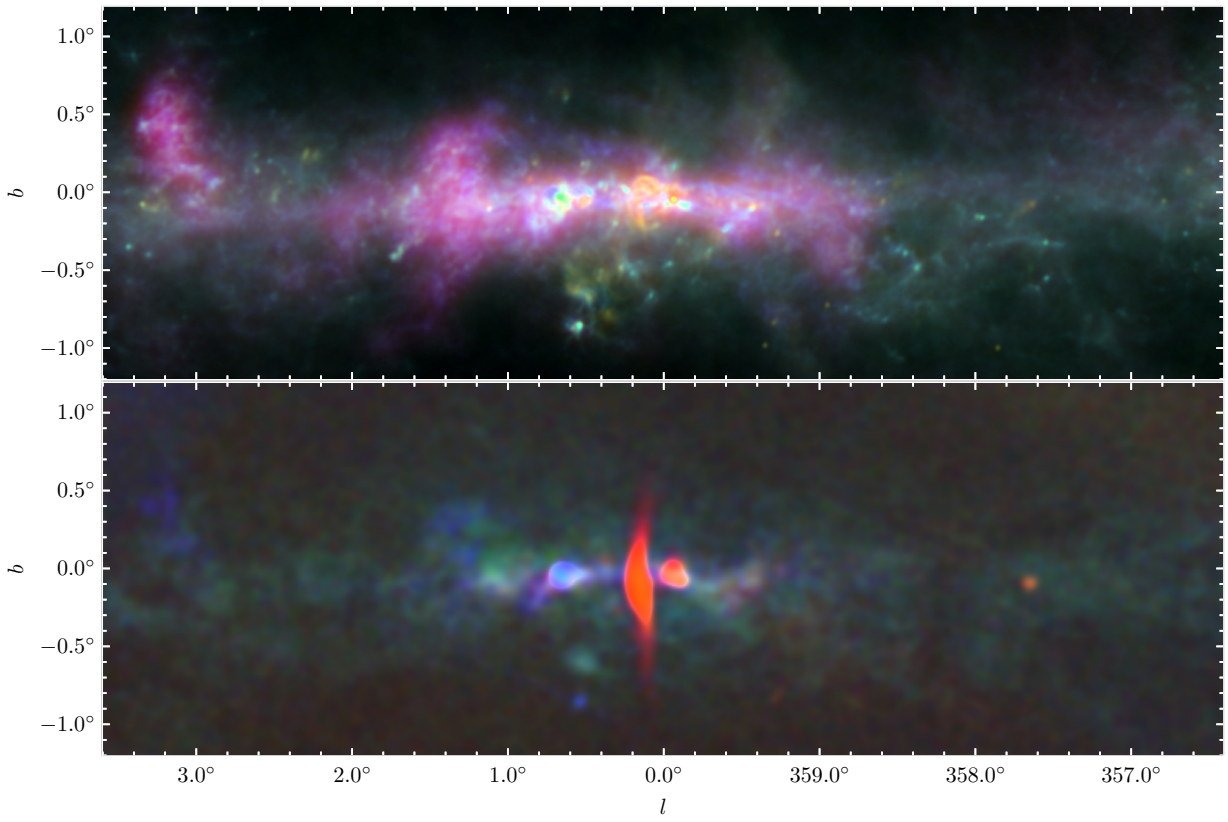

Figure 4.4: Multi-frequency view of the Galactic center region in both total intensity (upper panel) and polarized intensity (lower panel). Red, green, and blue correspond to f090, f150, and f220, respectively. In the upper panel, the maps are scaled logarithmically from 0.2 to 2 MJy sr^{-1} for f090, from 0.214 to 2.14 MJy sr^{-1} for f150, and from 1.15 to 10.15 MJy sr^{-1} for f220. The polarization maps shown in the lower panel are first smoothed with a Gaussian kernel (FWHM= 3.5′) and then scaled linearly from 0 to 1 MJy sr^{-1} for f090, to 1.79 MJy sr^{-1} for f150, and to 8.2 MJy sr^{-1} for f220.

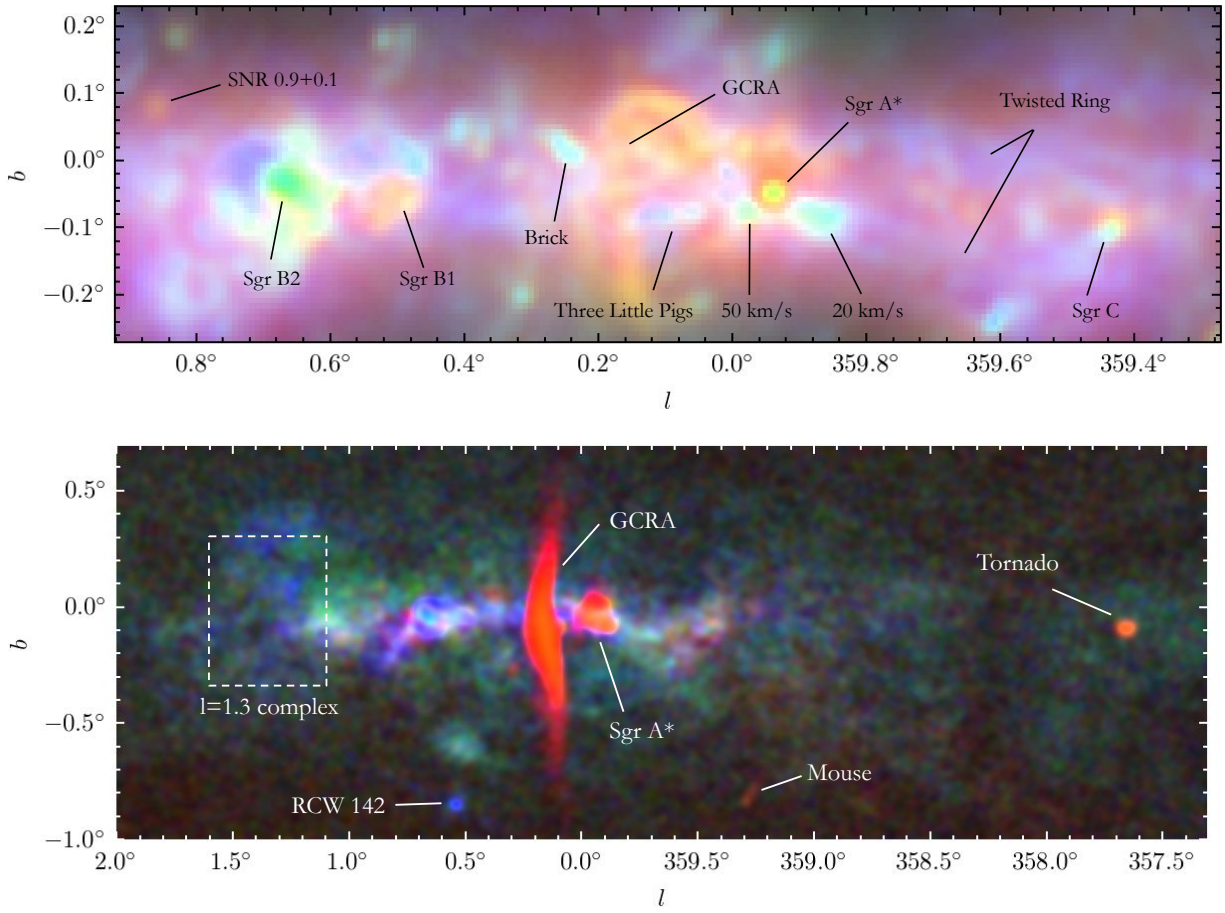

Figure 4.5: **Upper panel**: Known radio sources found in the Galactic center region. The background image shows a zoomed-in view of the multi-frequency 3-color image presented in the upper panel of Figure 4.4. **Lower panel**: Annotations of selected radio and dusty sources in the multi-frequency polarized intensity image (presented in the lower panel of Figure 4.4). The maps are smoothed with FWHM=2′ to make objects more visible.

and the Three Little Pigs (G0.145-0.086, G0.106-0.082, and G0.068-0.075; see, e.g., [120] for an overview of these molecular clouds) thus appear bright blue/green in Figure 4.5.

In general, however, the presence of strong molecular line emission in the CMZ precludes the simple interpretation that low frequencies correspond to synchrotron emission and high frequencies correspond to dust emission. Even in the relatively broad Planck and ACT passbands, line emission can dominate the total intensity in the Galactic center maps. Indeed, Ref. [169] found that 88.6 GHz HCN emission can alone account for up to 23 % of the total intensity in the Planck 100 GHz band in this region. CO(1–0) at 115.3 GHz and CO(2–1) at 230.5 GHz contribute significantly to the observed emission in the Planck 100 and 217 GHz bands, respectively [169], while other lines such as HCO^+ (89.2 GHz), CS (98.0, 147.0, and 244.9 GHz), ^{13}CO(1–0) (110.2 GHz), CN (113.2, 113.5 GHz), H_2CO (140.8 and 218.2 GHz), NO (150.2, 150.5 GHz), SiO (217.1 GHz), SO (219.9 GHz), and ^{13}CO(2–1) (220.4 GHz), among others, are also known to be present in the Galactic center (e.g., [170, 171, 172, 173, 174, 175, 176, 177]) and will contribute to the observed emission in the ACT and Planck frequency channels.

The very bright CO(1–0) emission poses a particular challenge for our analysis, as it falls comfortably within the Planck 100 GHz passband but largely outside that of ACT f090 (see Ref. [155] Figure 2). These two frequency channels have been combined without taking the differences in passbands into account, leading to CO(1–0) being emphasized on large Planck-dominated scales in the coadded map, but not on small ACT-dominated scales. This likely explains the haziness of the emission in purple in Figure 4.4, where the low-frequency channel (red) contains significant CO(1–0) emission in the Planck map but is dominated by other, less prominent emission mechanisms in the ACT map. A quantitative interpretation of the frequency spectra of particular regions in the Galactic center will therefore require careful consideration of bandpass effects, and possibly the use of external spectroscopic data (e.g., [178, 179]) and/or the CO component maps from Planck [169]. Such spectral analysis will be the subject of future work, and for now we urge caution when interpreting the colors in Figure 4.4 in terms of emission mechanisms or spectral indices.

4.5 Polarization maps

Figure 4.3 presents the full-resolution Stokes Q and U maps obtained through the map-making algorithm at each frequency band. A striking feature of the maps is the strong polarization signal of the GCRA, extending roughly from $b = -0.5°$ to $b = 0.5°$ in both f090 and f150. The signal is weaker in f220, which is dominated by polarized dust emission. Strong polarized signals can be generally seen near the CMZ along the Galactic plane across all frequency bands, with especially prominent polarization features near regions such as Sgr A* and Sgr B2. This suggests that the observed polarization signals are not dominated by diffuse emission along the line of sight (LOS), but rather by emission directly from the CMZ. Since we are focusing on high S/N regions ($\gtrsim 3$) that are negligibly impacted by debiasing, we do not debias the polarization quantities [180].

To create a three-color polarization image analogous to that in total intensity, we first compute the polarized intensity $P = \sqrt{Q^2 + U^2}$ in each band. We synthesize the three polarized intensity maps into a three-color image using f090, f150, f220 as the red, green, and blue channels respectively. The result is shown in the lower panel of Figure 4.4. The polarized emission has a strikingly different morphology than total intensity (cf. upper panel of Figure 4.4). The polarized GCRA stands out distinctively from the background in red, indicating dominance of f090, consistent with the prominence of synchrotron radiation in this region.

One quantity of interest is the polarization angle, defined as

$$\psi = \frac{1}{2} \arctan\left(\frac{U}{Q}\right). \tag{112}$$

The polarization angle is directly related to the plane-of-sky magnetic field orientation by a 90° rotation. Dust grains tend to align their short axes parallel to the magnetic field, while they radiate photons preferentially polarized parallel to their long axes. The synchrotron polarization angle, or Electric Vector Position Angle (EVPA), is similarly orthogonal to the local magnetic field orientation for optically thin emission. Hence, the magnetic field orientation is orthogonal to the polarization angle in both emission mechanisms. We note, however, that dust and synchrotron emission do not necessarily trace the same magnetic

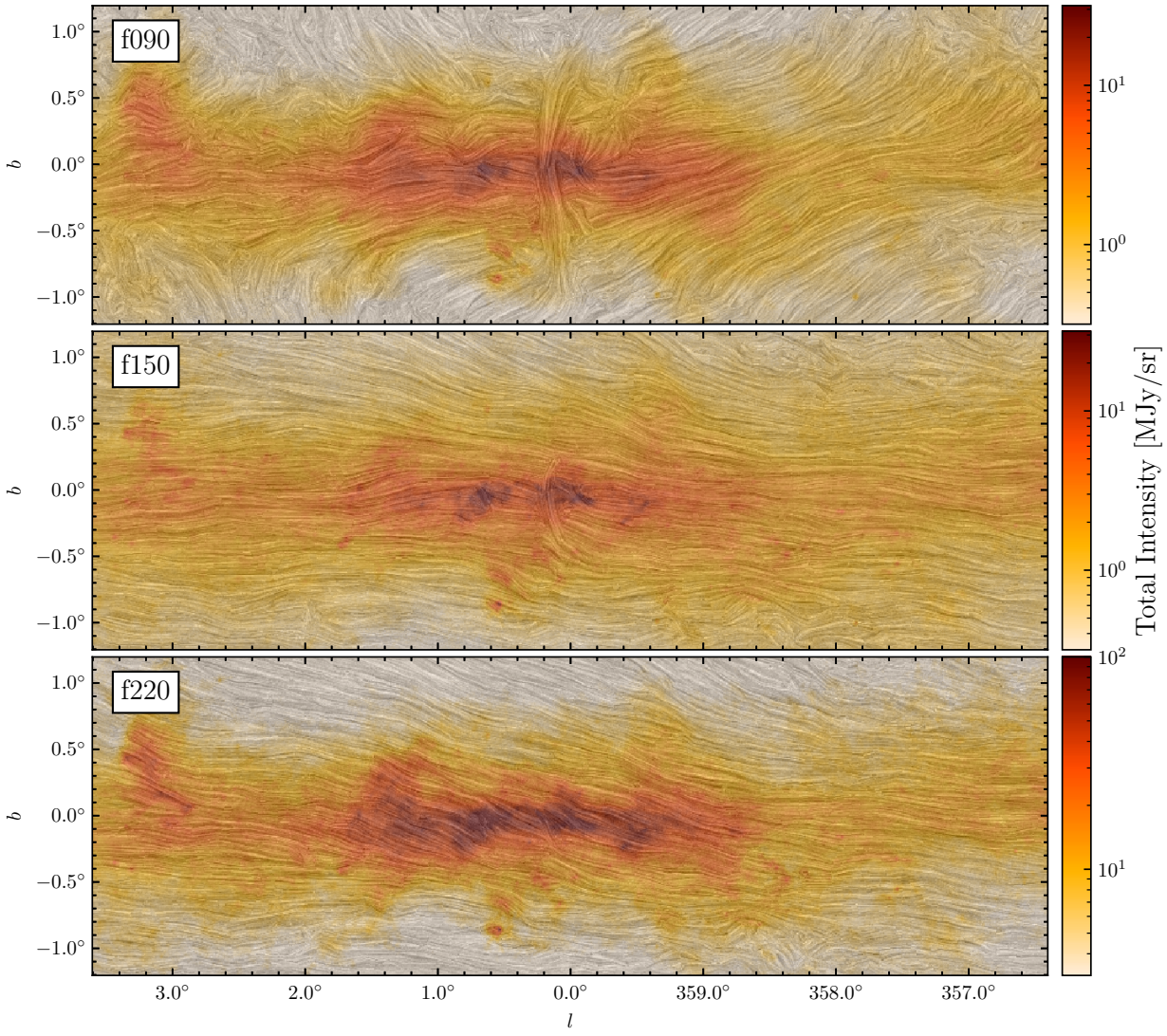

Figure 4.6: A visualization of magnetic field orientations using line-integral-convolution (LIC) with a 1° kernel. Contours in the map trace magnetic orientations. Rows represent f090, f150, and f220 respectively. Total intensity maps are shown in the background with the same color scales in Figure 4.1.

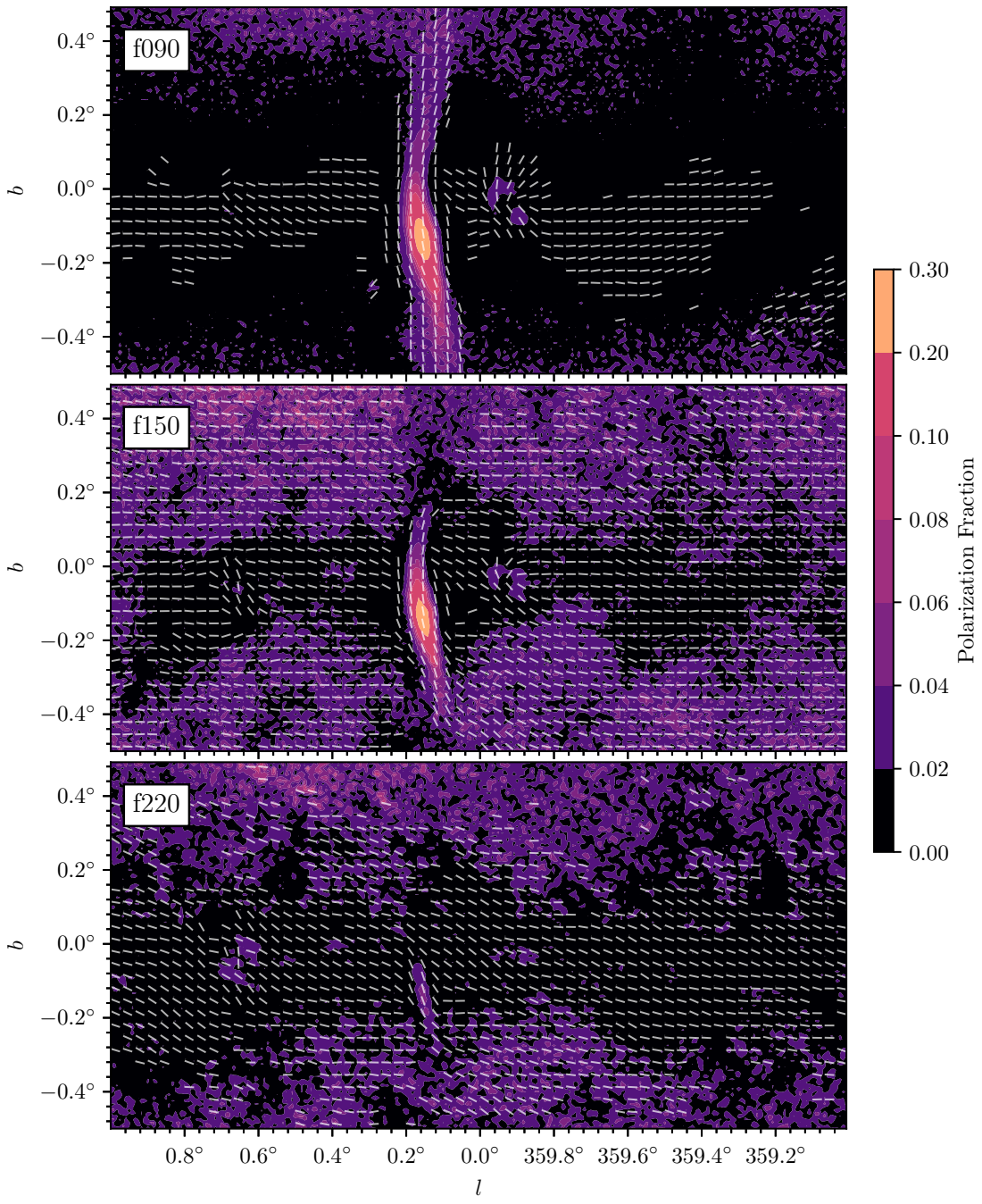

Figure 4.7: Polarization fractions (background) and magnetic field orientation (line segments) are shown for our three bands (f090, f150, and f220). To estimate the magnetic field orientations, the polarization field is smoothed with a Gaussian kernel FWHM=2′, and then resampled with a pixel size of 2′. Line segments with large uncertainty in polarization angle $\delta\psi \geq 15^\circ$ are masked.

field, as they generally probe different volumes along the LOS. The observed magnetic field morphology at a given frequency depends on the relative contribution of different emission components, which in turn depends on the spatial distribution of dust density versus cosmic ray density and the underlying magnetic field orientation and strength (see Ref. [181] for a review).

Figure 4.6 presents a visualization of the inferred magnetic field orientation in each of our bands using line integral convolution (LIC) [182] with a kernel size of 0.5°. Each contour in the map traces the magnetic field orientation. The magnetic field is approximately parallel to the Galactic plane near the CMZ for both f090 and f150, and is noticeably tilted for f220 within the range $|l| \lesssim 1.5°$. In particular, within a box of $|l| < 1.5°$, $|b| < 0.15°$ we measure the mean polarization angle to have a tilt of $\simeq 20°$ with respect to the Galactic plane, consistent with the $\simeq 22°$ tilt previously noted by, e.g., PILOT [145].

The f090 map is noticeably more disordered, with especially prominent features at the GCRA, where the plane-of-sky magnetic field is aligned with the orientation of the arc. This 90° flip in polarization angle at the GCRA has been observed by the QUIET collaboration [183] at both 43 GHz and 97 GHz. This orthogonal feature is less prominent at f150 and disappears at f220, as expected from a synchrotron-dominated signal.

The polarization fraction $p = \sqrt{Q^2 + U^2}/I$ in each band is shown in Figure 4.7. In each panel, we overlay the magnetic field orientation in the CMZ at $2'$ resolution. Along the Galactic plane the polarization fraction is generally low, $p \lesssim 2\%$. This is consistent with the previous observations from, e.g., Planck [184] and PILOT [145] that found polarization fractions at the percent level ($\lesssim 1.5\%$) in the Galactic center region. We see coherent magnetic fields even within regions of relatively low polarization fraction, in agreement with both cloud-scale observations and the relatively few wide-area dust polarization measurements, both of which tend to find very ordered magnetic fields [127, 185, 145]. The large-scale coherence in the inferred magnetic field direction suggests that the polarized emission is dominated by the CMZ. The low polarization fraction could be due to one of several effects, or to a combination of them. Perhaps the most likely is that the magnetic field orientation fluctuates both along the line of sight and within the beam smoothing radius, resulting in depolarization. There are so many emitting regions along the line of sight in the Galactic

disk that small variations in the magnetic field orientation average out in the line-of-sight integration, such that observed deviations from the mean magnetic field orientation are small. We note, however, that simulations of the Galactic magnetic field used to interpret PILOT data suggest that this effect may not be sufficient on its own to account for the entirety of the observed depolarization [145]. Another possibility is that the mean field has a significant LOS component. Because magnetically-aligned dust grains spin around their short axes, the net dust emission is more strongly polarized for regions with a predominantly plane-of-sky magnetic field than for regions where the magnetic field is more parallel to the LOS. However, a significant LOS magnetic field component would not be expected to dominate the entirety of the CMZ if the magnetic field has a significant azimuthal component. Finally, it may be that the mean field in the CMZ is itself a product of superimposed, misaligned structures that each have large scale coherence, e.g., the twisted ring geometry proposed for the distribution of dust density in the CMZ [186]. While possible, such a scenario demands great uniformity in the relative total and polarized intensities in each component to avoid dispersion in the observed polarization angles. On balance, we favor a coherent magnetic field in the CMZ dust, with LOS disorder as the primary driver of low polarization fractions, but more detailed modeling of the present data is warranted to assess the relative importance of each of these effects.

4.6 Notable objects

With arcminute resolution in three frequency bands, we detect many known radio and infrared sources, some of which have not been previously observed at ACT frequencies. Although the main focus of this chapter is presentation of the Galactic center coadded maps, in this Section we demonstrate the fidelity of these maps and their broad potential for different scientific investigations by highlighting select objects. All objects discussed in this section are marked in Figure 4.5, which includes additional selected radio sources listed in Ref. [187] and submillimeter sources from the CMZoom Survey [120] visible in our maps. This list of notable sources is non-exhaustive, and in particular, our maps extend to a wider

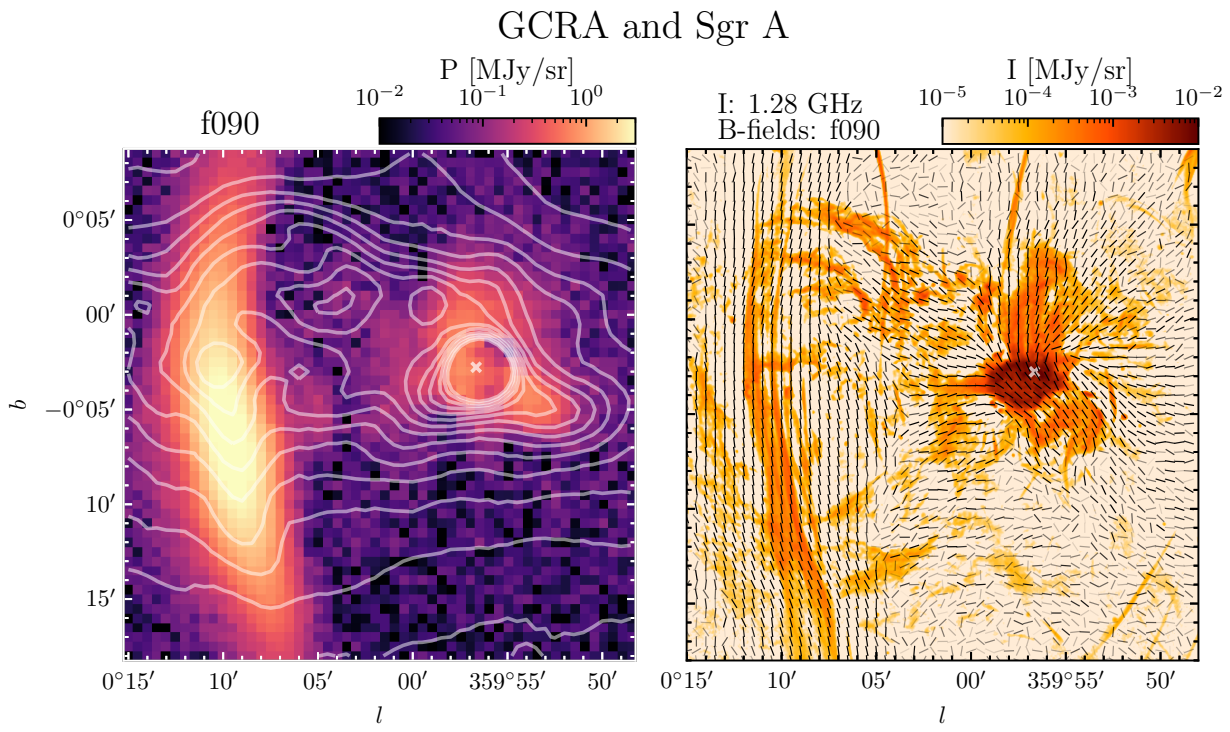

Figure 4.8: GCRA and Sgr A*. The left panel shows the polarized intensity in the region, measured from f090 coadded. Contours show levels of total intensity at f090 with a spacing of 2 MJy sr^{-1} up to 30 MJy sr^{-1}. The right panel shows the inferred magnetic field orientations from the f090 map as line segments in 0.5′ pixelization (full resolution). Segments are shown with varying opacity that scales linearly with the S/N in polarized intensity and saturates when $S/N = 3$. In the background we show a radio image of the region from MeerKAT [7] which observes at 1.28 GHz in 6″ pixelization. The expected location of Sgr A* is indicated with a white cross mark in both panels. Note that the MeerKAT image is shown for visualization purposes only, as no primary beam corrections have been applied, and the entire Galactic plane is seen through the primary beam sidelobes. Caution should be taken when interpreting the numerical values in this image (see [7] for a detailed discussion).

range in Galactic longitude than either the Ref. [187] or Ref. [120] catalogs.

4.6.1 Sgr A and GCRA

Sagittarius A (Sgr A) is a complex radio source located at the center of our Galaxy. It consists of Sgr A East, an extended non-thermal source with a radius of $\sim 3'$, and a thermal source Sgr A West, which has three-arm spiral morphology and lies within Sgr A East (e.g., [188, 189, 190]). Infrared monitoring of stellar orbits in the vicinity of Sgr A has also revealed the existence of a supermassive black hole Sgr A* that lies within Sgr A West (e.g., [191]) and acts as the dynamical center of our Galaxy [192].

The region of sky surrounding Sgr A* has been the subject of extensive multi-frequency observations both in imaging and polarimetry (e.g., [193, 194, 195, 196, 127]). Polarized observations in the millimeter bands, in particular, are important for understanding the accretion process near the black hole and associated relativistic emission (e.g., [197, 198]). Linear polarization of Sgr A* at millimeter wavelengths was first reported by the Submillimetre Common-User Bolometer Array (SCUBA) [199], which they interpret as synchrotron-dominated polarized emission sourced by the gas in the vicinity of the black hole. The observed polarization fraction of Sgr A* is $\sim 3\%$ at 2 mm. Subsequent interferometric imaging surveys (e.g., [200, 201]) measured a $\sim 2\%$ polarization fraction at 3.5 mm, and larger values at higher frequencies. Strong emission centered on Sgr A* is visible in the coadded maps, showing up clearly in the multi-frequency image with a yellow color in total intensity (see the upper panel in Figure 4.5), implying a predominance of synchrotron emission in the region. Its location indicates that the emission is likely dominated by Sgr A* itself instead of the overlapping components in Sgr A that are unresolved with the ACT beam. Regions surrounding Sgr A* are polarized at $2-4\%$ level, as seen in Figure 4.7 for f090 and f150, and show up as a reddish "blob" in the multi-frequency polarimetry (see the lower panel in Figure 4.5). This may be due to synchrotron emission from the nearby non-thermal filaments within a beam smoothing radius. The polarized emission in the vicinity of Sgr A* has a lower polarization fraction of $\sim 1.5\%$ at all three bands, consistent with the depolarization noted by SCUBA [199] at 2 mm. The slightly lower polarization fraction seen in the ACT data is

likely due to a beam depolarization effect from the larger ACT beam ($\sim 2'$) in comparison to the SCUBA beam ($\sim 34''$ at 2 mm).

In Figure 4.8 we present a zoom-in view of the region surrounding Sgr A*. The left panel shows the polarized signal in f090 overlaid with contours from the total intensity in f090. Strong emission from Sgr A* is seen in total intensity but not in polarization, where the emission is more diffuse and extends $\sim 3'$ away from the central source. This is further evidence that the polarized signal in the vicinity of Sgr A* is emitted by the surrounding non-thermal filaments, while the emission from Sgr A* itself is highly depolarized. In the right panel we show the inferred magnetic field orientations from the polarized signal at f090 overlaid on top of a radio image of the same region from MeerKAT [7], which observes at 1.28 GHz with a $6''$ beam. The magnetic field morphology inferred from our f090 map closely follows the underlying non-thermal filamentary structure. The morphology is also in broad agreement with previous Caltech Submillimeter Observatory (CSO) [127] observations at a wavelength of 350 μm with a $20''$ beam.

Figure 4.8 also shows the GCRA, a prominent radio feature located at $\sim l = 0°10'$, which consists of a bundle of thin filaments running perpendicular to the Galactic plane (e.g., [138, 190]). The GCRA is known to be a highly polarized synchrotron source, though its origin is still poorly understood. The strong synchrotron emission implies that free electrons are present in the GCRA and are accelerated to relativistic speeds in the presence of a strong magnetic field in the region. Various models have been proposed to explain the source of electrons and the acceleration mechanism (see, e.g., [202] for a review), though the matter is still under debate.

In millimeter bands, the GCRA has previously been detected at 7 mm [203], 3 mm [175], and 2 mm [204], which the latter notes was the highest-frequency detection of the GCRA at the time. Polarized emission from the GCRA has also been previously detected at 2 and 3 mm by Ref. [205], and at 3 mm and 7 mm by Ref. [183]. In our coadded maps, GCRA appears in total intensity in both f090 and f150. The associated polarized emission can also be seen clearly in f090 and f150 with polarization fractions reaching $\sim 30\%$. This is considerably higher than the $\sim 10\%$ peak polarization noted by the QUaD Galactic Plane Survey [205] at the same frequencies, likely due to the improved angular resolution in our

coadded maps (2′ at f090, 1.4′ at f150) in comparison to Ref. [205] (5′ at 100 GHz, 3.5′ at 150 GHz). The polarized emission from the southern portion of the GCRA is also visible in f220, which is likely the highest frequency at which this structure is detected to date (note especially the f220 Q map in Figure 4.3). In addition to being fainter at 220 GHz on account of the falling synchrotron spectrum, the GCRA is also obscured by emission from dust along the line of sight. The uniformity of the polarized emission observed in the Arc as seen in Figure 4.3 implies that a highly ordered magnetic field exists along the Arc that deviates sharply from the large scale magnetic field geometry (see Figure 4.6). In particular, the magnetic field orientation inferred from f090 (as seen in the right panel of Figure 4.8) aligns closely with the filamentary structure perpendicular to the Galactic plane. This is in broad agreement with the morphology observed at 43 GHz and 96 GHz by QUIET with lower angular resolution [183].

4.6.2 The brick

G0.253+0.016, also known as "the Brick", is a dense, massive molecular cloud in the CMZ, and a prominent infrared dark cloud [206, 167]. In the context of understanding the low star formation rate in the Galactic center environment, the Brick is a particularly interesting case study. Despite its high mass ($> 10^5 M_\odot$) and density ($> 10^4$ cm^{-3}), evidence of star formation is nearly absent in the Brick, and thus it may provide an ideal opportunity to study the initial conditions of high-mass star formation [207, 167, 208, 209, 210]. A number of factors have been invoked to explain the dearth of star formation in G0.253+0.016, including solenoidal turbulence driven by strong shear in the CMZ [211, 212, 213, 214], or strong cloud scale magnetic fields [$B \sim$ mG, 185].

The Brick stands out at high contrast to the background in the coadded total intensity maps at both 150 and 220 GHz. Our polarization measurements at these frequencies probe the magnetic field structure in the dust toward G0.253+0.016 at ∼arcminute scales. These observations complement 20″ resolution polarization data at 350 μm from the CSO [215, 185]. We find that the inferred magnetic field orientation is aligned parallel to the long axis of the Brick on the plane of the sky (Figure 4.9), and the polarization angles are very ordered in this

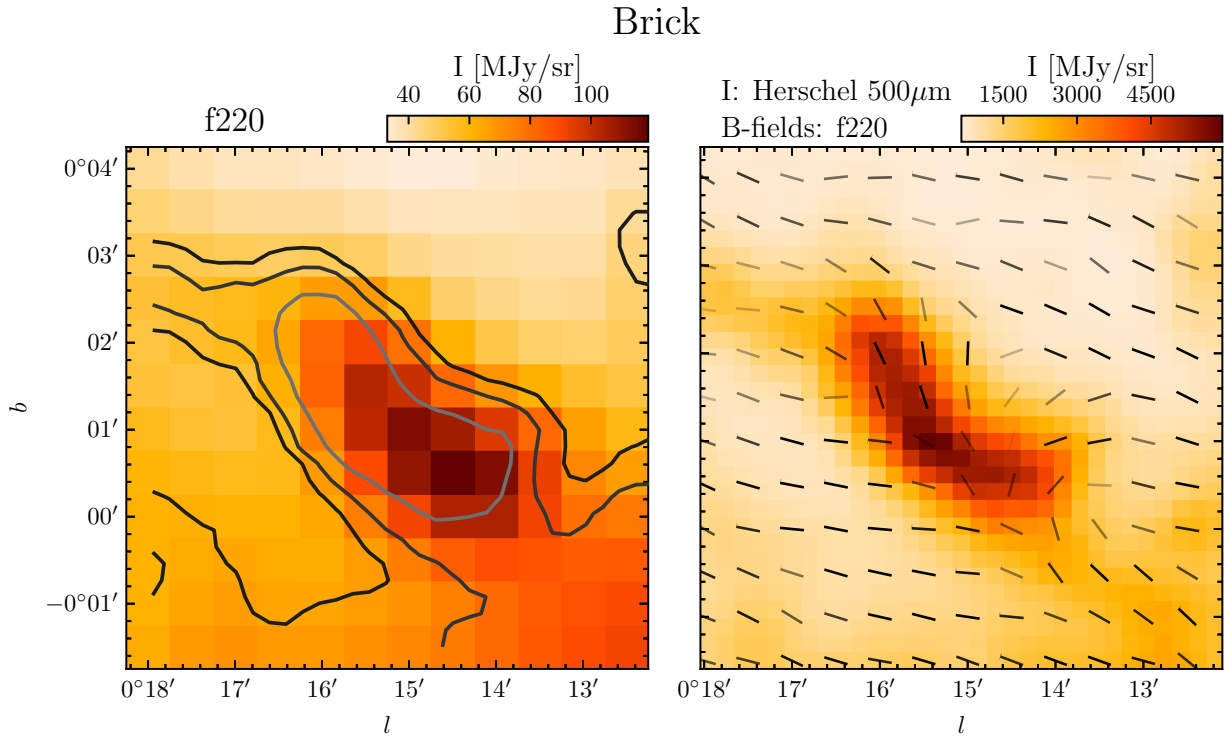

Figure 4.9: Molecular cloud known as "the Brick". **Left:** total intensity measured from ACT+Planck f220 coadd map is plotted in the background. The Herschel 500 μm measurements [8] are shown as contours indicating 50th, 70th, and 90th percentiles from lighter to darker contours. **Right:** total intensity measured by Herschel 500 μm is shown in the background. We show the magnetic field orientation inferred from the f220 map as line segments. Segments are shown with varying opacity that scales linearly with the S/N in polarized intensity and saturates when $S/N = 3$.

region, in agreement with the CSO data at smaller angular scales. Ref. [185] uses the strong coherence of the magnetic field orientation in the Brick to compare the inferred magnetic field strength to the gas velocity dispersion measured from N_2H^+ emission [208]. Those authors find that magnetic fields dominate over turbulence in the Brick. The coherent magnetic field structure in our observations is consistent with the expectation that turbulence in the Brick is sub-Alfvénic at the scales probed by ACT. The ACT polarized emission is brightest at the northern part of the Brick, with a peak polarization fraction of 3.6%. The polarized intensity is lower in the southern portion of the cloud, and the SNR on the polarized intensity drops below 3. This depolarization may be due in part to unresolved polarization structure within the ACT beam, and/or to incoherent contributions to the polarized emission along the line of sight.

4.6.3 The three little pigs

The cloud triad G0.145-0.086, G0.106-0.082, and G0.068-0.075 visible in Figure 4.10 has been dubbed "the Three Little Pigs." All three clouds have been noted as a set of compact dusty sources in the CMZoom Survey [120], while G0.068-0.075 also appears in the SCUBA-2 Compact Source Catalog [216]. As Figure 4.10 illustrates, each cloud is also apparent in the 500 μm data from Herschel Infrared Galactic Plane Survey Herschel (Hi-GAL) [8]. Interestingly, the 3″ resolution 230 GHz observations with the Submillimeter Array as part of the CMZoom Survey have revealed a dearth of substructure in G0.145-0.086 ("Straw Cloud"), somewhat more substructure in G0.106-0.082 ("Sticks Cloud"), and yet more in G0.068-0.075 ("Stone Cloud").

ACT f220 measurements give a first look at the magnetic field geometry in these clouds at arcminute resolution. The Straw Cloud, perhaps owing to a lower column density or lack of dense substructure, has a magnetic field orientation that deviates little from the large scale field structure. In contrast, both the Sticks and Stone Clouds have polarization angles in their interiors that are highly misaligned with the large scale magnetic field. Similar to the depolarization observed toward the Brick, the cancellation of polarized emission from dust in different regions within the cloud and/or other dust along the line of sight may explain

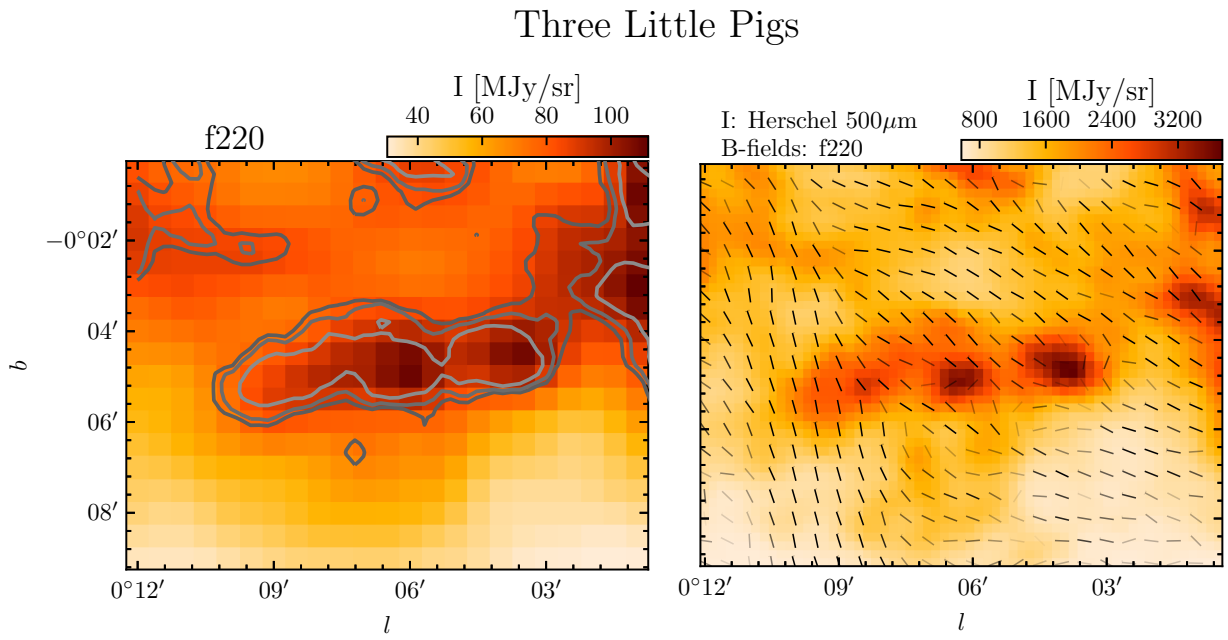

Figure 4.10: A cloud triad known as "the Three Little Pigs" consisting of G0.145-0.086 ("Straw Cloud"), G0.106-0.082 ("Sticks Cloud"), and G0.068-0.075 ("Stone Cloud"). The data are plotted following Figure 4.9, with the left panel showing the ACT+Planck f220 map with the Herschel 500 μm image overlaid as contours (indicating 50th, 70th, and 90th percentiles from lighter to darker colors), and the right panel showing the Herschel 500 μm map with the magnetic field orientations inferred from the f220 map overlaid as line segments. Segments are shown with varying opacity that scales linearly with the S/N in polarized intensity and saturates when S/N = 3.

the low polarized intensities observed, particularly in the Stone Cloud.

4.6.4 The mouse

G359.23–0.82, also known as "the Mouse", is a pulsar wind nebula powered by the young X-ray source PSR J1747–2958 [217, 218]. G359.23–0.82 was originally discovered in radio continuum data from the Very Large Array (VLA), and derives its nickname from its bright compact nebula "head" and extended radio "tail" [219]. The Mouse is strongly linearly polarized at centimeter wavelengths [220]. Distances to PSR J1747–2958 and the Mouse are uncertain, but they are not at the Galactic center: observations of neutral hydrogen absorption set the maximum distance to G359.23–0.82 at ~ 5.5 kpc [221]. Ref. [222] argue for a distance of $\sim 5\,\mathrm{kpc}$, a value now commonly adopted [e.g., 223]. At 5 kpc, the transverse velocity of PSR J1747–2958 is $306 \pm 43\,\mathrm{km\,s^{-1}}$ [224]. The Mouse is a striking example of a bow shock nebula, formed by the interaction of the pulsar with the ambient ISM as it travels at supersonic speeds (e.g., [166]).

The Mouse is a prominent object in the ACT f090 map, both in total and polarized intensity (Figure 4.11). In particular, polarized emission is detected significantly across the peak of the Mouse, which is expected for a pulsar wind nebula. Significant polarized emission is also detected along its tail, and exhibits a similar morphology as seen by MeerKAT at 1.28 GHz [7] with a $6''$ beam, albeit at lower resolution in the ACT data. The implied magnetic field orientation in the f090 band is roughly parallel to the Mouse's extended tail, consistent with observations at 3.5 and 6 cm by the VLA [220]. The Mouse is traveling eastward in declination, which is roughly toward the lower lefthand corner of Figure 4.11.

4.6.5 The tornado

G357.7-0.1, "the Tornado," is typically classified as a supernova remnant, though its unusual properties have prevented a definitive explanation [225, 226]. The Tornado has been long observed in radio imaging and polarimetry (e.g., [162, 227, 228]), which consistently show a bright "head" region and a "tail" region roughly $10'$ in extent. Recently, mid- and far-infrared dust emission has been detected with Spitzer and Herschel, revealing a large dust

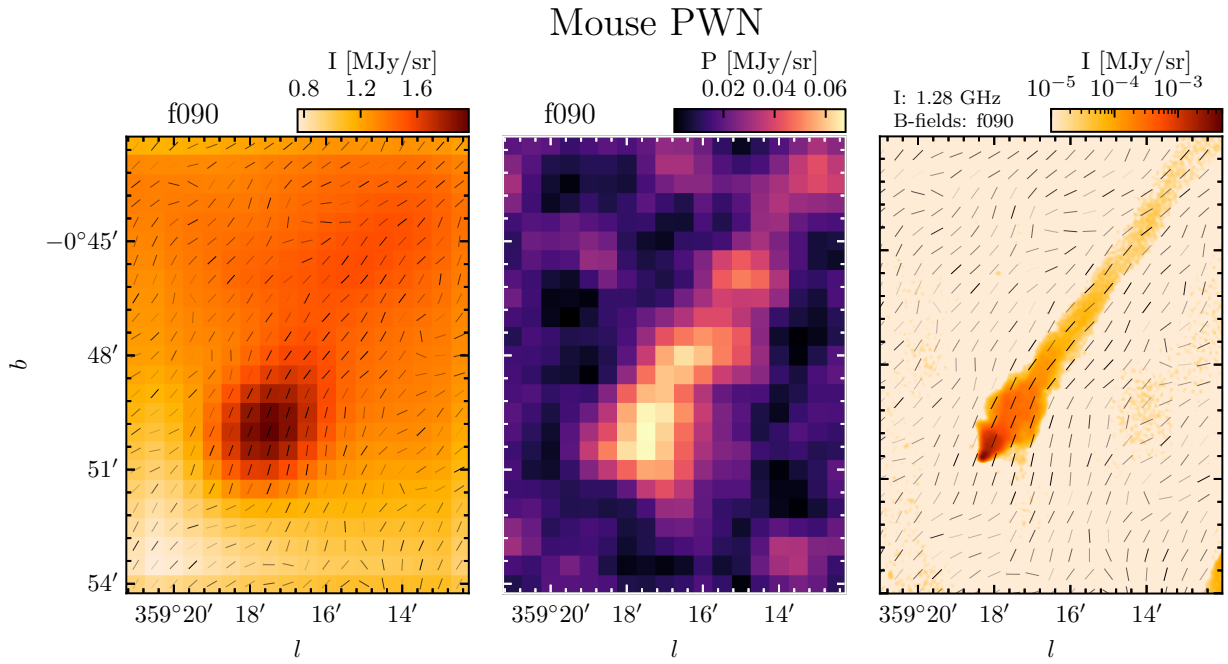

Figure 4.11: G359.23–0.82 or "the Mouse" is a pulsar wind nebula (PWN) traveling with high velocity ($\sim$300 km s^{-1}) with respect to ISM, causing a comet-like tail. The left panel shows the total intensity in f090 with magnetic field orientation over-plotted in line segments. Both the background and magnetic field are smoothed to a resolution of 2.2′ to increase the signal-to-noise ratio. Segments are shown with varying opacity that scales linearly with the S/N in polarized intensity and saturates when S/N= 3. The middle panel shows the polarized intensity in f090 after smoothed to a resolution of 2.2′. The right panel shows a radio image of the region from MeerKAT [7] which observes at 1.28 GHz in 6″ pixelization, with the magnetic field orientation from f090 over-plotted as line segments similar to the leftmost panel.

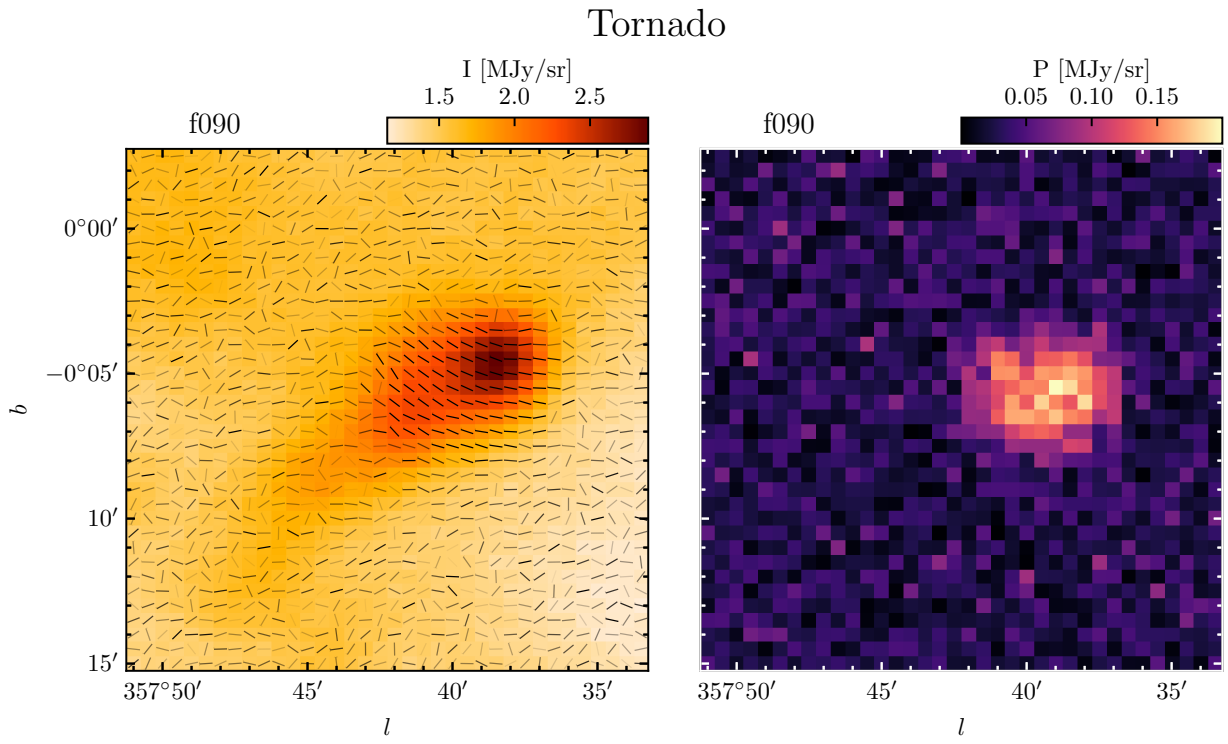

Figure 4.12: G357.7-0.1, or "the Tornado", is typically classified as a supernova remnant. The left plot shows the total intensity in its neighborhood in f090 coadded map. Line segments indicate The right plot shows the magnetic field orientations inferred from f090. They are shown with varying opacity that scales linearly with the S/N in polarized intensity and saturates when S/N= 3. The right panel shows the corresponding polarized intensity map in f090. Both maps are shown at the full resolution from mapmaking (0.5′).

reservoir in the head region ($\sim 17\,M_\odot$) and consistent with interstellar matter swept up in a supernova blast wave [226]. The head of the Tornado has also been detected by Chandra in X-rays without evidence for embedded point sources [225], lending further credence to its classification as a supernova remnant. However, the provenance of the tail is still unresolved (see [226] for a recent discussion).

The Tornado is prominent in the f090 and f150 Stokes Q and U maps, but not f220 (see Figure 4.3). Likewise, the region stands out in reddish-brown in the three-color polarization map (Figure 4.5). This suggests the prominence of synchrotron emission in this source. A closer examination of the Tornado in the f090 band is presented in Figure 4.12. Here we see the extended tail region in total intensity but not in polarization, while the head is prominent in both. This morphology is consistent with 4.9 GHz polarimetric observations by Ref. [227]. The inferred magnetic field at f090 is approximately perpendicular to the extended tail in the eastern side of the Tornado, and is tilted towards the head on the western side. This is also in a broad agreement with the magnetic field morphology noted by Ref. [227] at 4.9 GHz. We observe a maximum polarization fraction of the Tornado in f090 of $8.5\% \pm 1\%$, slightly lower than the $\sim 10\%$ observed at 4.9 GHz at significantly higher resolution ($12 \times 26''$ beam) [227]. It is likely that much of the difference is due to more beam depolarization in the ACT data.

4.6.6 $l = 1.3$ complex

The combination of ACT and Planck data used in the coadded maps enables large regions to be mapped with fidelity on both large and small angular scales. Likewise, the high sensitivity of the polarimetry permits mapping of more diffuse regions of molecular clouds, not just bright cores. These capabilities are highlighted in the $20 \times 30'$ maps of the $l = 1.3$ complex in Figure 4.13.

The $l = 1.3$ complex is a large, high-velocity-dispersion molecular cloud complex extending from roughly 1.2–1.6° in Galactic longitude [229]. The elevated abundance of SiO and high ratio of CO(3–2) to CO(1–0) emission in some clouds within the complex suggest the presence of strong shocks, perhaps from cloud-cloud collisions or supernova explosions

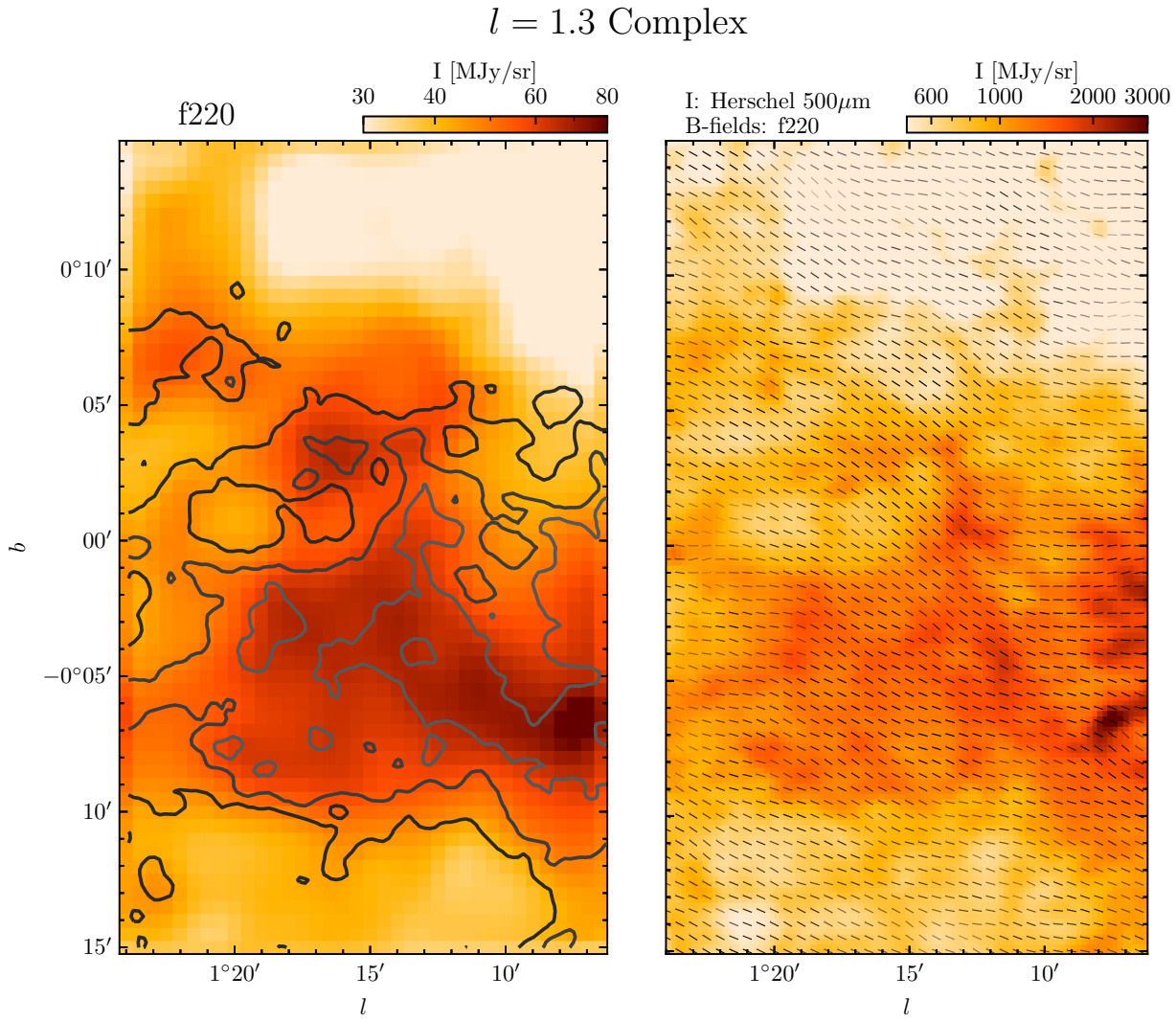

Figure 4.13: $l = 1.3$ molecular complex. The left plot shows the total intensity in f220 (smoothed with FWHM=1′) with contours indicating the 50th, 70th, 90th percentiles in the Herschel 500 μm map. The right plot shows the Herschel 500 μm map with magnetic field orientation inferred from the f220 map as an overlay, after smoothed to a resolution of 1.4′. Segments are shown with varying opacity that scales linearly with the S/N in polarized intensity and saturates when S/N= 3.

[230, 231, 232, 233, 216, 234]. This complex may sit at the intersection of a dust lane with the nuclear ring, supplying it with material [230, 235, 232, 236].

Total emission from the $l = 1.3$ in f220 and Herschel 500 μm [8] is presented in Figure 4.13, with good morphological correspondence between the two maps. In the right panel, we overlay the f220 magnetic field orientation on the higher resolution Herschel map. While many density structures show clear alignment with the magnetic field orientation, this is not universally observed. The highest intensity regions have comparatively low polarized intensities, suggesting elevated magnetic field disorder or a loss of grain alignment in the densest regions.

4.7 Conclusion

We have presented new arcminute-resolution maps of the Galactic center region at microwave frequencies by combining data from ACT and Planck. Known radio features appear at high significance in both total intensity and polarization in three frequency bands. The polarization maps provide a frequency-dependent probe of magnetic fields, demonstrating a change in the observed magnetic field morphology as the fractional contributions of synchrotron radiation and thermal dust emission from different regions within the Galactic center along the line of sight vary with frequency. With wide-field maps at higher angular resolution, we identified known radio sources and molecular clouds, some of which have not previously been observed in polarization at microwave frequencies. With three frequency bands, our total intensity maps reveal the rich physical environment in the CMZ with spatially varying combinations of different emission mechanisms, including synchrotron, free-free, dust, and molecular line emission in the CMZ. Separation of these emission components will be the subject of a follow-up work.

The coadded maps produced in this work is made publicly available on LAMBDA. These maps are suitable for tracing magnetic field morphology across the Galactic center region and measuring the total and polarized emission from individual sources. However, caution is urged for multi-frequency analyses due to the bandpass mismatch between ACT and

Planck that results in a slight scale-dependence of effective band centers for different emission mechanisms. As discussed in Section 4.4, CO(1-0) emission falls within the Planck 100 GHz passband but not f090, amplifying bandpass mismatch effects in the resulting coadded map.

ACT has continued to observe the Galactic center during 2020, collecting a similar amount of data to that used in this work. In addition, the daytime data from both 2019 and 2020 can, in principle, be corrected for thermal telescope distortions [98], which would again double the total amount of data. Therefore, ACT maps with half the pixel noise variance of those presented here are possible based solely on data that has already been collected. Additionally, we plan to apply the mapping techniques used here to approximately 70 degrees of the Galactic plane covered by ACT from 2019 and 2020. Furthermore, the addition of the low-frequency array to ACT in 2020 [237, 238] will also allow us to map the Galactic plane at 27 GHz and 39 GHz, likely yielding new insights on the Galactic center environment.

The next observational step at these frequencies will be the Large Aperture Telescope of the Simons Observatory [30], anticipated to see first light in 2023 from the same site in Chile. This new instrument will have the same 6-meter diameter primary as ACT, but with an instrumented focal plane of 5 times larger area [239]. The nominal scan strategy will continuously cover the entire sky in the declination range between $+25^\circ$ and -40°, providing coverage of over 100 degrees of the Galactic plane in five frequency bands in both total intensity and polarization. The five-year map noise should improve on ACT by roughly a factor of three. The Galactic center will be observed at higher frequencies by the CCAT-prime project [240] and will also be a good target for future balloon-borne instruments, which can achieve sub-arcminute resolution with similar sensitivity at even higher frequencies, e.g., BLAST Observatory [241]. By 2030, we can also anticipate data from CMB-S4 [33], with an additional map noise improvement by a factor of four. This unrivaled combination of resolution, sky coverage, and sensitivity at microwave frequencies will enable many new inquiries into the properties of the Milky Way.

5.0 Data cuts for the Atacama Cosmology Telescope

Having discussed the applications of high precision CMB measurements, in this chapter I focus instead on the experimental front. In particular, I describe one of the crucial steps in the data reduction pipeline in ACT known as the data cuts pipeline which identifies data affected by sporadic pathologies and removes them from the CMB mapmaking process. Cleaning observed data from such pathologies is a challenging task due to the large data volume and the often complex phenomenology associated. As data cuts impact the noise property of the data, generating a high quality data cuts product has direct impact on the precision of the final science products. The current data cuts pipeline used in ACT was originally implemented by Rolando Dünner [242], which was then improved by Loïc Maurin and further refined by me. I am currently the primary person responsible for generating and characterizing the data cuts, and refining the cuts pipeline for data collected by ACT from 2017 onward. This work directly impacts the quality of the CMB maps in the next ACT data release (DR6), which is expected to contain a factor of 5 more data than the previous ACT data release (DR4). As the DR6 analysis is still underway, I present only preliminary results based on the current status of the analysis.

5.1 Introduction

Over the past 30 years, precision measurements of the Cosmic Microwave Background (CMB) have led to remarkable progress in our understanding of cosmology. The result has led to a remarkably simple model of our universe known as the standard model of cosmology, which can be described simply with six parameters. Most of the parameters are determined with percent-level accuracy with the help of high precision CMB measurements (e.g., [1]). This remarkable progress is enabled by the successive generations of CMB experiments with increasing sensitivity. Space-based CMB experiments such as the Wilkinson Microwave Anisotropy Probe (WMAP) [148] and Planck [243] are able to map the full CMB sky across

multiple frequencies. In particular, WMAP obtained cosmic-variance-limited measurements of the primary anisotropies of the CMB for multipoles $L \lesssim 500$. It was followed-up by the Planck satellite mission with an improved sensitivity, which obtained cosmic-variance-limited measurements of CMB anisotropies up to multipole $L \lesssim 1200$, leading to many of our best known constraints on cosmological parameters to date, with percent-level accuracy [1].

On the other hand, due to the engineering constraint of space-based experiments, the angular resolution of Planck is limited to $\gtrsim 5'$. This means that the small-scale CMB anisotropies are inaccessible to Planck. In fact, many physical effects leave imprints in the small-scale CMB anisotropies, such as the thermal Sunyaev Zel'dovich effect and the kinetic Sunyaev Zel'dovich effect, which are important for our understanding of the late-time universe [244]. Planck also has limited sensitivity in polarization measurements, while CMB is known to be polarized at $\sim 10\%$ level, and measurements of CMB polarization provide an important independent probe of the recombination physics, potentially yielding even higher constraining power in cosmological parameters than temperature maps [245].

Ground-based CMB experiments such as the Atacama Cosmology Telescope (ACT) and South-pole Telescope (SPT), on the other hand, have significantly improved their map sensitivity over the past decade. In particular, ACT now maps over 40% of the CMB sky with arcminute resolution and improved sensitivity in both temperature and polarization. The CMB polarization map obtained by ACT is signal-dominated, and the improved angular resolution also makes small-scale physics accessible. Hence, ground-based CMB experiments like ACT will likely be the next big step in our understanding of cosmology.

ACT released its Data Release 4 (DR4) maps in 2020, containing observations made between observational season 2013 and 2016 [98]. The released map, when combined with data from WMAP, has lead to competitive constraints on cosmological parameters such as H_0, independently of Planck, shedding light on the Hubble's tension (see, e.g., [10] for a review). The next major data release in ACT will be Data Release 6 (DR6). It will contain data collected between observational season 2017 and 2019, which has 5 times larger data volume than the previous data releases. It will allow ACT to constrain cosmological models with its data alone, independently of Planck, to an competitive or better precision than Planck, significantly improving our current understanding of cosmology.

The observational data that will be used for ACT DR6 is currently being characterized and preprocessed. One of the crucial steps in this process is known as data cuts, which involves identifying data with known pathological problems, such as data collected by defective detectors and/or affected by bad weather conditions. Data cuts pipeline has direct impact on the quality of the final CMB maps and the precision of the derived cosmological constraints. Hence, optimizing the data cuts algorithm is crucial for the success of CMB experiments.

In this chapter we describe the data cuts algorithm used for the upcoming ACT DR6. The chapter will be organized as follows. In Section 5.2 we give an overview of instrument details of the telescope and discuss the property of the observation data. We describe the main data cuts pipeline in Section 5.3, and show some early results from the pipeline for ACT DR6 in Section 5.4. We discuss future outlook of the current data cuts algorithm in light of the upcoming CMB experiments including the challenges and alternative solutions in Section 5.5, and we conclude in Section 5.6.

5.2 The Atacama cosmology telescope

5.2.1 Overview of observational data

The Atacama Cosmology Telescope (ACT) is a Gregorian telescope with a 6 m primary mirror and a 2 m secondary mirror. It is located in the Atacama Desert in Chile at an altitude of 5190 m above the sea level [147, 84]. ACT observes the millimeter sky across different frequencies from 30 GHz to 220 GHz, in both temperature and polarization. In particular, three Advanced ACT dichroic detector arrays (PA4, PA5, PA6) [150, 151, 152], were used between observational season 2017 and season 2019 (which we denote as s17, s18, s19), collecting data at three frequency bands 90 GHz, 150 GHz, and 220 GHz, termed as f090, f150, and f220 respectively hereafter. Each detector array contains $\sim$ 2000 Transition Edge Sensor (TES) detectors sensitive to two frequency bands sensitive and two linear polarizations (as summarized in Table 5.1). The entire detector array is kept at a temperature of $\sim 100\,\mathrm{mK}$

to ensure that the TES detectors are at superconducting transition. Detectors within an array are arranged in rows and columns – detectors at the same column share the same biasing circuit, which is used to keep detectors at superconducting transition, and detectors at the same row share the same read-out circuit. This is relevant for our discussion as many instrumental effects tend to manifest in row / column space.

`array`	`frequencies`	N_{dets}
PA4	f150, f220	2048
PA5	f090, f150	1760
PA6	f090, f150	1760

Table 5.1: Frequency bands that each detector array observes at and the number of detectors (N_{dets}) in each detector array.

As the sky drifts across the telescope, ACT scans the sky periodically in an azimuthal motion at a fixed elevation. In addition, ACT acquires data at a rate of 400 Hz, and the data is then stored to disk in the form of time-ordered data (TOD). Each stored TOD contains measurements from all detectors of an array within an interval of ~ 10 minutes (see Figure 5.1 for an example TOD). Between observational season 2017 and 2019, a total of $\sim 2 \times 10^5$ TODs were collected, which are the main subject of the upcoming ACT DR6 and hence the subject of this analysis.

5.2.2 Mapmaking

TODs can be projected into a sky map by solving the mapmaking equation,

$$d_i(t) = P_{i,p}(t) m_p + n_i(t), \tag{113}$$

where $d_i(t)$ denotes the TOD of a given detector i at time t, m_p denotes a pixelated sky map with pixel index p, $P_{i,p}(t)$ is known as the pointing matrix which denotes where in the sky a given detector i is measuring at time t, and $n_i(t)$ represents detector noise. Equation 113

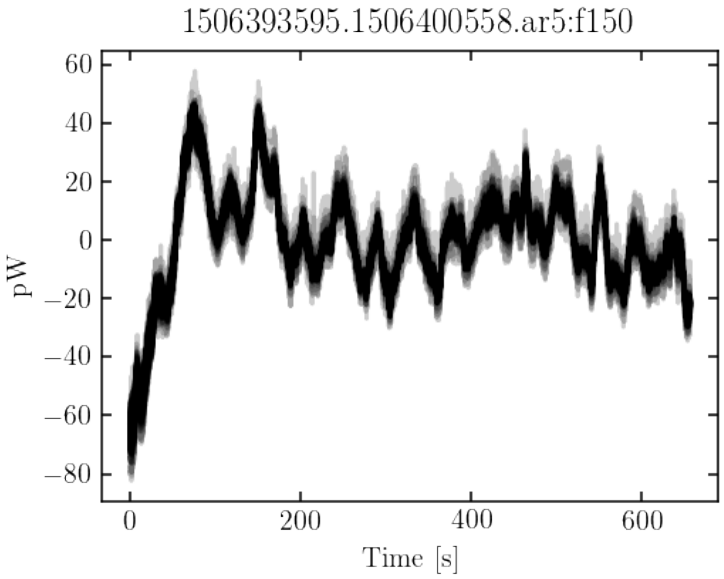

Figure 5.1: An example TOD obtained from PA5 at f150 in observational season 2017 after calibration. Timestreams from multiple detectors are over-plotted with transparency.

can be inverted using a maximum-likelihood method to obtain a sky map m_p from TODs $d_i(t)$, by solving

$$(P^T N^{-1} P)m = P^T N^{-1} d, \tag{114}$$

where we have dropped the detector, pixel, and time indices for brevity. N denotes the detector-detector noise covariance matrix, which is often referred to as the noise model.

From Equation 114 it is apparent that the quality of sky map depends critically on two aspects: (1) to what extent is the observation data $d_i(t)$ an accurate measurement of the sky. For example, when a detector is severely contaminated by the thermal emission from the ground, Equation 113 is no longer an accurate description of the data. Equation 113 also assumes that data from different detectors are properly calibrated. A mis-calibration error may lead to leakages of signal into the noise model, potentially biasing the resulting map and leaking temperature signal into polarization; (2) how accurately is the noise model N capturing the time varying noise covariance between different detectors. For example, the existence of short-duration glitches, such as those caused by the read-out circuit and cosmic

rays, may bias the noise model, because a time-domain glitch will manifest as a non-local bias in the Fourier space, which is where ACT builds the noise model. Hence, to improve the quality of map, a preprocessing pipeline is needed to identify and remove data with known pathological conditions, such as glitches, before going into mapmaking. This is the motivation behind the data cuts pipeline.

5.2.3 Source of noises

Noise in the observed data is contributed by many sources, among which the dominant contribution comes from the atmospheric emission, which can be 3-4 orders of magnitudes higher than the expected CMB signal. The atmosphere emission can be modeled as a gray body. In the Rayleigh–Jeans limit,

$$I_{\rm atm}(\lambda) = \frac{2k_B T_{\rm atm}}{\lambda^2}\left(1 - e^{-\tau A}\right), \tag{115}$$

where $T_{\rm atm}$ is the temperature of atmosphere, k_B is the Boltzmann's constant, λ is the wavelength of observation, τ is the optical depth, and A is the air mass. The factor $e^{-\tau A}$ represents the atmospheric transmission, which depends on the amount of precipitable water vapor (PWV) in the atmosphere. Figure 5.2 shows how brightness temperature of the atmosphere, defined as $T_b \equiv T_{\rm atm}(1 - e^{-\tau A})$, changes with frequency and PWV. It shows that the higher ACT frequency bands (f150, f220) are more sensitive to PWV than the f090 band.

The observed data is also affected by thermal drifts caused by temperature changes in the cryostat used to keep the detector at low temperature. Thermal drift is often the second strongest contribution to the observed data after the atmospheric noises, but it can become the dominant contribution during excellent weather condition particularly at lower frequency band (e.g., f090) that has a higher atmospheric transmittance. Figure 5.3 shows an example detector TOD with its signal dominated by thermal fluctuation in the array.

Both atmospheric and thermal drifts fluctuate on the time scales of $\gtrsim 1$ seconds. Hence they dominate the low frequency part of the power spectrum of a TOD, with a $1/f$ power law in frequency, as seen in Figure 5.4. Another type of noise is random noise sourced by,

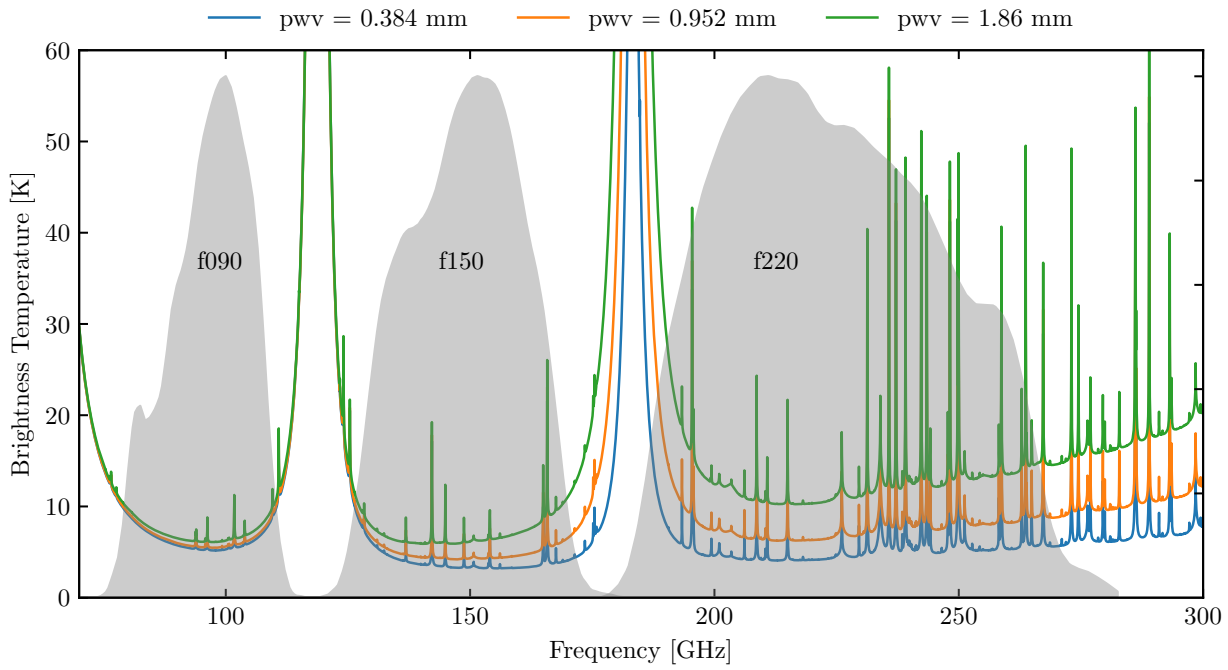

Figure 5.2: Brightness temperatures of the atmosphere at different PWVs are shown in solid curves, generated using `am` atmospheric modeling software [9]. The shaded area shows the ACT passbands at f090, f150, and f220, respectively.

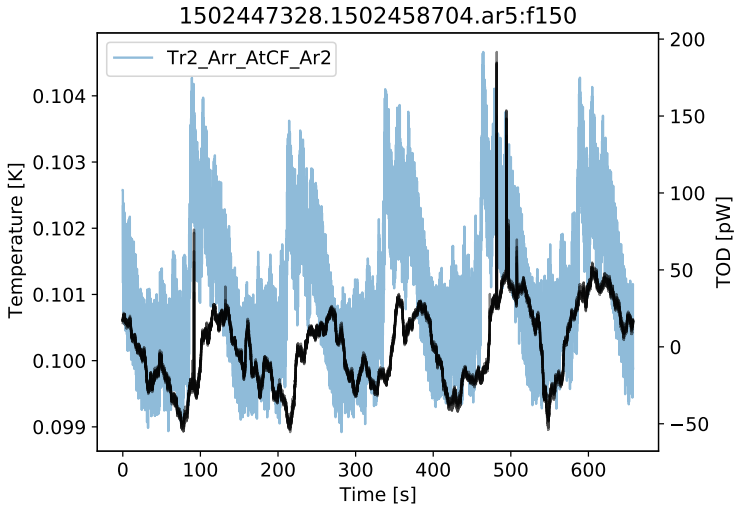

Figure 5.3: An example detector TOD (black) is over-plotted with the thermometer readings (blue) from Tr2_Arr_AtCF_Ar2 located in the same array. It shows that a TOD signal can be significantly affected by thermal drifts caused by temperature changes on the detector array.

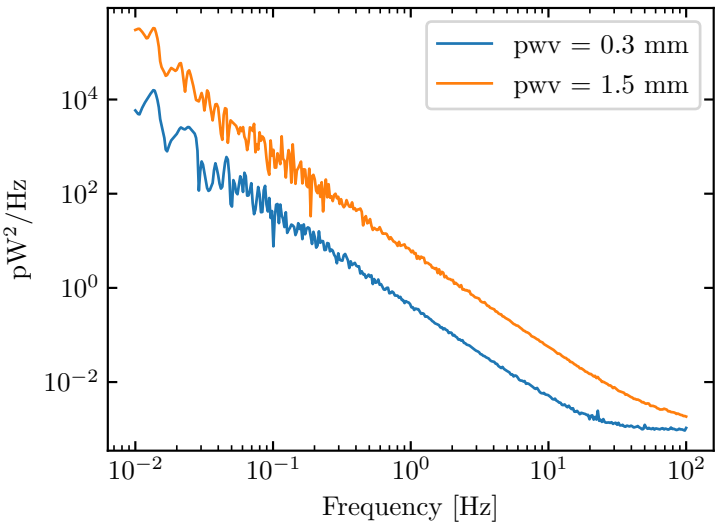

Figure 5.4: Noise power spectrum of a given detector at two different PWVs. Frequencies are binned logarithmically to reduce fluctuations.

e.g., photon shot noise and read-out circuit noise. This type of noise tends to have a white spectrum which dominates the high frequency part of a TOD power spectrum, and it tends to be uncorrelated across different detectors.

Detectors may experience sporadic pathologies which make the detector TODs unusable for mapmaking. Pathological problems can occur on a variety of time scales. On the 0.01 s scale, detectors are impacted by glitches from, e.g., read-out circuits and cosmic ray hits. They typically show up as spikes a few times higher than the typical noise level of the detector. Examples of such glitch can be seen in the TOD in Figure 5.3 as spikes. On the 0.1 s scale, signals from point sources, such as planets in the solar system, may dominate the TOD signal when a detector scans across them. This leads to a spike that looks like a glitch but differs in duration and signal shape. The most significant difference between a glitch and point source signal is that point source signal tends to move across the array as the telescope scans across the array, while a glitch tends to be localized to with a few detectors. On the 1 s scale, instrumental effects start to be apparent, such as mechanical vibrations, thermal oscillations caused by periodic changes of thermal bath temperature, and scan-synchronous signals caused by the scan, all of which may dominate the observed signal of a TOD. Detectors affected by these pathological problems need to be identified prior to mapmaking to improve the quality of the final maps. This is the main objective of the data cuts pipeline, which we describe in detail in the next section.

5.3 Data cuts pipeline

5.3.1 Overview

The data cuts pipeline looks through all TODs and generates three classes of cuts: per-sample cuts, per-detector cuts, and per-TOD cuts. Per-sample cuts flag a subset of detectors within a given TOD for an interval of time. For example, we flag samples affected by glitches and point sources using per-sample cuts to remove them from mapmaking. Per-detector cuts identify detectors that experience pathological conditions and flag the entire detector TOD

($\sim$ 10 minutes) to be cut. For example, we flag detectors with poor optical responsiveness and/or bad calibration using per-detector cut and remove them from mapmaking. Per-TOD cuts apply to an entire TOD, with all the detectors included. This applies when, e.g., a TOD is obtained at a bad weather condition (e.g., with high pwv), in which case we remove all detectors within the TOD from mapmaking.

The data cuts pipeline used for ACT DR4 is described briefly in Ref. [98], and in more depth in Ref. [246], which has a somewhat dated description. Several changes have been introduced in DR6 but not described elsewhere. Hence, we fill the gap in this chapter and describe the data cuts pipeline used in ACT DR6.

5.3.2 Per-sample cuts

We first generate per-sample cuts. In particular, we start by identifying glitches in each detector TOD. As glitches occur on a short time scale, we first apply a high-pass filter to keep only frequencies above 5 Hz and then apply a Gaussian filter with a full-width-half-maximum (FWHM) of $\sim 0.015\,\mathrm{s}$ which is the typical time scale of a glitch. We estimate the white noise level after the filtering (using inter-quantile range to be more robust to outliers) and then flag samples with $S/N \geq 10$ as glitch events. Each interval identified is padded with a buffer of 200 samples ($\sim 0.5\,\mathrm{s}$ with a data acquisition rate of 400 Hz) on each side. Adjacent intervals with a gap smaller than 30 samples are automatically merged. We save the flagged intervals as per-sample cuts and remove samples within the intervals from mapmaking.

One caveat in the aforementioned steps is that point sources may be bright enough to be visible in each detector timestream with $S/N \geq 10$, and they may be flagged as glitches mistakenly by the glitch finder. This problem needs to be fixed because point sources in the map are important tools for the calibration of pointing model (P in Equation 113). Planets, in particular, are also important for the absolute calibration of our maps and the characterization of telescope beams. To circumvent this problem, we use an existing point source map to mask all pixels within a 3 arcminute radius to a point sources with flux $\geq 5\,\mathrm{mK}$. Denoting this pixel-space mask as m_{src}, we project it to a timestream mask d_{src} by applying the mapmaking equation, $d_{\mathrm{src}} = Pm_{\mathrm{src}}$. We remove samples flagged by d_{src} as near

a bright source and gapfill them before applying the glitch finder. This ensures that point sources will not be flagged as glitches by the glitch finder.

In addition to glitches, we also flag time samples based on the scan pattern. In particular, as ACT scans across the sky in a periodic motion azimuthally, two turnarounds occur within each period of the azimuthal scan. The change of motion at the turnarounds may lead to mechanical vibrations within the instrument leading to unreliable measurements near the turnarounds. Hence, we flag the turnaround samples in each detector TOD and remove them from mapmaking. In addition, we also flag samples when the telescope suddenly stops scanning, or scans with a speed that differs from the expected speed in the middle of an observational run. These samples are also removed from mapmaking.

5.3.3 Per-detector cuts

After generating the per-sample cuts, we evaluate the performance of each detector in a TOD and flag detectors that show sporadic pathologies. In particular, we first calibrate each detector within each TOD from data acquisition units to a physical unit of pW. We adopt a different calibration strategy for ACT DR6 compared to ACT DR4 [98]. The difference is explained in Appendix A of Ref. [247] and will not be elaborated here. Calibration measurements are performed every ~ 10 minutes, which we match to each detector TOD. Detectors without a valid calibration are flagged and removed from mapmaking. The remaining detectors are termed as live detector candidates.

As different sources of noise manifest in different frequency ranges in a TOD power spectrum, we evaluate detector performance through a multi-frequency analysis. In particular, we divide the power spectrum into two broad bands: a low-frequency band ($\sim 0.01\,\mathrm{Hz}$–$0.1\,\mathrm{Hz}$), which is expected to be dominated by atmospheric noise, and a high-frequency band ($\sim 10\,\mathrm{Hz}$–$20\,\mathrm{Hz}$), which is expected to be dominated by detector random noise.

5.3.3.1 Low-frequency analysis

In the low frequency band ($\sim 0.01\,\mathrm{Hz}$–$0.1\,\mathrm{Hz}$) of a TOD, the 1/f atmospheric noise dominates with a knee frequency of $\sim 1-10\,\mathrm{Hz}$ depending on PWV. We expect all live detectors

to see the atmospheric signal, which in turn acts as a common mode across detectors. Detectors poorly correlated with the atmospheric signal may be contaminated by large systematic error. They need to be identified and removed from mapmaking. To do that we perform a common-mode analysis using Singular Value Decomposition (SVD). If we denote the TOD as a matrix $d \equiv d_i(t)$, which has a shape $n_d \times n_t$ with n_d the number of detectors and n_t the number of time samples, the TOD can then be decomposed as

$$d = USV^T, \tag{116}$$

where both U and V are column-wise orthonormal matrices that satisfy $U^TU = 1$, and $V^TV = 1$, with shape $n_i \times n_m$, and $n_t \times n_m$, respectively. n_m is the number of common modes obtained using SVD. S is a diagonal matrix with non-negative elements and a shape of $n_m \times n_m$. It is often referred to as the relevance matrix. Each element (S_{ii}) in the relevance matrix corresponds to a common mode, with S_{ii} being the relative importance of the mode. Hence, we expect the mode with largest S_{ii} to be associated with the atmospheric common mode. Note that the common modes are extracted using the low frequency part of a TOD. This implies that the TOD is to be first preprocessed with a combination of a high-pass and a low-pass filter to keep only the frequencies within ~ 0.01 Hz–0.1 Hz. In practice we simplify this step by performing the common mode analysis in Fourier space within the frequency band which is completely equivalent, but for pedagogical purposes we only describe the steps in time domain. From Equation 116,

$$dV = US. \tag{117}$$

If we denote the ith column of V as v_i, the ith normalized mode ($\hat{m}_i$) can then be written as

$$\hat{m}_i = v_i / S_{ii}, \tag{118}$$

and the response of detector j to the common mode $\hat{m}_i$ (defined as gain) is given by

$$g_{ji} = d_j \hat{m}_i = U_{ji}. \tag{119}$$

Assuming the atmospheric mode is the strongest mode (with $i = 0$), the response of each detector to this mode characterizes the optical gain of each detector, given by U_{j0}, which we

refer to simply as `gain` hereafter. `gain` is one of the three pathological parameters that we extract from each detector TOD to characterize the performance of each detector in the low frequency band of a TOD.

Another two pathological parameters that we extract are termed as `norm` and `corr`. Specifically, `norm` is defined as the norm of the TOD signal within the low-frequency band, given by $\|d_i\|$ for the ith detector. `corr` is defined as the correlation between a detector TOD and the strongest common mode $\hat{m}_0$, given by $d_i \cdot \hat{m}_0 / \|d_i\|$. `corr` approaches 1 when d_i is completely dominated by $\hat{m}_0$, i.e., no other modes are present. Hence, `corr` is a useful measure of the amount of contaminating modes in a detector TOD.

One caveat of SVD decomposition is that the extracted common mode is sensitive to outliers, which are common in a TOD due to defective detectors. To reduce the impact of outliers, before applying SVD decomposition, we perform a preselection step to identify a "well-behaved" group of detectors that are highly correlated with each other and then use TODs from these detectors to extract the common modes. In particular, the preselection is done by first computing the full detector-detector correlation matrix $\mathbf{M}$ and then select detectors with a median correlation (to all other detectors) above a given threshold (≥ 0.9). If too few detectors (≤ 10) are found to satisfy this criteria, we flag the entire TOD as problematic due to a failure to see an atmospheric common mode, and remove it from mapmaking. Note that in ACT DR4 [98] only the preselected detectors are used for mapmaking, which leads to lower detector yields in general. In contrast, in ACT DR6 we only use the preselected detectors to extract the common modes and not for mapmaking. This leads to overall better detector yields in ACT DR6.

Another issue is that although we have assumed that the strongest common mode is dominated by the atmospheric signal, this is not necessarily true, because other effects such as thermal drift and scan synchronous signal may also show up on a similar timescale and hence impact the common mode estimation. To reduce the impact from scan synchronous signal, we deproject harmonics of the scan frequency from the TOD before extracting the common modes using SVD. To reduce the impact from thermal contamination, in ACT DR4 we made used of dark detectors, which do not couple optically but only thermally, to estimate the thermal signal and deproject it from detector TODs. However, the three new

detector arrays (PA4, PA5, PA6) introduced from 2017 onward do not have functioning dark detectors due to hardware limitation. Hence, we are unable to deproject thermal signal for ACT DR6 TODs. This should be kept in mind when interpreting the DR6 results.

As the low-frequency analysis relies on a predefined frequency window, the window choice may potentially bias the results especially when scan pattern changes. To make our analysis more robust, we repeat the same analysis across a total of 10 rolling frequency windows with steps of 0.05 Hz, and we obtain the pathological parameters as averages across all frequency windows.

As a result of the low-frequency analysis, we obtain three pathological parameters, `gain`, `corr`, and `norm`, that characterize each detector TOD.

5.3.3.2 High-frequency analysis

In the high-frequency band (10 Hz–20 Hz), random detector noise dominates the power spectrum of a TOD, with an approximately white spectrum. The noise property of a detector is an important performance indicator. Thus we measure three pathological parameters in the high-frequency band to characterize the noise property of each detector. In particular, we measure the root-mean-square noise level (standard deviation) of each detector TOD, termed as `rms` hereafter. As we expect the detector noise to be approximately Gaussian, deviation from Gaussian statistics is a sign of pathological problem in the detector. To estimate such deviation, we also measure higher order statistical moments including skewness, which characterizes the asymmetry of the signal distribution and is term as `skew` hereafter, and kurtosis, which characterizes the tail distribution of the signal and is termed as `kurt` hereafter.

Note that in order for these pathological parameters to be meaningful measures of the noise property of each individual detector, the high-frequency band of a TOD should be negligibly contaminated by systematic errors, which is often not the case in practice. On the other hand, as systematic errors often lead to correlated noise across detectors, we can identify the correlated noise modes using SVD, in a similar way as in the low-frequency analysis (in Section 5.3.3.1), and deproject these correlated noise modes from detector TODs. The

resulting TOD is now dominated by uncorrelated noises, from which we can then evaluate the noise property of individual detectors using the pathological parameters `rms`, `skew`, and `kurt`. Specifically, we identify the 10 strongest correlated modes across detectors and deproject them from the detector TODs. If we denote the ith mode as $\hat{m}_i$, the deprojection is performed by

$$\tilde{d} = d(I - \hat{m}_i \hat{m}_i^T), \tag{120}$$

where $\tilde{d}$ is the TOD after deprojection.

As a result, we obtain three pathological parameters, `rms`, `skew`, and `kurt`, that characterize the noise property of each detector in a given TOD.

5.3.3.3 Other statistics

In addition to analyzing TODs in two broad frequency bands, we also obtain two more pathological parameters to evaluate systematic errors in detectors, termed as `drift error` and `mid-frequency error`.

As TOD signals often drift slowly on the timescale of minutes due to changes in atmospheric emission which acts as the strongest common mode across detectors, any slow drift that deviates from the common mode behavior may be a sign of systematic error in the detector TOD. Hence we define a term `drift error` to estimate such systematic error. To calculate `drift error`, we first low-pass filter the detector TODs to keep only frequencies below $\sim 0.03\,\mathrm{Hz}$ and then use SVD to obtain correlated modes across detectors. We deproject the 3 strongest correlated modes from detector TODs and calculate `drift error` as the root-mean-square noise level (standard deviation) in the detector TODs after deprojection.

The `mid-frequency error` is a similar measure to `drift error` but at a different frequency range (0.3 Hz–1 Hz). We expect the atmospheric signal to be much weaker in this frequency range, reaching a comparable level to thermal signal. Therefore, the strongest common mode in this frequency range is likely contributed by a combination of atmospheric and thermal signal. Any deviations from the common mode behavior in this frequency range may be manifestation of systematic error, and hence we define a pathological parameter `mid-frequency error` as a smoking gun of such problem. `mid-frequency error` is

name	freq
`gain`	$\sim$0.01 Hz–0.1 Hz
`corr`	$\sim$0.01 Hz–0.1 Hz
`norm`	$\sim$0.01 Hz–0.1 Hz
`rms`	10 Hz–20 Hz
`skew`	10 Hz–20 Hz
`kurt`	10 Hz–20 Hz
`drift error`	$\lesssim$ 0.03 Hz
`mid-freq error`	0.3 Hz–1 Hz

Table 5.2: Pathological parameters used to characterize the performance of each detector in a given TOD. The right column indicates the frequency range that the corresponding parameter is extracted from.

calculated using similar steps as for `drift errors`. Specifially, we first apply a combination of low-pass and high-pass filters to keep only frequencies with 0.3 Hz to 1 Hz in the TOD, and then we obtain common modes using SVD and deproject the 8 strongest correlated modes from every detector TOD. `mid-frequency error` is then calculated as the root-mean-square noise in the resulting detector TODs after deprojection.

5.3.3.4 Summary of pathological parameters

With the multi-band analysis described above, we obtain a total of 8 pathological parameters to characterize the performance of each detector in a given TOD, as summarized in Table 5.2.

We compute these pathological parameters for all TODs within the scope of ACT DR6 and collect them based on its detector array (PA4, PA5, PA6), frequency band (f090, f150, f220), and observational season (s17, s18, s19), resulting in a total of 18 datasets [1]. Based on

[1] As we use dichroic detector array, each array has two frequency band, so the total number of datasets is $3 \times 2 \times 3 = 18$

the statistical distribution of the pathological parameters in each dataset, we cut detectors with outlying statistics by defining absolute or percentile-based thresholds in each pathological parameter and remove them from mapmaking. The thresholds are adjusted for each dataset to accommodate instrumental and/or seasonal differences.

In addition to the threshold-based cuts, we also cut a detector TOD when an excessive number of glitches (> 20000) occur within the detector TOD, or when $> 40\%$ of the samples in a detector TOD are cut by per-sample cuts, although both cases rarely happen in practice.

5.3.4 Per-TOD cuts

Although most of the cuts are on per-sample and per-detector basis, there are occasions when an entire TOD is cut. This happens when a TOD has fewer than a predefined number of detectors (< 100) that pass the per-detector cut, and when a TOD is acquired during a bad weather such as snow storms or during high optical loading ($\mathrm{PWV}/\sin(\alpha) > 4\,\mathrm{mm}$, with α being the altitude angle). In addition, we also cut an entire TOD when the data is collected during telescope instrumentation.

5.4 Results for DR6

In Table 5.3 we summarize the yields of the data cuts pipeline for ACT DR6. It shows that on average $\sim 90\%$ of the TODs get processed. The TODs that fail to be processed are due a variety of reasons including failure to extract a common mode, wrong encoding of telescope pointing, and TOD being to short for low-frequency analysis. In terms of individual detectors, on average $\sim 70\% - 90\%$ of the live detector candidates pass the cuts. Among different frequency bands, f220 has the lowest yield across all seasons, which implies that the f220 data s likely more susceptible to systematic errors. This is also reflected in the low calibration yield as apparently only $\sim 50\%$ of the detectors have valid calibration measurements. Overall $\sim 80\%$ of the calibrated data pass the data cuts. This is considerably higher than the $\sim 70\%$ obtained for ACT DR4 as reported in Ref. [98]. This is likely due

	s17			s18			s19		
	f090	f150	f220	f090	f150	f220	f090	f150	f220
TOD									
Total TOD	31323	46823	15500	30280	45254	14974	48535	72454	23919
Processed	29470	42736	13666	28551	41198	12778	46929	67984	21129
Percentage	94.1%	91.3%	88.2%	94.3%	91.0%	85.3%	96.7%	93.8%	88.3%
Detector									
N_{det}	1704	2710	1006	1704	2710	1006	1704	2710	1006
$N_{\text{candidates}}$	1382	1989	534	1382	1989	534	1382	1989	534
$\langle N_{\text{uncut}} \rangle$	1258.1	1772.6	405.2	1199.1	1693.2	381.4	1187.7	1696.7	392.5
Percentage	91.0%	89.1%	75.9%	86.8%	85.1%	71.4%	85.9%	85.3%	73.5%
Overall									
Percentage	85.6%	81.3%	66.9%	81.8%	77.5%	60.9%	83.1%	80.0%	64.9%

Table 5.3: Yield of the data cuts pipeline for ACT DR6. N_{det} denotes the total number of optical coupled detectors, $N_{\text{candidates}}$ denotes the number of detectors with a valid calibration. $\langle N_{\text{uncut}} \rangle$ denotes the mean number of detectors that survives the data cuts. The percentage in the Detector section is defined as $\langle N_{\text{uncut}} \rangle / N_{\text{candidate}}$ which is an indicator of the performance of per-detector cuts. The overall percentage is defined as a product of the processed percentage of TODs and the detector percentage mentioned above. It is an indicator of the overall performance of the data cuts pipeline.

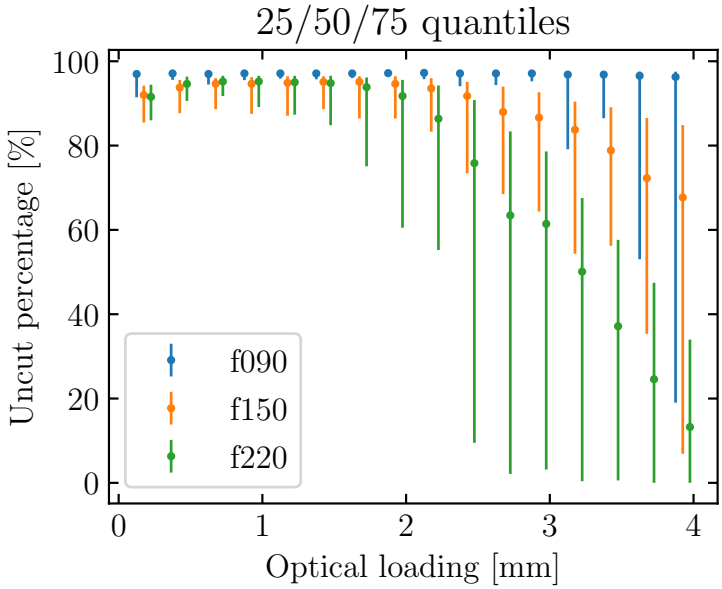

Figure 5.5: Percentage of live detector candidates that pass the cuts as a function of optical loading, which is defined as PWV/ $\sin(\alpha)$ with α being the altitude angle. Each dot denotes the median percentage, and the errorbar extends from the 25th percentile to the 75th percentile. f090 results (blue) are derived from PA5 in s19, and both f150 (orange) and f220 (green) results are derived from PA4 in s19. Data points are offsetted for better visualization.

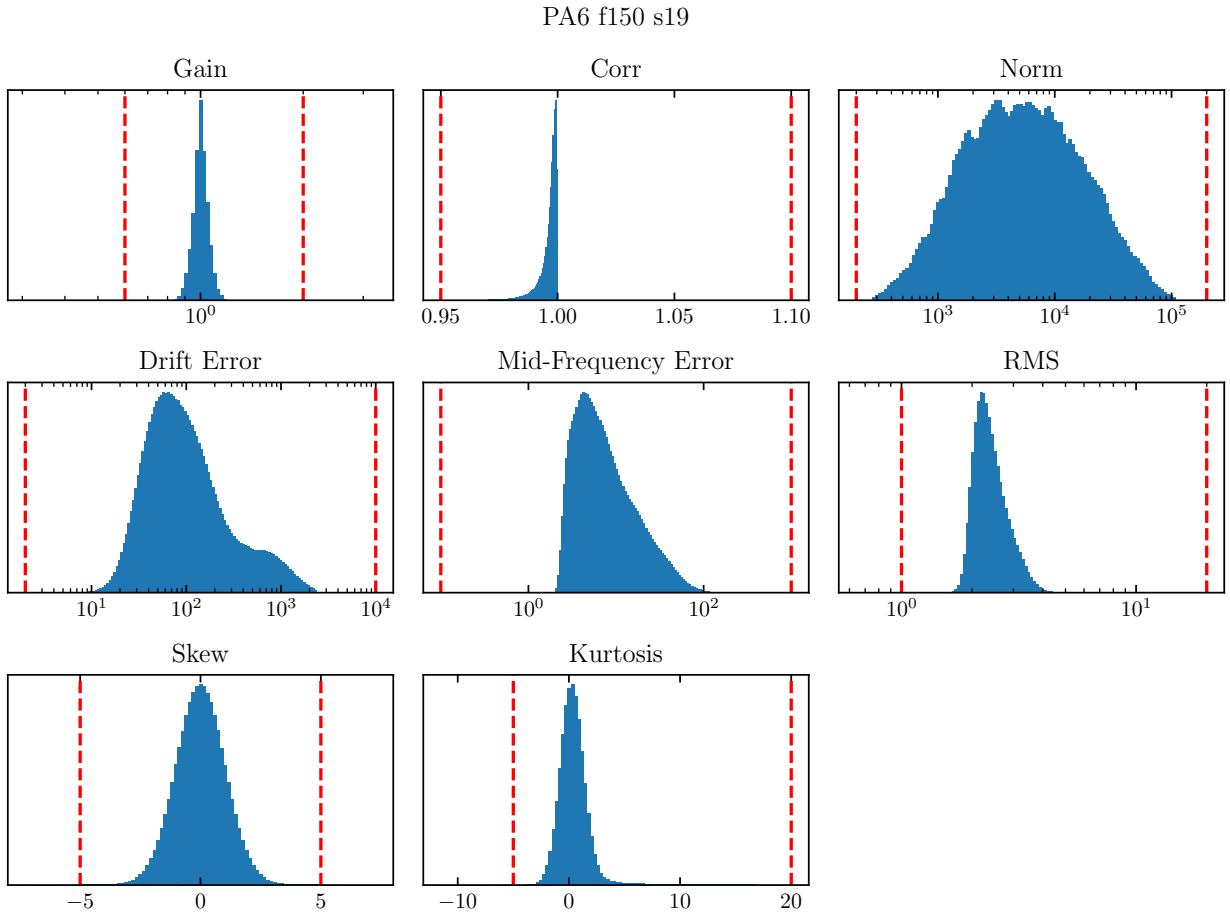

Figure 5.6: Histograms of pathological parameters from detector array PA6 and frequency band f150 obtained in season s19. Red dashed lines indicate the thresholds applied to the pathological parameters to flag outliers and generate detector cuts.

to a combination of improved preselection algorithm as described in Section 5.3.3.1 and the improved data quality in ACT DR6.

In Figure 5.5 we show the percentage of live detector candidates that pass the cuts at different PWV bins. As the optical loading ($\mathrm{PWV}/\sin(\alpha)$) increases, the higher frequency bands suffer more detector loss, while the low frequency band f090 sees an almost constant median percentage. This is consistent with our expectation that the higher frequency bands see more emission from the atmosphere and are more sensitive to PWV changes, as seen clearly in Figure 5.2. In addition, when the optical loading is $\lesssim 0.2\,\mathrm{mm}$, a small reduction in the detector yield can be seen across different frequency bands and most noticeably at higher frequencies (f150 and f220). This is as expected because at low optical loading the atmosphere emission is significantly reduced and no longer acts as a good common mode across detectors. This manifests in the pathological parameters as, e.g., lower `corr`, which results in more detectors being cut.

In Figure 5.6 we show a representative set of histograms of pathological parameters obtained from PA6 in the f150 band and observational season s19. The histograms are shown together with the threshold-based cuts applied to identify detectors with sporadic pathologies. As `gain` measures the amplitude of the atmospheric common mode that each detector sees. When detectors are properly calibrated, we expect `gain` to sharply center around 1 after removing an arbitrary normalization constant. On the other hand, if the atmospheric common mode is contaminated by non-atmospheric signals such as thermal drift, the distribution of `gain` will instead be tilted and/or multi-modeled. In the upperleft of Figure 5.6 we see that the histogram of `gain` is nicely centered around 1, indicating that the contamination from thermal modes to the atmospheric common mode is likely small, and the amplitudes extracted from our common mode analysis are in agreement with our calibration model obtained independently of the atmosphere, which is reassuring. We also see that the histogram of `corr` is highly tilted toward 1. As `corr` represents the correlation to the atmospheric common mode, we expect the non-atmospheric modes in our data to constitute only $\lesssim 2\%$ of the observed data at the low-frequency band of a TOD, consistent with our expectation based on the histogram of `gain`. The histogram of `drift error`, on the other hand, shows a slight bimodal distribution, hinting that although the impact from

thermal drifts is likely small, potentially a small subset of detectors still experience slow drifts that are uncorrelated to the atmospheric and thermal modes. In terms of detector noise, the histograms of `rms`, `skew`, and `kurt` show that the detectors generally have have well-behaved noise properties. In particular, the higher order statistics are consistent with zero, and `rms` also features a smooth Gaussian-like distribution. Overall, although the histograms are shown for a particular dataset, we find them representative of the other datasets. The results support the fact that ACT DR6 data are not significantly affected by systematic errors and the detectors are generally well-behaved.

5.5 Future prospects

ACT will stop collecting data at the end of observation season 2021. Its scientific goals will be superseded by the Simons Observatory (SO) [30] which is currently under construction and scheduled to see the first light in 2021. As SO will collect 5 times more data than ACT, it will pose a challenge to the data cuts pipeline, as the existing cuts pipeline is computationally intensive and requires a significant amount of human intervention in fine-tuning the threshold-based cuts for each dataset. In addition, as transient science will also be one of the scientific goals for SO, it may require generating daily maps of the sky, which in turn requires daily generation of data cuts. Running the existing data cuts pipeline on a daily basis is unfeasible particularly due to the human intervention required to tune the threshold-based per-detector cuts. Therefore, a more automated approach to generate detector cuts is well motivated to meet the scientific goals of the upcoming SO.

In the past decades we have seen rapid progress in the domain of machine learning (ML), which makes it a promising approach to automate the data cuts pipeline. In particular, as we have collected multiple seasons of data all of which have been processed through the existing cuts pipeline and labeled as either cut or uncut, our problem can be posed as a supervised binary classification problem, which is a common use case for ML algorithms.

As a proof of concept we implement a simple ML-based pipeline which takes the set of 8 pathological parameters calculated from the existing cuts pipeline as features and the per-

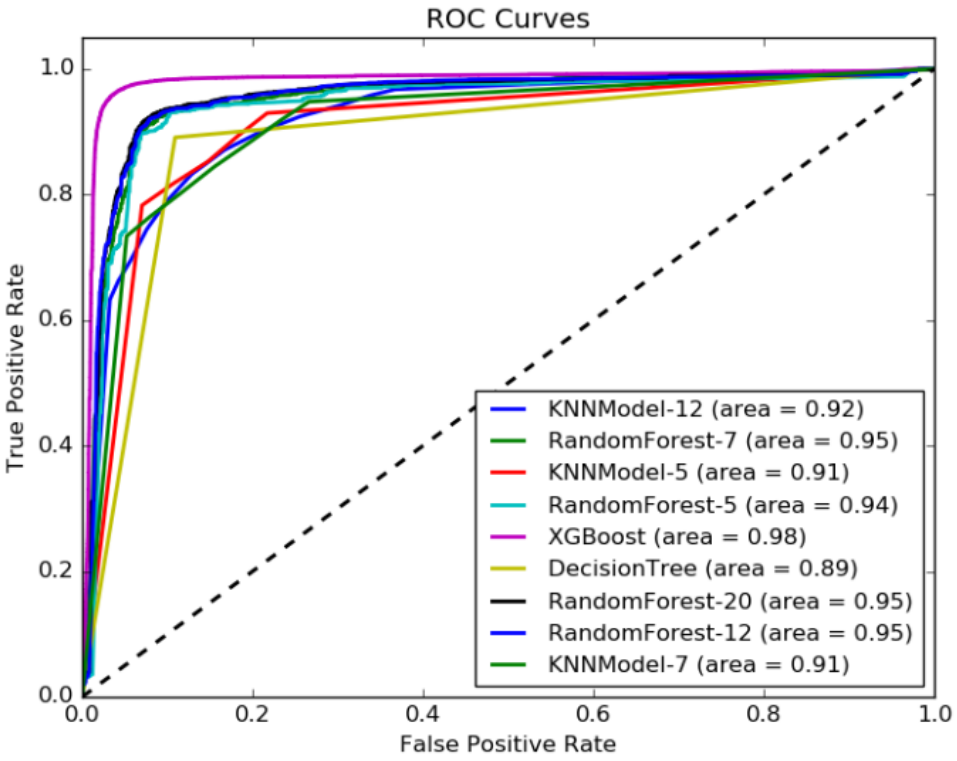

Figure 5.7: Receiver operating characteristic (ROC) curves of different ML models. Each curve characterizes the performance of a ML model in terms of true-positive rate versus false-positive rate as we adjust the probability threshold for positive prediction. Model with the highest area under the curve has the best overall performance, which is found to be the XGBoost model. Postfixes as in `KNNModel-x` denotes the number of estimators in the model.

detector cut as labels. The objective is that when we supply the pathological parameters of a new TOD to the ML model, it is able to generate the detector cuts automatically without the need of human intervention. We test the ML-based pipeline on 400 TODs from the f090 band in the observational season 2016, which have been well characterized as part of ACT DR4. The dataset contains $\sim$ 160,000 labeled data which we split into two subsets, with 80% of the data as the training set and 20% of the data as the testing set. We further resample the training set such that the positive (uncut) and the negative (cut) samples are balanced to avoid bias in the training. We test a selection of popular machine learning algorithms including decision tree [248], random forest [249], k-nearest neighbours (k-NN) [250, 251], all of which are implemented in `Scikit-learn` [252], and gradient boosting which is implemented in the `XGBoost` package [253], and compare their performances in terms of the accuracy of the prediction when applying to the testing set.

In Figure 5.7 we show the true-positive rate of each machine learning algorithm against its false-positive rate, at various probability thresholds used to determine positive and negative predictions. The `XGBoost` algorithm stands out as it achieves the highest true positive rate for any given false-positive rate. It reaches an overall prediction accuracy of 97% when compared to the existing data cuts pipeline, showing promises in applying such algorithm in generating data cuts.

In addition to the within-season test, we also test the ML-based pipeline across different seasons. In particular, we train the ML models using data from s14 and s15, and use the trained model to predict detector cuts for s16 to test how transferrable is the learning of model when applied to a completely new dataset. The results for cross-season test are consistent with the within-season test, with `XGBoost` model outperforming the other ML models, reaching an accuracy of $\sim$ 90%. Considering that the s16 dataset may see completely different systematic errors than the previous seasons, the achieved accuracy in reproducing the existing detector cuts is very promising and demonstrates the high potential of a ML algorithm like `XGBoost` in automating the generation of detector cuts.

5.6 Discussions

The data cuts pipeline is of crucial importance to the success of ACT and the next-generation CMB experiments like the Simons Observatory. In this chapter we have presented a detailed description of the data cuts pipeline used in ACT DR6 and presented the results from applying the cuts pipeline to ACT DR6 data. From the results we have seen an overall improvement in detector yields when compared to ACT DR4, likely due to a combination of improvement in the cuts pipeline particularly in the low-frequency analysis and an overall improvement in the quality of the observational data in DR6.

We have also discussed the future prospects of the data cuts pipeline in light of the upcoming CMB experiments. As a future experiment like SO will collect an order of magnitude more data than ACT, running the same data cuts will be computational challenging especially when we want to make daily maps for transient science. This requires a more automated data cuts pipeline. In this chapter we have presented early studies of a machine learning based pipeline and demonstrated its huge potential in automating the generation of detector cuts.

6.0 Conclusion

We have, without doubts, entered the era of "precision cosmology". We now have enough statistics that allow us to constrain cosmological parameters to percent-level accuracy and probe tiny deviations from the standard cosmological model. In this thesis we presented three such applications, using the precision measurements of the Cosmic Microwave Background to expand our knowledge of the universe, demonstrating the power of such cosmological dataset.

With the increasing sensitivity in CMB polarization measurements, we are now closer to being able to detect the signature of a primordial gravitational wave in the CMB B-mode power spectrum. On the other hand, the improved sensitivities also mean that there are likely more confusion signals that show a similar signature, and hence more work is needed to rule out such degenerate models before one can claim the detection of a signal from inflation. In Chapter 2, we have investigated one of such degenerate models, namely, primordial magnetic field. In particular, we showed that the hypothesized primordial magnetic field (PMF), if it exists, may also generate a CMB B-mode signal that is highly degenerate to that of the primordial gravitational wave, particularly on the large angular scales. Thus we suggested that one should be cautious in claiming a discovery of inflationary signal when its signature shows up in the large angular scales. Fortunately, on the small angular scales, PMF leaves its unique signatures in the form of a vector-mode perturbation which gives us a handle in ruling it out. In fact, we demonstrated that by leveraging the precision measurements of the small scale CMB anisotropies to constrain the vector-mode signal from the PMF, one can effectively rule out a degenerate PMF model for $r \gtrsim 0.01$ for an Simons Observatory-like experiment and $r \gtrsim 0.004$ for a CMB S4-like experiment. Furthermore, PMF also induces an effect known as the Faraday rotation on the CMB polarization, causing a net rotation of the linear polarization of the CMB photons. We demonstrated that such effect can generate a B-mode signal detectable with the sensitivity of the upcoming CMB experiments, though it will unlikely provide a strong constraint on the PMF. On the other hand, the Faraday rotation also induces off-diagonal cross-correlations in the E- and B-mode polarization maps.

We showed that this effect will likely provide the strongest constraint on PMF among the effects discussed in Chapter 2, allowing us to rule-out degenerate PMF models for $r \gtrsim 0.001$. Overall, our study presented a solid evidence in support of the view that a PMF model is unlikely a challenge for the B-mode searches of the primordial gravitational wave, provided that one includes the small-scale CMB anisotropies in the constraint, because precision measurements of the small-scale anisotropies of the upcoming CMB experiments will have enough sensitivities to rule out the degenerate PMF models for the targeting ranges of the B-mode signal.

Faraday rotation is not the only physical mechanism that causes a rotation in the polarization direction of CMB photons. In fact, cosmic birefringence can be a generic feature of models beyond the standard model of physics that introduce parity-violating physics in the early universe. Such models often predict an anisotropic rotation field with a scale-invariant rotation power spectrum, which can be constrained in a model independent way. In Chapter 3, we performed a search for such signal in the data obtained by the ACT experiment, by searching for the off-diagonal correlation between the E- and B-mode polarization maps caused by the polarization rotation, which we found to give the strongest constraint on such signal in Chapter 2. We reconstructed the rotation power spectrum and found it consistent with zero. With the non-detection, we placed a constraint on the amplitude of a scale-invariant rotational field, which improved the previous limit by a factor of 3 and reduced the allowed parameter space for parity-violating physics beyond the standard model.

In addition to cosmology, we also demonstrated that high angular resolution measurements of the microwave sky from a CMB experiment are valuable for astronomy, particularly for Galactic science. In Chapter 4 we presented the microwave maps of the Galactic center regions of our galaxy, made by combining the data obtained from ACT and Planck. These maps improved the previous maps in this region in the millimeter wavelengths in both sensitivity and angular resolution, particularly in polarization. These improvements allowed us to probe the magnetic field morphology of the Galactic magnetic field in arpcmin resolution while maintaining a wide field of view. We also probed magnetic fields on top of known radio sources and molecular clouds, significantly improving our knowledge of the magnetic field environment at some of these regions.

I also presented preparation works for the upcoming data release from ACT (DR6) which will contain a factor of 5 more data than the previous ACT data release (DR4) and is expected to improve our constraining power in cosmology by a factor of 2. In Chapter 5, I presented a detailed description the data reduction process known as the data cuts pipeline which identifies data with sporadic pathologies and removes them from mapmaking. I also presented the preliminary results of the cuts pipeline for ACT DR6 which showed an overall improved quality compared to ACT DR4, likely contributed by a combination of the improved cuts algorithm and the improved control of the systematics. In addition, I discussed the prospects of the data cuts pipeline in the context of the upcoming Simons Observatory, because it will collect a factor of 5 more data than ACT and may pose a challenge to the data cuts pipeline which is both computationally insensitive and manpower demanding in fine-tuning the threshold-based cuts. In light of this, I also discussed a promising new way to generated data cuts without any human intervention with the help of machine learning algorithms. I presented some preliminary results from a machine learning based cuts pipeline and demonstrated that it is capable of reproducing the expert-based cuts pipeline with $\gtrsim 90\%$ accuracy. Being able to generate data cuts automatically will enable the Simons Observatory to make daily maps of the sky which opens doors to doing transient science with the Simons Observatory.

In closing, with the help of the current high precision measurements of the CMB and the upcoming CMB datasets to come, it is without doubt that our knowledge of the universe will be significantly expanded, with our theoretical model tested and confronted by new experimental findings.

Bibliography

[1] Planck Collaboration VI. *Planck* 2018 results. VI. Cosmological parameters. *A&A, in press*, 2019.

[2] Antony Lewis and Anthony Challinor. CAMB: Code for Anisotropies in the Microwave Background, February 2011.

[3] Lawrence M. Krauss, Scott Dodelson, and Stephan Meyer. Primordial Gravitational Waves and Cosmology. *Science*, 328(5981):989, May 2010.

[4] POLARBEAR Collaboration, Peter A. R. Ade, Kam Arnold, Matt Atlas, Carlo Baccigalupi, Darcy Barron, et al. Polarbear constraints on cosmic birefringence and primordial magnetic fields. *PhRvD*, 92:123509, 2015.

[5] BICEP2 / *Keck Array* Collaboration. BICEP2 / *keck array* ix: New bounds on anisotropies of cmb polarization rotation and implications for axion-like particles and primordial magnetic fields. *PhRvD*, 96:102003, 2017.

[6] Dagoberto Contreras, Paula Boubel, and Douglas Scott. Constraints on direction-dependent cosmic birefringence from Planck polarization data. *JCAP*, 1712(12):046, 2017.

[7] I. Heywood, F. Camilo, W. D. Cotton, F. Yusef-Zadeh, T. D. Abbott, et al. Inflation of 430-parsec bipolar radio bubbles in the Galactic Centre by an energetic event. *Nature*, 573(7773):235–237, September 2019.

[8] S. Molinari, E. Schisano, D. Elia, M. Pestalozzi, A. Traficante, et al. Hi-GAL, the Herschel infrared Galactic Plane Survey: photometric maps and compact source catalogues. First data release for the inner Milky Way: $+68^\circ \geq l \geq -70^\circ$. *A&A*, 591:A149, July 2016.

[9] Scott Paine. The am atmospheric model, September 2019.

[10] L. Knox and M. Millea. Hubble constant hunter's guide. *PhRvD*, 101(4):043533, February 2020.

[11] Adam G. Riess, Alexei V. Filippenko, Peter Challis, Alejandro Clocchiatti, Alan Diercks, et al. Observational Evidence from Supernovae for an Accelerating Universe and a Cosmological Constant. *AJ*, 116(3):1009–1038, September 1998.

[12] Chung-Pei Ma and Edmund Bertschinger. Cosmological Perturbation Theory in the Synchronous and Conformal Newtonian Gauges. pages 1–46, 1995.

[13] W. Hu and M. J. White. Cmb anisotropies: Total angular momentum method. *PhRvD*, 56:596–615, 1997.

[14] Arthur Kosowsky. The cosmic microwave background. *Modern Cosmology*, pages 219–263, 2001.

[15] V. F. Mukhanov, H. A. Feldman, and R. H. Brandenberger. Theory of cosmological perturbations. *PhR*, 215(5-6):203–333, June 1992.

[16] Julien Lesgourgues. The Cosmic Linear Anisotropy Solving System (CLASS) I: Overview. 2011.

[17] A. McKellar. Evidence for the Molecular Origin of Some Hitherto Unidentified Interstellar Lines. *PASP*, 52(307):187, June 1940.

[18] Walter S. Adams. Some Results with the COUDÉ Spectrograph of the Mount Wilson Observatory. *ApJ*, 93:11, January 1941.

[19] JF Denisse, J Lequeux, and E Leroux. Nouvelles observations du rayonnement du ciel sur la longueur donde 33 cm. *COMPTES RENDUS HEBDOMADAIRES DES SEANCES DE L ACADEMIE DES SCIENCES*, 244(25):3030–3033, 1957.

[20] TA Shmaonov. "metodika absolyutnykh izmerenii effektivnoi temperatury radioizlucheniya s nizkoi ekvivalentnoi temperaturoi"("method of absolute measurements of the effective temperature of radio emission with low equivalent temperature"). *Prib. Tekh. Eksp*, 1:83, 1957.

[21] A. A. Penzias and R. W. Wilson. A Measurement of Excess Antenna Temperature at 4080 Mc/s. *ApJ*, 142:419–421, July 1965.

[22] R. H. Dicke, P. J. E. Peebles, P. G. Roll, and D. T. Wilkinson. Cosmic Black-Body Radiation. *ApJ*, 142:414–419, July 1965.

[23] R. A. Alpher, H. Bethe, and G. Gamow. The origin of chemical elements. *Phys. Rev.*, 73:803–804, Apr 1948.

[24] William H. Kinney. Lectures on Inflation. pages 447–543, 2009.

[25] J. N. Goldberg, A. J. Macfarlane, E. T. Newman, F. Rohrlich, and E. C. G. Sudarshan. Spin-s Spherical Harmonics and ð. *Journal of Mathematical Physics*, 8(11):2155–2161, November 1967.

[26] W Hu, M Hedman, and M. Zaldarriaga. Benchmark parameters for cmb polarization experiments. *PhRvD*, 67:043004, 2003.

[27] Lloyd Knox and Michael S. Turner. Detectability of tensor perturbations through anisotropy of the cosmic background radiation. *PhRvL*, 73(25):3347–3350, December 1994.

[28] Uroš Seljak and Christopher M. Hirata. Gravitational lensing as a contaminant of the gravity wave signal in the CMB. *PhRvD*, 69(4):043005, February 2004.

[29] Planck Collaboration X. *Planck* 2018 results. X. Constraints on inflation. *A&A, in press*, 2019.

[30] Peter Ade, James Aguirre, Zeeshan Ahmed, Simone Aiola, Aamir Ali, David Alonso, Marcelo A. Alvarez, Kam Arnold, Peter Ashton, Jason Austermann, and et al. The Simons Observatory: science goals and forecasts. *JCAP*, 2019(2):056, February 2019.

[31] J. A. Grayson and others (BICEP3 Collaboration). Bicep3 performance overview and planned keck array upgrade. *Proc. SPIE Int. Soc. Opt. Eng.*, 9914:99140S, 2016.

[32] M. Hazumi, P. A. R. Ade, Y. Akiba, D. Alonso, K. Arnold, et al. LiteBIRD: A Satellite for the Studies of B-Mode Polarization and Inflation from Cosmic Background Radiation Detection. *J. Low. Temp. Phys.*, 194:443–452, 2019.

[33] CMB-S4 Collaboration, Kevork N. Abazajian, Peter Adshead, Zeeshan Ahmed, et al. CMB-S4 Science Book, First Edition. *arXiv e-prints*, page arXiv:1610.02743, October 2016.

[34] P.A.R. Ade, Z. Ahmed, R. W. Aikin, K. D. Alexander, D. Barkats, et al. BICEP2 / Keck Array V: Measurements of B-mode polarization at degree angular scales and 150 GHz by the Keck Array. *Astrophysical Journal*, 811(2), 2015.

[35] Planck Collaboration, R. Adam, P. A. R. Ade, N. Aghanim, M. Arnaud, J. Aumont, C. Baccigalupi, A. J. Banday, R. B. Barreiro, J. G. Bartlett, and et al. Planck intermediate results. XXX. The angular power spectrum of polarized dust emission at intermediate and high Galactic latitudes. *A&A*, 586:A133, February 2016.

[36] P. A. R. Ade, Z. Ahmed, R. W. Aikin, K. D. Alexander, et al. Constraints on primordial gravitational waves using *planck*, wmap, and new bicep2/*keck* observations through the 2015 season. *Phys. Rev. Lett.*, 121:221301, Nov 2018.

[37] Lloyd Knox and Yong-Seon Song. Limit on the Detectability of the Energy Scale of Inflation. *PhRvL*, 89(1):011303, July 2002.

[38] W. Hu and T. Okamoto. Mass reconstruction with cmb polarization. *ApJ*, 574:566–574, 2002.

[39] Omar Darwish, Mathew S Madhavacheril, Blake Sherwin, Jo Dunkley, Simone Ferraro, J Colin Hill, Toshiya Namikawa, Bruce Partridge, J Qu, Naomi Robertson, Neelima Sehgal, and Edward J Wollack. The Atacama Cosmology Telescope : A CMB lensing mass map over 2100 square degrees of sky and its cross-correlation with BOSS-CMASS galaxies. (January), 2020.

[40] SPT Collaboration (Holder, G. P. et al.). A cosmic microwave background lensing mass map and its correlation with the cosmic infrared background. *ApJ*, 771:L16, 2013.

[41] *Planck* Collaboration. Planck 2018 results. viii. gravitational lensing. *A&A*, 2018.

[42] Gabrielle Simard, Duncan Hanson, and Gil Holder. Prospects for Delensing the Cosmic Microwave Background for Studying Inflation. *ApJ*, 807(2):166, July 2015.

[43] David Alonso, Joanna Dunkley, Ben Thorne, and Sigurd Næss. Simulated forecasts for primordial B -mode searches in ground-based experiments. *PhRvD*, 95(4):043504, February 2017.

[44] Marc Kamionkowski and Ely D. Kovetz. The Quest for B Modes from Inflationary Gravitational Waves. *ARA&A*, 54:227–269, September 2016.

[45] Iain A. Brown. Concerning the statistics of cosmic magnetism. *arXiv e-prints*, page arXiv:1005.2982, May 2010.

[46] Levon Pogosian and Alex Zucca. Searching for primordial magnetic fields with CMB B-modes, 2018.

[47] Fabrizio Renzi, Giovanni Cabass, Eleonora Di Valentino, Alessandro Melchiorri, and Luca Pagano. The impact of primordial magnetic fields on future cmb bounds on inflationary gravitational waves. *Journal of Cosmology and Astroparticle Physics*, 2018(08):038–038, Aug 2018.

[48] Lawrence M. Widrow. Origin of galactic and extragalactic magnetic fields. *Reviews of Modern Physics*, 74(3):775–823, 2002.

[49] Andrii Neronov and Ievgen Vovk. Evidence for Strong Extragalactic Magnetic Fields from Fermi Observations of TeV Blazars. *Science*, 328(5974):73, Apr 2010.

[50] Michael S. Turner and Lawrence M. Widrow. Inflation-produced, large-scale magnetic fields. *Phys. Rev. D*, 37:2743–2754, May 1988.

[51] T. Vachaspati. Magnetic fields from cosmological phase transitions. *Phys. Lett.*, B265:258–261, 1991.

[52] J. Richard Shaw and Antony Lewis. Massive neutrinos and magnetic fields in the early universe. *Physical Review D*, 81(4):043517, 2010.

[53] Arthur Kosowsky, Tina Kahniashvili, George Lavrelashvili, and Bharat Ratra. Faraday rotation of the Cosmic Microwave Background polarization by a stochastic magnetic field. *PhRvD*, 71:043006, 2005.

[54] Alex Zucca, Yun Li, and Levon Pogosian. Constraints on primordial magnetic fields from planck data combined with the south pole telescope cmb b -mode polarization measurements. *Physical Review D*, 95(6):063506, 2017.

[55] P. A.R. Ade, N. Aghanim, M. Arnaud, F. Arroja, M. Ashdown, et al. Planck 2015 results. XIX. Constraints on primordial magnetic fields. *Astronomy and Astrophysics*, 594, oct 2016.

[56] V. B. Semikoz and D. Sokoloff. Magnetic helicity and cosmological magnetic field. *A&A*, 433(3):L53–L56, April 2005.

[57] L. Campanelli and M. Giannotti. Magnetic helicity generation from the cosmic axion field. *PhRvD*, 72(12):123001, December 2005.

[58] Andrew Mack, Tina Kahniashvili, and Arthur Kosowsky. Microwave background signatures of a primordial stochastic magnetic field. *Physical Review D*, 65(12), Jun 2002.

[59] J. M. Stewart and M. Walker. Perturbations of space-times in general relativity. *Proceedings of the Royal Society of London Series A*, 341(1624):49–74, October 1974.

[60] Tina Kahniashvili and Bharat Ratra. CMB anisotropies due to cosmological magnetosonic waves. *PhRvD*, 75(2):023002, January 2007.

[61] Michael S. Turner and Lawrence M. Widrow. Inflation-produced, large-scale magnetic fields. *PhRvD*, 37(10):2743–2754, May 1988.

[62] Wayne Hu and Martin J. White. CMB anisotropies: Total angular momentum method. *Phys. Rev.*, D56:596–615, 1997.

[63] Massimo Giovannini. Magnetized initial conditions for CMB anisotropies. *PhRvD*, 70(12):123507, December 2004.

[64] Fabio Finelli, Francesco Paci, and Daniela Paoletti. Impact of stochastic primordial magnetic fields on the scalar contribution to cosmic microwave background anisotropies. *PhRvD*, 78(2):023510, July 2008.

[65] Antony Lewis. CMB anisotropies from primordial inhomogeneous magnetic fields. *Phys. Rev.*, D70:043011, 2004.

[66] Camille Bonvin, Chiara Caprini, and Ruth Durrer. Magnetic fields from inflation: The CMB temperature anisotropies. *PhRvD*, 88(8):083515, October 2013.

[67] Planck Collaboration XIX. *Planck* 2015 results. XIX. Constraints on primordial magnetic fields. *A&A*, 594:A19, 2016.

[68] Jenni Adams, Ulf H. Danielsson, Dario Grasso, and Héctor Rubinstein. Distortion of the acoustic peaks in the CMBR due to a primordial magnetic field. *Physics Letters, Section B: Nuclear, Elementary Particle and High-Energy Physics*, 388(2):253–258, 1996.

[69] Tina Kahniashvili and Bharat Ratra. CMB anisotropies due to cosmological magnetosonic waves. *Physical Review D - Particles, Fields, Gravitation and Cosmology*, 75(2):1–17, nov 2006.

[70] Kerstin E. Kunze. CMB anisotropies in the presence of a stochastic magnetic field. *Physical Review D - Particles, Fields, Gravitation and Cosmology*, 83(2):1–26, 2011.

[71] Antony Lewis, Anthony Challinor, and Anthony Lasenby. Efficient computation of cosmic microwave background anisotropies in closed friedmann-robertson-walker models. *The Astrophysical Journal*, 538(2):473–476, Aug 2000.

[72] Samira Hamimeche and Antony Lewis. Likelihood Analysis of CMB Temperature and Polarization Power Spectra. *PhRvD*, 77:103013, 2008.

[73] Lloyd Knox and Marius Millea. Hubble constant hunter's guide. *Phys. Rev. D*, 101(4):043533, 2020.

[74] CMB-S4 Collaboration, Kevork Abazajian, Graeme Addison, Peter Adshead, Zeeshan Ahmed, et al. Cmb-s4 science case, reference design, and project plan. 2019.

[75] Levon Pogosian, Amit P. S. Yadav, Yi-Fung Ng, and Tanmay Vachaspati. Primordial magnetism in the cmb: Exact treatment of faraday rotation and wmap7 bounds. *Physical Review D*, 84(4), Aug 2011.

[76] E P Wigner. *On the Matrices Which Reduce the Kronecker Products of Representations of S. R. Groups*, pages 608–654. Springer Berlin Heidelberg, Berlin, Heidelberg, 1993.

[77] D. D. Sokoloff, A. A. Bykov, A. Shukurov, E. M. Berkhuijsen, R. Beck, and A. D. Poezd. Depolarization and Faraday effects in galaxies. *MNRAS*, 299(1):189–206, August 1998.

[78] Arthur Kosowsky, Tina Kahniashvili, George Lavrelashvili, and Bharat Ratra. Faraday rotation of the cosmic microwave background polarization by a stochastic magnetic field. *Physical Review D*, 71(4), Feb 2005.

[79] Kendrick M. Smith, Duncan Hanson, Marilena LoVerde, Christopher M. Hirata, and Oliver Zahn. Delensing cmb polarization with external datasets. *JCAP*, 06:014, 2012.

[80] J. N. Goldberg, A. J. Macfarlane, E. T. Newman, F. Rohrlich, and E. C.G. Sudarshan. Spin-s spherical harmonics and O. *Journal of Mathematical Physics*, 8(11):2155–2161, nov 1967.

[81] W. Hu. Mapping the dark matter through the cosmic microwave background damping tail. *ApJ*, 557:L79–L83, 2001.

[82] Fabio Finelli and Daniela Paoletti. Primordial Magnetic Fields in the Early Universe and Cosmic Microwave Background Anisotropies. In *Cosmic Magnetic Fields*, number 2018, pages 161–190. Cambridge University Press, 2018.

[83] Toshiya Namikawa, Yilun Guan, Omar Darwish, Blake D. Sherwin, et al. Atacama Cosmology Telescope: Constraints on cosmic birefringence. *PhRvD*, 101(8):083527, April 2020.

[84] R. J. Thornton, P. A. R. Ade, S. Aiola, F. E. Angilè, M. Amiri, et al. The Atacama Cosmology Telescope: The Polarization-sensitive ACTPol Instrument. *ApJS*, 227(2):21, December 2016.

[85] S. M. Carroll. *PhRvL*, 81:3067–3070, 1998.

[86] Mingzhe Li and Xinmin Zhang. Cosmological cpt violating effect on cmb polarization. *PhRvD*, 78:103516, 2008.

[87] Maxim Pospelov, Adam Ritz, and Constantinos Skordis. Pseudoscalar perturbations and polarization of the cosmic microwave background. *PhRvL*, 103:051302, 2009.

[88] Fabio Finelli and Matteo Galaverni. *PhRvD*, 79:063002, 2009.

[89] Renée Hlozek, David J. E. Marsh, and Daniel Grin. Using the Full Power of the Cosmic Microwave Background to Probe Axion Dark Matter. *MNRAS*, 476(3):3063–3085, 2018.

[90] D. J. E. Marsh. *Phys. Rep.*, 643:1, 2016.

[91] Ludovico M. Capparelli, Robert R. Caldwell, and Alessandro Melchiorri. Cosmic Birefringence Test of the Hubble Tension. 2019.

[92] Arthur Lue, Limin Wang, and Mark Kamionkowski. Cosmological signature of new parity-violating interactions. *PhRvL*, 83:1506–1509, 1999.

[93] C. Li, T. L. Smith, and A. Cooray. Non-gaussian covariance of cmb b-modes of polarization and parameter degradation. *PhRvD*, 75:083501, 2007.

[94] Robert R. Caldwell, Vera Gluscevic, and Marc Kamionkowski. *PhRvD*, 84:043504, 2011.

[95] Seokcheon Lee, Guo-Chin Liu, and Kin-Wang Ng. Cosmic Birefringence Fluctuations and Cosmic Microwave Background B-mode Polarization. *PhRvB*, 746:406–409, 2015.

[96] David Leon, Jonathan Kaufman, Brian Keating, and Matthew Mewes. *Mod. Phys. Lett. A*, 32:1730002, 2017.

[97] V. Gluscevic, M. Kamionkowski, and D. Hanson. Patchy screening of the cosmic microwave background by inhomogeneous reionization. *PhRvD*, 87:047303, 2013.

[98] Simone Aiola, Erminia Calabrese, Loïc Maurin, Sigurd Naess, Benjamin L. Schmitt, et al. The Atacama Cosmology Telescope: DR4 maps and cosmological parameters. *JCAP*, 2020(12):047, December 2020.

[99] Thibaut Louis, Emily Grace, Matthew Hasselfield, Marius Lungu, Loïc Maurin, et al. The Atacama Cosmology Telescope: Two-Season ACTPol Spectra and Parameters. *JCAP*, 1706:031, 2017.

[100] Steve K Choi, Matthew Hasselfield, Shuay-Pwu Patty Ho, Brian Koopman, Marius Lungu, et al. The Atacama Cosmology Telescope: a measurement of the Cosmic Microwave Background power spectra at 98 and 150 GHz. *jcap*, 2020(12):45, dec 2020.

[101] Flavien Vansyngel, François Boulanger, Tuhin Ghosh, Benjamin D. Wandelt, Jonathan Aumont, Andrea Bracco, François Levrier, Peter G. Martin, and Ludovic Montier. Statistical simulations of the dust foreground to cosmic microwave background polarization. *A&A*, 603:A62, 2017.

[102] *Planck* Collaboration. Planck 2015 results. ix. diffuse component seperation: Cmb maps. *A&A*, 594:A9, 2016.

[103] Blake D. Sherwin, Alexander van Engelen, Neelima Sehgal, Mathew Madhavacheril, et al. The atacama cosmology telescope: Two-season actpol lensing power spectrum. *PhRvD*, 95:123529, 2017.

[104] T. Okamoto and W. Hu. Cmb lensing reconstruction on the full sky. *PhRvD*, 67:083002, 2003.

[105] *Planck* Collaboration. Planck 2013 results. xvii. gravitational lensing by large-scale structure. *A&A*, 571:A17, 2014.

[106] T. Namikawa. Testing parity-violating physics from cosmic rotation power reconstruction. *PhRvD*, 95:043523, 2017.

[107] T. Namikawa, D. Hanson, and R. Takahashi. Bias-hardened cmb lensing. *MNRAS*, 431:609–620, 2013.

[108] Dongwon Han, Neelima Sehgal, Amanda MacInnis, Alexander Van Engelen, Blake D Sherwin, Mathew S Madhavacheril, et al. The Atacama Cosmology Telescope: delensed power spectra and parameters. *jcap*, 2021(01):031–031, jan 2021.

[109] Brian Keating, Meir Shimon, and Amit Yadav. Self-calibration of cmb polarization experiments. *ApJ*, 762:L23, 2012.

[110] J. P. Kaufman, N. J. Miller, M. Shimon, D. Barkats, C. Bischoff, et al. Self-calibration of bicep1 three-year data and constraints on astrophysical polarization rotation. *PhRvD*, 89:062006, 2014.

[111] *Planck* Collaboration. Planck intermediate results. XXX. The angular power spectrum of polarized dust emission at intermediate and high Galactic latitudes. *A&A*, 586:A133, 2016.

[112] *Planck* Collaboration. Planck 2018 results. XI. Polarized dust foregrounds. *A&A*, 2018.

[113] Sean M. Carroll, George B. Field, and Roman Jackiw. Limits on a Lorentz and Parity Violating Modification of Electrodynamics. *PhRvD*, 41:1231, 1990.

[114] Diego Harari and Pierre Sikivie. Effects of a Nambu-Goldstone boson on the polarization of radio galaxies and the cosmic microwave background. *PhRvB*, 289:67–72, 1992.

[115] Daniel Baumann. Inflation. In *Physics of the large and the small, TASI 09, proceedings of the Theoretical Advanced Study Institute in Elementary Particle Physics, Boulder, Colorado, USA, 1-26 June 2009*, pages 523–686, 2011.

[116] Howard Hui, P. A. R. Ade, Z. Ahmed, R. W. Aikin, K. D. Alexander, D. Barkats, et al. BICEP Array: a multi-frequency degree-scale CMB polarimeter. *Proc. SPIE Int. Soc. Opt. Eng.*, 10708:1070807, 2018.

[117] Adrian Lee, Maximilian H. Abitbol, Shunsuke Adachi, Peter Ade, James Aguirre, et al. The Simons Observatory: Astro2020 Decadal Project Whitepaper. *Bull. Am. Astron. Soc.*, 51:147, 2019.

[118] B. A. Benson, P. A. R. Ade, Z. Ahmed, S. W. Allen, K. Arnold, et al. Spt-3g: A next-generation cosmic microwave background polarization experiment on the south pole telescope. *Proc. SPIE*, 9153:91531P, 2014.

[119] Levon Pogosian, Meir Shimon, Matthew Mewes, and Brian Keating. Future cmb constraints on cosmic birefringence and implications for fundamental physics. *PhRvD*, D100:023507, 2019.

[120] Cara Battersby, Eric Keto, Daniel Walker, Ashley Barnes, Daniel Callanan, et al. CMZoom: Survey Overview and First Data Release. *ApJS*, 249(2):35, August 2020.

[121] R. Güsten. Gas and Dust in the Inner Few Degrees of the Galaxy (review). In Mark Morris, editor, *The Center of the Galaxy*, volume 136, page 89, January 1989.

[122] K. Ferrière, W. Gillard, and P. Jean. Spatial distribution of interstellar gas in the innermost 3 kpc of our galaxy. *A&A*, 467(2):611–627, May 2007.

[123] S. N. Longmore, J. Bally, L. Testi, C. R. Purcell, A. J. Walsh, E. Bressert, M. Pestalozzi, S. Molinari, J. Ott, L. Cortese, C. Battersby, N. Murray, E. Lee, J. M. D. Kruijssen, E. Schisano, and D. Elia. Variations in the Galactic star formation rate and density thresholds for star formation. *MNRAS*, 429(2):987–1000, February 2013.

[124] A. T. Barnes, S. N. Longmore, C. Battersby, J. Bally, J. M. D. Kruijssen, J. D. Henshaw, and D. L. Walker. Star formation rates and efficiencies in the Galactic Centre. *MNRAS*, 469(2):2263–2285, August 2017.

[125] H. Nguyen, M. R. Rugel, K. M. Menten, A. Brunthaler, S. A. Dzib, et al. A global view on star formation: The glostar galactic plane survey iv. radio continuum detections of young stellar objects in the galactic centre region, 2021.

[126] Richard M. Crutcher, Douglas A. Roberts, David M. Mehringer, and Thomas H. Troland. H i Zeeman Measurements of the Magnetic Field in Sagittarius B2. *ApJL*, 462:L79, May 1996.

[127] David T. Chuss, Jacqueline A. Davidson, Jessie L. Dotson, C. Darren Dowell, Roger H. Hildebrand, Giles Novak, and John E. Vaillancourt. Magnetic Fields in Cool Clouds within the Central 50 Parsecs of the Galaxy. *ApJ*, 599(2):1116–1128, December 2003.

[128] Katia Ferrière. The interstellar magnetic field near the Galactic center. In Nicholas H. Brummell, A. Sacha Brun, Mark S. Miesch, and Yannick Ponty, editors, *Astrophysical Dynamics: From Stars to Galaxies*, volume 271, pages 170–178, August 2011.

[129] Mattia C. Sormani and Ashley T. Barnes. Mass inflow rate into the Central Molecular Zone: observational determination and evidence of episodic accretion. *MNRAS*, 484(1):1213–1219, March 2019.

[130] C. Federrath, J. M. Rathborne, S. N. Longmore, J. M. D. Kruijssen, J. Bally, Y. Contreras, R. M. Crocker, G. Garay, J. M. Jackson, L. Testi, and A. J. Walsh. The link between solenoidal turbulence and slow star formation in G0.253+0.016. In Roland M. Crocker, Steven N. Longmore, and Geoffrey V. Bicknell, editors, *The Multi-Messenger Astrophysics of the Galactic Centre*, volume 322, pages 123–128, January 2017.

[131] J. M. Diederik Kruijssen, Steven N. Longmore, Bruce G. Elmegreen, Norman Murray, John Bally, Leonardo Testi, and Robert C. Kennicutt. What controls star formation in the central 500 pc of the Galaxy? *MNRAS*, 440(4):3370–3391, June 2014.

[132] Mark R. Krumholz and J. M. Diederik Kruijssen. A dynamical model for the formation of gas rings and episodic starbursts near galactic centres. *MNRAS*, 453(1):739–757, October 2015.

[133] J. M. Diederik Kruijssen and Steven N. Longmore. Comparing molecular gas across cosmic time-scales: the Milky Way as both a typical spiral galaxy and a high-redshift galaxy analogue. *MNRAS*, 435(3):2598–2603, November 2013.

[134] Adam Ginsburg, Elisabeth A. C. Mills, Cara D. Battersby, Steven N. Longmore, and J. M. Diederik Kruijssen. Galactic center star formation & feedback: key questions. *BAAS*, 51(3):220, May 2019.

[135] K. Ferrière. Interstellar magnetic fields in the Galactic center region. *A&A*, 505(3):1183–1198, October 2009.

[136] Mark R. Morris. *Manifestations of the Galactic Center Magnetic Field*, page 391. 2015.

[137] M. Morris and F. Yusef-Zadeh. Unusual threads of radio emission near the Galactic Center. *AJ*, 90:2511–2513, December 1985.

[138] Farhad Yusef-Zadeh and Mark Morris. The Linear Filaments of the Radio Arc near the Galactic Center. *ApJ*, 322:721, November 1987.

[139] Cornelia C. Lang, Mark Morris, and Luis Echevarria. A Radio Polarimetric Study of the Galactic Center Threads. *ApJ*, 526(2):727–743, December 1999.

[140] E. M. Purcell. *Interstellar grains as pinwheels.*, pages 155–167. 1975.

[141] G. Novak, J. L. Dotson, C. D. Dowell, R. H. Hildebrand, T. Renbarger, and D. A. Schleuning. Submillimeter Polarimetric Observations of the Galactic Center. *ApJ*, 529(1):241–250, January 2000.

[142] G. Novak, D. T. Chuss, T. Renbarger, G. S. Griffin, M. G. Newcomb, J. B. Peterson, R. F. Loewenstein, D. Pernic, and J. L. Dotson. First Results from the Submillimeter Polarimeter for Antarctic Remote Observations: Evidence of Large-Scale Toroidal Magnetic Fields in the Galactic Center. *ApJL*, 583(2):L83–L86, February 2003.

[143] Brenda C. Matthews, Christie A. McPhee, Laura M. Fissel, and Rachel L. Curran. The Legacy of SCUPOL: 850 μm Imaging Polarimetry from 1997 to 2005. *ApJS*, 182(1):143–204, May 2009.

[144] P. F. Roche, E. Lopez-Rodriguez, C. M. Telesco, R. Schödel, and C. Packham. The magnetic field in the central parsec of the Galaxy. *MNRAS*, 476(1):235–245, May 2018.

[145] A. Mangilli, J. Aumont, J. Ph. Bernard, A. Buzzelli, G. de Gasperis, et al. The geometry of the magnetic field in the central molecular zone measured by PILOT. *A&A*, 630:A74, October 2019.

[146] Planck Collaboration Int. XIX. *Planck* intermediate results. XIX. An overview of the polarized thermal emission from Galactic dust. *A&A*, 576:A104, 2015.

[147] J. W. Fowler, M. D. Niemack, S. R. Dicker, A. M. Aboobaker, P. A. R. Ade, et al. Optical design of the Atacama Cosmology Telescope and the Millimeter Bolometric Array Camera. *ApOpt*, 46(17):3444–3454, June 2007.

[148] C. L. Bennett, D. Larson, J. L. Weiland, N. Jarosik, G. Hinshaw, N. Odegard, K. M. Smith, R. S. Hill, B. Gold, M. Halpern, E. Komatsu, M. R. Nolta, L. Page, D. N. Spergel, E. Wollack, J. Dunkley, A. Kogut, M. Limon, S. S. Meyer, G. S. Tucker, and E. L. Wright. Nine-year Wilkinson Microwave Anisotropy Probe (WMAP) Observations: Final Maps and Results. *ApJS*, 208(2):20, October 2013.

[149] Planck Collaboration I. *Planck* 2013 results. I. Overview of products and scientific results. *A&A*, 571:A1, 2014.

[150] S. W. Henderson, R. Allison, J. Austermann, T. Baildon, N. Battaglia, et al. Advanced ACTPol Cryogenic Detector Arrays and Readout. *Journal of Low Temperature Physics*, 184(3-4):772–779, August 2016.

[151] S.-P. P. Ho, J. A. Austermann, J. A. Beall, S. K. Choi, N. F. Cothard, et al. Highly uniform 150 mm diameter multichroic polarimeter array deployed for CMB detection. In *Millimeter, Submillimeter, and Far-Infrared Detectors and Instrumentation for Astronomy VIII*, volume 9914 of *Proc. SPIE*, page 991418, July 2017.

[152] S. K. Choi, J. Austermann, J. A. Beall, K. T. Crowley, R. Datta, et al. Characterization of the Mid-Frequency Arrays for Advanced ACTPol. *Journal of Low Temperature Physics*, 193(3-4):267–275, November 2018.

[153] Sigurd K. Naess. How to avoid x'es around point sources in maximum likelihood cmb maps. *Journal of Cosmology and Astroparticle Physics*, 2019(12):060–060, Dec 2019.

[154] Jason R. Stevens, Neil Goeckner-Wald, Reijo Keskitalo, Nialh McCallum, Aamir Ali, et al. Designs for next generation CMB survey strategies from Chile. In Jonas Zmuidzinas and Jian-Rong Gao, editors, *Millimeter, Submillimeter, and Far-Infrared Detectors and Instrumentation for Astronomy IX*, volume 10708 of *Society of Photo-Optical Instrumentation Engineers (SPIE) Conference Series*, page 1070841, July 2018.

[155] Sigurd Naess, Simone Aiola, Jason E. Austermann, Nick Battaglia, James A. Beall, Daniel T. Becker, Richard J. Bond, Erminia Calabrese, Steve K. Choi, Nicholas F. Cothard, and et al. The atacama cosmology telescope: arcminute-resolution maps of 18 000 square degrees of the microwave sky from act 2008-2018 data combined with planck. *Journal of Cosmology and Astroparticle Physics*, 2020(12):046–046, Dec 2020.

[156] Planck Collaboration Int. LVII. *Planck* intermediate results. LVII. NPIPE: Joint *Planck LFI and HFI data processing*. *A&A*, 643:42, 2020.

[157] K. M. Górski, E. Hivon, A. J. Banday, B. D. Wandelt, F. K. Hansen, M. Reinecke, and M. Bartelmann. HEALPix: A Framework for High-Resolution Discretization and Fast Analysis of Data Distributed on the Sphere. *ApJ*, 622(2):759–771, April 2005.

[158] Planck Collaboration, N. Aghanim, Y. Akrami, M. Ashdown, J. Aumont, et al. Planck 2018 results. III. High Frequency Instrument data processing and frequency maps. *A&A*, 641:A3, September 2020.

[159] J. P. Hamaker and J. D. Bregman. Understanding radio polarimetry. III. Interpreting the IAU/IEEE definitions of the Stokes parameters. *A&AS*, 117:161–165, May 1996.

[160] Dylan M. Paré, Cornelia C. Lang, Mark R. Morris, Hailey Moore, and Sui Ann Mao. A VLA Polarimetric Study of the Galactic Center Radio Arc: Characterizing Polarization, Rotation Measure, and Magnetic Field Properties. *ApJ*, 884(2):170, October 2019.

[161] Kurt W. Weiler and Richard A. Sramek. Supernovae and supernova remnants. *ARA&A*, 26:295–341, January 1988.

[162] D. K. Milne. Nonthermal galactic radio sources. *Australian Journal of Physics*, 23:425, June 1970.

[163] D. J. Helfand and R. H. Becker. G0.9+0.1 and the Emerging Class of Composite Supernova Remnants. *ApJ*, 314:203, March 1987.

[164] F. Yusef-Zadeh, M. Morris, and D. Chance. Large, highly organized radio structures near the galactic centre. *Nature*, 310(5978):557–561, August 1984.

[165] A. Pedlar, K. R. Anantharamaiah, R. D. Ekers, W. M. Goss, J. H. van Gorkom, U. J. Schwarz, and Jun-Hui Zhao. Radio Studies of the Galactic Center. I. The Sagittarius A Complex. *ApJ*, 342:769, July 1989.

[166] Bryan M. Gaensler and Patrick O. Slane. The Evolution and Structure of Pulsar Wind Nebulae. *ARA&A*, 44(1):17–47, September 2006.

[167] Steven N. Longmore, Jill Rathborne, Nate Bastian, Joao Alves, Joana Ascenso, John Bally, Leonardo Testi, Andy Longmore, Cara Battersby, Eli Bressert, Cormac Purcell, Andrew Walsh, James Jackson, Jonathan Foster, Sergio Molinari, Stefan Meingast, A. Amorim, J. Lima, R. Marques, A. Moitinho, J. Pinhao, J. Rebordao, and F. D. Santos. G0.253 + 0.016: A Molecular Cloud Progenitor of an Arches-like Cluster. *ApJ*, 746(2):117, February 2012.

[168] R. Güsten and D. Downes. Formaldehyde in the Galactic Center region: interpretation. *A&A*, 87:6–19, July 1980.

[169] Planck Collaboration X. *Planck* 2015 results. X. Diffuse component separation: Foreground maps. *A&A*, 594:A10, 2016.

[170] H. S. Liszt and B. E. Turner. Microwave detection of interstellar NO. *ApJL*, 224:L73–L76, September 1978.

[171] A. Sandqvist. 2-mm H2CO emission in the SGR A molecular complex at the galactic center. *A&A*, 223:293–303, October 1989.

[172] C. Kramer, J. Staguhn, H. Ungerechts, and A. Sievers. The Sagittarius C region mapped in CS(2–>1) and (3–>2) with the IRAM 30m telescope. In Yoshiaki Sofue, editor, *The Central Regions of the Galaxy and Galaxies*, volume 184, page 173, January 1998.

[173] Cornelia C. Lang, W. M. Goss, and Mark Morris. The Molecular Component of the Galactic Center Arched Filaments H II Complex: OVRO Observations of the CS J=2-1 Line. *AJ*, 124(5):2677–2692, November 2002.

[174] Shunya Takekawa, Tomoharu Oka, Kunihiko Tanaka, Shinji Matsumura, Kodai Miura, and Daisuke Sakai. Millimeter-wave Spectral Line Surveys toward the Galactic Circumnuclear Disk and Sgr A*. *ApJS*, 214(1):2, September 2014.

[175] Marc W. Pound and Farhad Yusef-Zadeh. The CARMA 3 mm survey of the inner $0.7^\circ \times 0.4^\circ$ of the Central Molecular Zone. *MNRAS*, 473(3):2899–2929, January 2018.

[176] Xing Lu, Shanghuo Li, Adam Ginsburg, Steven N. Longmore, J. M. Diederik Kruijssen, Daniel L. Walker, Siyi Feng, Qizhou Zhang, Cara Battersby, Thushara Pillai, Elisabeth A. C. Mills, Jens Kauffmann, Yu Cheng, and Shu-ichiro Inutsuka. ALMA Observations of Massive Clouds in the Central Molecular Zone: Ubiquitous Protostellar Outflows. *ApJ*, 909(2):177, March 2021.

[177] F. Schuller, J. S. Urquhart, T. Csengeri, D. Colombo, A. Duarte-Cabral, et al. The SEDIGISM survey: First Data Release and overview of the Galactic structure. *MNRAS*, 500(3):3064–3082, January 2021.

[178] T. M. Dame, D. Hartmann, and P. Thaddeus. The Milky Way in Molecular Clouds: A New Complete CO Survey. *ApJ*, 547:792–813, February 2001.

[179] D. J. Eden, T. J. T. Moore, M. J. Currie, A. J. Rigby, E. Rosolowsky, et al. CHIMPS2: survey description and ^{12}CO emission in the Galactic Centre. *MNRAS*, 498(4):5936–5951, November 2020.

[180] S. Plaszczynski, L. Montier, F. Levrier, and M. Tristram. A novel estimator of the polarization amplitude from normally distributed Stokes parameters. *MNRAS*, 439(4):4048–4056, April 2014.

[181] J. L. Han. Observing Interstellar and Intergalactic Magnetic Fields. *ARA&A*, 55(1):111–157, August 2017.

[182] Brian Cabral and Leith Casey Leedom. Imaging vector fields using line integral convolution. In *Proceedings of the 20th annual conference on Computer graphics and interactive techniques*, pages 263–270, 1993.

[183] T. M. Ruud, U. Fuskeland, I. K. Wehus, M. Vidal, D. Araujo, C. Bischoff, I. Buder, Y. Chinone, K. Cleary, et al. The Q/U Imaging Experiment: Polarization Measurements of the Galactic Plane at 43 and 95 GHz. *ApJ*, 811(2):89, October 2015.

[184] Planck Collaboration, N. Aghanim, Y. Akrami, M. I. R. Alves, M. Ashdown, et al. Planck 2018 results. XII. Galactic astrophysics using polarized dust emission. *A&A*, 641:A12, September 2020.

[185] T. Pillai, J. Kauffmann, J. C. Tan, P. F. Goldsmith, S. J. Carey, and K. M. Menten. Magnetic Fields in High-mass Infrared Dark Clouds. *ApJ*, 799(1):74, January 2015.

[186] S. Molinari, J. Bally, A. Noriega-Crespo, M. Compiègne, J. P. Bernard, et al. A 100 pc Elliptical and Twisted Ring of Cold and Dense Molecular Clouds Revealed by Herschel Around the Galactic Center. *ApJL*, 735(2):L33, July 2011.

[187] T. N. LaRosa, Namir E. Kassim, T. Joseph W. Lazio, and S. D. Hyman. A Wide-Field 90 Centimeter VLA Image of the Galactic Center Region. *AJ*, 119(1):207–240, January 2000.

[188] R. D. Ekers, J. H. van Gorkom, U. J. Schwarz, and W. M. Goss. The radio structure of SGR A. *A&A*, 122:143–150, June 1983.

[189] F. Yusef-Zadeh and Mark Morris. Structural Details of the Sagittarius A Complex: Evidence for a Large-Scale Poloidal Magnetic Field in the Galactic Center Region. *ApJ*, 320:545, September 1987.

[190] K. R. Anantharamaiah, A. Pedlar, R. D. Ekers, and W. M. Goss. Radio studies of the galactic centre. II. The arc, threads and related features at 90 cm (330 MHz). *MNRAS*, 249:262, March 1991.

[191] A. M. Ghez, S. Salim, N. N. Weinberg, J. R. Lu, T. Do, J. K. Dunn, K. Matthews, M. R. Morris, S. Yelda, E. E. Becklin, T. Kremenek, M. Milosavljevic, and J. Naiman. Measuring Distance and Properties of the Milky Way's Central Supermassive Black Hole with Stellar Orbits. *ApJ*, 689(2):1044–1062, December 2008.

[192] D. C. Backer and R. A. Sramek. Proper Motion of the Compact, Nonthermal Radio Source in the Galactic Center, Sagittarius A*. *ApJ*, 524(2):805–815, October 1999.

[193] Susan R. Stolovy, T. L. Hayward, and Terry Herter. The First Mid-Infrared Detection of a Source Coincident with Sagittarius A *. *ApJL*, 470:L45, October 1996.

[194] Geoffrey C. Bower and Donald C. Backer. 7 Millimeter VLBA Observations of Sagittarius A*. *ApJL*, 496(2):L97–L100, April 1998.

[195] Fulvio Melia, Siming Liu, and Robert Coker. Polarized Millimeter and Submillimeter Emission from Sagittarius A* at the Galactic Center. *ApJL*, 545(2):L117–L120, December 2000.

[196] F. K. Baganoff, Y. Maeda, M. Morris, M. W. Bautz, W. N. Brandt, W. Cui, J. P. Doty, E. D. Feigelson, G. P. Garmire, S. H. Pravdo, G. R. Ricker, and L. K. Townsley. Chandra X-Ray Spectroscopic Imaging of Sagittarius A* and the Central Parsec of the Galaxy. *ApJ*, 591(2):891–915, July 2003.

[197] Eric Agol. Sagittarius A* Polarization: No Advection-dominated Accretion Flow, Low Accretion Rate, and Nonthermal Synchrotron Emission. *ApJL*, 538(2):L121–L124, August 2000.

[198] Fulvio Melia, Siming Liu, and Robert Coker. A Magnetic Dynamo Origin for the Submillimeter Excess in Sagittarius A*. *ApJ*, 553(1):146–157, May 2001.

[199] D. K. Aitken, J. Greaves, Antonio Chrysostomou, T. Jenness, W. Holland, J. H. Hough, D. Pierce-Price, and J. Richer. Detection of Polarized Millimeter and Submillimeter Emission from Sagittarius A*. *ApJL*, 534(2):L173–L176, May 2000.

[200] Jean-Pierre Macquart, Geoffrey C. Bower, Melvyn C. H. Wright, Donald C. Backer, and Heino Falcke. The Rotation Measure and 3.5 Millimeter Polarization of Sagittarius A*. *ApJL*, 646(2):L111–L114, August 2006.

[201] Daniel P. Marrone, James M. Moran, Jun-Hui Zhao, and Ramprasad Rao. The Submillimeter Polarization of Sgr A*. In *Journal of Physics Conference Series*, volume 54 of *Journal of Physics Conference Series*, pages 354–362, December 2006.

[202] E. Serabyn and Mark Morris. The Source of the Relativistic Particles in the Galactic Center Arc. *ApJL*, 424:L91, April 1994.

[203] Wolfgang Reich, Yoshiaki Sofue, and Hiroshi Matsuo. 150 GHz NOBA Observations of the Galactic Center Arc. *PASJ*, 52:355, April 2000.

[204] Johannes Staguhn, Richard G. Arendt, Eli Dwek, Mark R. Morris, Farhad Yusef-Zadeh, Dominic J. Benford, Attila Kovács, and Junellie Gonzalez-Quiles. 2 mm GISMO Observations of the Galactic Center. II. A Nonthermal Filament in the Radio Arc and Compact Sources. *ApJ*, 885(1):72, November 2019.

[205] T. Culverhouse, P. Ade, J. Bock, M. Bowden, M. L. Brown, et al. The QUaD Galactic Plane Survey. II. A Compact Source Catalog. *ApJS*, 195(1):8, July 2011.

[206] Sean J. Carey, F. O. Clark, M. P. Egan, S. D. Price, R. F. Shipman, and T. A. Kuchar. The Physical Properties of the Midcourse Space Experiment Galactic Infrared-dark Clouds. *ApJ*, 508(2):721–728, December 1998.

[207] D. C. Lis, K. M. Menten, E. Serabyn, and R. Zylka. Star Formation in the Galactic Center Dust Ridge. *ApJL*, 423:L39, March 1994.

[208] Jens Kauffmann, Thushara Pillai, and Qizhou Zhang. The Galactic Center Cloud G0.253+0.016: A Massive Dense Cloud with low Star Formation Potential. *ApJL*, 765(2):L35, March 2013.

[209] E. A. C. Mills, N. Butterfield, D. A. Ludovici, C. C. Lang, J. Ott, M. R. Morris, and S. Schmitz. Abundant CH_3OH Masers but no New Evidence for Star Formation in GCM0.253+0.016. *ApJ*, 805(1):72, May 2015.

[210] Daniel L. Walker, Steven N. Longmore, John Bally, Adam Ginsburg, J. M. Diederik Kruijssen, Qizhou Zhang, Jonathan D. Henshaw, Xing Lu, João Alves, Ashley T. Barnes, Cara Battersby, Henrik Beuther, Yanett A. Contreras, Laura Gómez, Luis C. Ho, James M. Jackson, Jens Kauffmann, Elisabeth A. C. Mills, and Thushara Pillai. Star formation in 'the Brick': ALMA reveals an active protocluster in the Galactic centre cloud G0.253+0.016. *MNRAS*, 503(1):77–95, May 2021.

[211] C. Federrath, J. M. Rathborne, S. N. Longmore, J. M. D. Kruijssen, J. Bally, Y. Contreras, R. M. Crocker, G. Garay, J. M. Jackson, L. Testi, and A. J. Walsh. The Link between Turbulence, Magnetic Fields, Filaments, and Star Formation in the Central Molecular Zone Cloud G0.253+0.016. *ApJ*, 832(2):143, December 2016.

[212] J. M. D. Kruijssen, J. E. Dale, S. N. Longmore, D. L. Walker, J. D. Henshaw, S. M. R. Jeffreson, M. A. Petkova, A. Ginsburg, A. T. Barnes, C. D. Battersby, K. Immer, J. M. Jackson, E. R. Keto, N. Krieger, E. A. C. Mills, Á. Sánchez-Monge, A. Schmiedeke, S. T. Suri, and Q. Zhang. The dynamical evolution of molecular clouds near the Galactic Centre - II. Spatial structure and kinematics of simulated clouds. *MNRAS*, 484(4):5734–5754, April 2019.

[213] J. E. Dale, J. M. Diederik Kruijssen, and S. N. Longmore. The dynamical evolution of molecular clouds near the Galactic Centre - III. Tidally induced star formation in protocluster clouds. *MNRAS*, 486(3):3307–3326, July 2019.

[214] J. D. Henshaw, A. Ginsburg, T. J. Haworth, S. N. Longmore, J. M. D. Kruijssen, E. A. C. Mills, V. Sokolov, D. L. Walker, A. T. Barnes, Y. Contreras, J. Bally, C. Battersby, H. Beuther, N. Butterfield, J. E. Dale, T. Henning, J. M. Jackson, J. Kauffmann, T. Pillai, S. Ragan, M. Riener, and Q. Zhang. 'The Brick' is not a brick: a comprehensive study of the structure and dynamics of the central molecular zone cloud G0.253+0.016. *MNRAS*, 485(2):2457–2485, May 2019.

[215] Jessie L. Dotson, John E. Vaillancourt, Larry Kirby, C. Darren Dowell, Roger H. Hildebrand, and Jacqueline A. Davidson. 350 μm Polarimetry from the Caltech Submillimeter Observatory. *ApJS*, 186(2):406–426, February 2010.

[216] H. Parsons, J. T. Dempsey, H. S. Thomas, D. Berry, M. J. Currie, P. Friberg, J. G. A. Wouterloot, A. Chrysostomou, S. Graves, R. P. J. Tilanus, G. S. Bell, and M. G. Rawlings. The Dusty Galactic Center as Seen by SCUBA-2. *ApJS*, 234(2):22, February 2018.

[217] P. Predehl and S. R. Kulkarni. G359.23-0.92, the Mouse, a plusar powered bow shock? *A&A*, 294:L29–L31, February 1995.

[218] F. Camilo, R. N. Manchester, B. M. Gaensler, and D. R. Lorimer. Heartbeat of the Mouse: A Young Radio Pulsar Associated with the Axisymmetric Nebula G359.23-0.82. *ApJL*, 579(1):L25–L28, November 2002.

[219] Farhad Yusef-Zadeh and John Bally. A non-thermal axially symmetric radio wake towards the galactic centre. *Nature*, 330(6147):455–458, December 1987.

[220] F. Yusef-Zadeh and B. M. Gaensler. A radio study of the mouse, G359.23 - 0.82. *Advances in Space Research*, 35(6):1129–1136, January 2005.

[221] Keven Uchida, Mark Morris, and Farhad Yusef-Zadeh. An H1 Absorption Line Study of the Nonthermal Shell Near the Galactic Center, G359.1-0.5 and Several Nearby Unusual radio Features. *AJ*, 104:1533, October 1992.

[222] B. M. Gaensler, E. van der Swaluw, F. Camilo, V. M. Kaspi, F. K. Baganoff, F. Yusef-Zadeh, and R. N. Manchester. The Mouse that Soared: High-Resolution X-Ray Imaging of the Pulsar-powered Bow Shock G359.23-0.82. *ApJ*, 616(1):383–402, November 2004.

[223] Noel Klingler, Oleg Kargaltsev, George G. Pavlov, C. Y. Ng, Paz Beniamini, and Igor Volkov. The Mouse Pulsar Wind Nebula. *ApJ*, 861(1):5, July 2018.

[224] C. A. Hales, B. M. Gaensler, S. Chatterjee, E. van der Swaluw, and F. Camilo. A Proper Motion for the Pulsar Wind Nebula G359.23-0.82, the "Mouse," Associated with the Energetic Radio Pulsar J1747-2958. *ApJ*, 706(2):1316–1322, December 2009.

[225] B. M. Gaensler, J. K. J. Fogel, P. O. Slane, J. M. Miller, R. Wijnands, S. S. Eikenberry, and W. H. G. Lewin. Untwisting the Tornado: X-Ray Imaging and Spectroscopy of G357.7-0.1. *ApJL*, 594(1):L35–L38, September 2003.

[226] H. Chawner, A. D. P. Howard, H. L. Gomez, M. Matsuura, F. Priestley, M. J. Barlow, I. De Looze, A. Papageorgiou, K. Marsh, M. W. L. Smith, A. Noriega-Crespo, J. Rho, and L. Dunne. A Galactic dust devil: far-infrared observations of the Tornado supernova remnant candidate. *MNRAS*, 499(4):5665–5678, December 2020.

[227] P. A. Shaver, C. J. Salter, A. R. Patnaik, J. H. van Gorkom, and G. C. Hunt. Two remarkable bright supernova remnants. *Nature*, 313(5998):113–115, January 1985.

[228] C. J. Law, F. Yusef-Zadeh, W. D. Cotton, and R. J. Maddalena. Green Bank Telescope Multiwavelength Survey of the Galactic Center Region. *ApJS*, 177(1):255–274, July 2008.

[229] John Bally, Antony A. Stark, Robert W. Wilson, and Christian Henkel. Galactic Center Molecular Clouds. II. Distribution and Kinematics. *ApJ*, 324:223, January 1988.

[230] S. Huettemeister, G. Dahmen, R. Mauersberger, C. Henkel, T. L. Wilson, and J. Martin-Pintado. Molecular gas in the Galactic center region. III. Probing shocks in molecular cores. *A&A*, 334:646–658, June 1998.

[231] Tomoharu Oka, Tetsuo Hasegawa, Fumio Sato, Masato Tsuboi, and Atsushi Miyazaki. A Hyperenergetic CO Shell in the Galactic Center Molecular Cloud Complex. *PASJ*, 53(5):787–791, October 2001.

[232] N. J. Rodriguez-Fernandez, F. Combes, J. Martin-Pintado, T. L. Wilson, and A. Apponi. Coupling the dynamics and the molecular chemistry in the Galactic center. *A&A*, 455(3):963–969, September 2006.

[233] Kunihiko Tanaka, Kazuhisa Kamegai, Makoto Nagai, and Tomoharu Oka. High-Resolution Mappings of the l=1°.3 Complex in Molecular Lines: Discovery of a Proto-Superbubble. *PASJ*, 59:323–333, April 2007.

[234] Shiho Tsujimoto, Tomoharu Oka, Shunya Takekawa, Yuhei Iwata, Asaka Uruno, Hiroki Yokozuka, Ryosuke Nakagawara, Yuto Watanabe, Akira Kawakami, Sonomi Nishiyama, Miyuki Kaneko, Shoko Kanno, and Takuma Ogawa. New Look at the Molecular Superbubble Candidate in the Galactic Center. *ApJ*, 910(1):61, March 2021.

[235] R. Fux. 3D self-consistent N-body barred models of the Milky Way. II. Gas dynamics. *A&A*, 345:787–812, May 1999.

[236] H. S. Liszt. Multiplicity of nuclear dust lanes and dust lane shocks in the Milky Way bar. *A&A*, 486(2):467–470, August 2008.

[237] Yaqiong Li, Jason E. Austermann, James A. Beall, Sarah Marie Bruno, Steve K. Choi, et al. Performance of the advanced ACTPol low frequency array. In *Proc. SPIE*, volume 10708 of *Society of Photo-Optical Instrumentation Engineers (SPIE) Conference Series*, page 107080A, July 2018.

[238] S. M. Simon, J. A. Beall, N. F. Cothard, S. M. Duff, P. A. Gallardo, S. P. Ho, J. Hubmayr, B. J. Koopman, J. J. McMahon, F. Nati, M. D. Niemack, S. T. Staggs, E. M. Vavagiakis, and E. J. Wollack. The Advanced ACTPol 27/39 GHz Array. *Journal of Low Temperature Physics*, 193(5-6):1041–1047, December 2018.

[239] Ningfeng Zhu, Tanay Bhandarkar, Gabriele Coppi, Anna M. Kofman, John L. Orlowski-Scherer, et al. The Simons Observatory Large Aperture Telescope Receiver. *arXiv e-prints*, page arXiv:2103.02747, March 2021.

[240] S. K. Choi, J. Austermann, K. Basu, N. Battaglia, F. Bertoldi, et al. Sensitivity of the Prime-Cam Instrument on the CCAT-Prime Telescope. *Journal of Low Temperature Physics*, 199(3-4):1089–1097, March 2020.

[241] Ian Lowe, Gabriele Coppi, Peter A. R. Ade, Peter C. Ashton, Jason E. Austermann, et al. The Balloon-borne Large Aperture Submillimeter Telescope Observatory. In *Society of Photo-Optical Instrumentation Engineers (SPIE) Conference Series*, volume 11445 of *Society of Photo-Optical Instrumentation Engineers (SPIE) Conference Series*, page 114457A, December 2020.

[242] Rolando Dünner. *From Data to Maps with the Atacama Cosmology Telescope*. PhD thesis, 2009.

[243] Planck Collaboration I. *Planck* 2018 results. I. Overview, and the cosmological legacy of *Planck*. *A&A, in press*, 2019.

[244] R. A. Sunyaev and Ya. B. Zeldovich. The velocity of clusters of galaxies relative to the microwave background - The possibility of its measurement. *MNRAS*, 190:413–420, February 1980.

[245] Silvia Galli, Karim Benabed, François Bouchet, Jean-François Cardoso, Franz Elsner, Eric Hivon, Anna Mangilli, Simon Prunet, and Benjamin Wandelt. CMB polarization can constrain cosmology better than CMB temperature. *PhRvD*, 90(6):063504, September 2014.

[246] Rolando Dünner, Matthew Hasselfield, Tobias A. Marriage, Jon Sievers, Viviana Acquaviva, et al. The Atacama Cosmology Telescope: Data Characterization and Mapmaking. *ApJ*, 762(1):10, January 2013.

[247] Yilun Guan, Susan E. Clark, Brandon S. Hensley, Patricio A. Gallardo, Sigurd Naess, Cody J. Duell, et al. The Atacama Cosmology Telescope: Microwave Intensity and Polarization Maps of the Galactic Center. *arXiv e-prints*, page arXiv:2105.05267, May 2021.

[248] Wei-Yin Loh. Fifty years of classification and regression trees. *International Statistical Review*, 82(3):329–348, 2014.

[249] Leo Breiman. Random forests. *Mach. Learn.*, 45(1):5–32, October 2001.

[250] Evelyn Fix and J. L. Hodges. Discriminatory analysis. nonparametric discrimination: Consistency properties. *International Statistical Review / Revue Internationale de Statistique*, 57(3):238–247, 1989.

[251] Naomi S Altman. An introduction to kernel and nearest-neighbor nonparametric regression. *The American Statistician*, 46(3):175–185, 1992.

[252] F. Pedregosa, G. Varoquaux, A. Gramfort, V. Michel, B. Thirion, O. Grisel, M. Blondel, P. Prettenhofer, R. Weiss, V. Dubourg, J. Vanderplas, A. Passos, D. Cournapeau, M. Brucher, M. Perrot, and E. Duchesnay. Scikit-learn: Machine learning in Python. *Journal of Machine Learning Research*, 12:2825–2830, 2011.

[253] Tianqi Chen and Carlos Guestrin. XGBoost: A scalable tree boosting system. In *Proceedings of the 22nd ACM SIGKDD International Conference on Knowledge Discovery and Data Mining*, KDD '16, pages 785–794, New York, NY, USA, 2016. ACM.